Title

Ultrasonic Guided Waves Test Method for Blunt Impact Damage Assessment on Composite Aircraft Structures

Permalink

https://escholarship.org/uc/item/9pp6p9gm

Author

Kim, Hyung Suk

Publication Date

2020

UNIVERSITY OF CALIFORNIA SAN DIEGO

Ultrasonic Guided Waves Test Method for Blunt Impact Damage Assessment on Composite Aircraft Structures

A dissertation submitted in partial satisfaction of the

requirements for the degree Doctor of Philosophy

in

Structural Engineering

by

Hyung Suk Kim

Committee in charge:

Professor Hyonny Kim, Chair
Professor Veronica Eliasson
Professor Francesco Lanza Di Scalea
Professor Kenneth J. Loh
Professor Vitali F. Nesterenko

2020

The Dissertation of Hyung Suk Kim is approved, and
it is acceptable in quality and form for publication
on microfilm and electronically:

Chair

University of California San Diego

2020

DEDICATION

I dedicate my doctoral dissertation to my wife and my best friend, Linda Seol. Also to my wonderful daughters, Teresa and Eleanor Kim, and to my parents, Nak Woong Kim and Young Ae Kwon for their endless love and support.

TABLE OF CONTENTS

LIST OF ABBREVIATIONS

BID	Blunt Impact Damage
NDE	Non-Destructive Evaluation
UGW	Ultrasonic Guided Wave
HEWABI	High Energy, Wide Area, Blunt Impact
GSE	Ground Service Equipment
UT	Ultrasonic Testing
FAA	Federal Aviation Administration
LEFM	Linear Elastic Fracture Mechanics
SNR	Signal-to-Noise Ratio
VARTM	Vacuum Assisted Resin Transfer Molding
RMS	Root Mean Square
FEM	Finite Element Model
CWT	Continuous Wavelet Transform
FSP	Flat Stringer Panel
CT	Computed Tomography
CAI	Compression-After-Impact
COI	Center-of-Impact
TOF	Time-of-Flight
BAT	Broadband Air-coupled Transducer
S0	First symmetrical wave mode
A0	First anti-symmetrical wave mode
OHT	Open-Hole Tension

DIC	Digital Image Correlation

LIST OF FIGURES

LIST OF TABLES

ACKNOWLEDGEMENTS

I would like to express my deep and sincere gratitude to my advisor, Professor Hyonny Kim, for all his invaluable teachings, guidance, and encouragement throughout the years of my PhD student life. I am truly honored to have worked under him, not only because he was the best advisor, but also because he showed me the life path I wish to pursue. I am forever indebted to him for I know this research would not have been possible without his support.

I am also extremely grateful for Professor Francesco Lanza di Scalea's insightful feedback and explanations through the many struggles I had with the research project. A special thank you also to my Committees, Professor Veronica Eliasson, Professor Kenneth Loh, and Professor Vitali Nesterenko for their valuable feedback on my research .

I would also like to acknowledge the Federal Aviation Administration for supporting the fund for the project, especially Dr. Larry Ilcewicz for all his excellent advice and great experiences he has shared throughout the project.

I cannot express enough thanks to Margherita Capriotti for being the best research collaborator. She has truly accomplished some amazing work through our years of collaborative research and has always remained the kindest person even through the hardships we experienced while trying to make progress. I acknowledge Andrew Ellison for his visionary research ideas and his great work ethics. And all the members in the group, Konstantinos Anagnostopoulos, Moonhee Nam, Mimi Ngo, Chaiane Wiggers De Souza, and Javier Buenrostro for always being there to help. I am thankful to have worked with everyone.

I also would like to thank Dr. Gabriela DeFrancisci and Dr. Zhi Ming Chen —my research was possible because of your excellent work on the HEWABI research and the valuable specimens and information you left behind.

Chapter 2 contains publication material as it may appear in "Non-Destructive Inspection of Impact Damage in Composite Aircraft Panels by Ultrasonic Guided Waves and Statistical Processing." Capriotti, Margherita; Kim, Hyungsuk E.; Lanza di Scalea, Francesco; Kim, Hyonny. Materials, 2017. The dissertation author was the primary investigator and author of this paper.

Chapter 2 also contains material currently being prepared for submission for publication. "Ultrasonic Guided Wave Testing for Damage Detection on Bolted Joint Internal Components of Composite Structures." Kim, Hyungsuk E.; Kim, Hyonny; Capriotti, Margherita. The dissertation author was the primary investigator and author of this material.

Chapter 2 also contains material currently being prepared for submission for publication. "Non-Destructive Evaluation Methods for Detecting Major Damage in Internal Composite Structural Components." Capriotti, Margherita; Kim, Hyungsuk E.; Lanza di Scalea, Francesco; Kim, Hyonny. The dissertation author was the primary investigator and author of this material.

Chapter 3 contains material currently being prepared for submission for publication. Capriotti, Margherita; Ellison, Andrew; Kim, Hyungsuk E.; Lanza di Scalea, Francesco; Kim, Hyonny. The dissertation author was the primary investigator and author of this material.

VITA

EDUCATION

2011	Bachelor of Science in Aerospace Engineering, University of California San Diego
2016	Master of Science in Structural Engineering, , University of California San Diego
2019	Doctor of Philosophy in Structural Engineering, , University of California San Diego

PUBLICATIONS

Capriotti, Margherita, Hyungsuk E. Kim, Francesco Lanza di Scalea, and Hyonny Kim. "Non-Destructive inspection of impact damage in composite aircraft panels by ultrasonic guided waves and statistical processing." *Materials*, vol. 10, no. 6, pp. 616, 2017.

Lanza di Scalea, Francesco, Hyonny Kim, Hyungsuk E. Kim, Margherita Capriotti, Ranting Cui. "Non-Destructive Evaluation Methods for Detecting Major Damage in Internal Composite Structures." *JAMS Technical Review Presentation*, 2018.

Capriotti, Margherita, Hyungsuk E. Kim, Francesco Lanza di Scalea, and Hyonny Kim. "Detection of major impact damage to composite aerospace structures by ultrasonic guided waves and statistical signal processing." *Procedia Engineering*, vol. 199, pp. 1550-1555, 2017.

Margherita Capriotti, Hyungsuk E. Kim, Francesco Lanza di Scalea, Hyonny Kim. "Non-Destructive Evaluation Methods for Detecting Major Damage in Internal Composite Structural Components." Technical Report to Federal Aviation Administration, DOT/FAA/TC-18/50, 2019.

EXPERIENCES

2014-2020	Graduate Student Researcher, Structural Engineering Department at University of California San Diego
2016-2018	Teaching Assistant for “Aerospace Structures Repair”, Structural Engineering Department at University of California San Diego

ABSTRACT OF THE DISSERTATION

Ultrasonic Guided Waves Test Method for Blunt Impact Damage Assessment on Composite Aircraft Structures

by

Hyung Suk Kim
Doctor of Philosophy in Structural Engineering
University of California San Diego, 2020
Professor Hyonny Kim, Chair

Blunt impact damage (BID) is known to potentially cause significant strength reduction on composite structures even when the damage is barely noticeable. Therefore, non-destructive evaluation (NDE) to assess blunt-impacted composite aircraft structures is a crucial procedure to determine existence and severity of the damage to examine airworthiness. Ultrasonic guided waves (UGWs) test method has been studied herein as an NDE technique to evaluate large composite structures, because the typically thin-walled aircraft structures effectively act as has guided waves propagation paths.

UGW scanning methods were performed only from the external skin-side using pitch-catch method: an actuator and a receiver located at a distance apart to scan the structure within. The actuator and the receiver transducers were placed on the adjacent skin-to-shear tie bolted joint regions for scanning of internal shear tie and C-frame components, and placed at opposite sides of the hat stringer on the skin bay for investigation of co-cured stringer components. UGWs transmission through bolted joint structure was examined to determine the test frequency that allowed wave transmission through bolted joints at low attenuation. And UGW tests from the skin-to-shear tie joint regions identified significant wave energy drop at the test frequency from the comparison of the pristine and the damaged (HEWABI) shear ties. Furthermore, damage characteristics were analyzed from the UGW measurements of the stringer scan followed by successful blunt impacted stringer delamination damage detection. Features extracted from the UGW test results showed exceptional match to the damage location, severity, and modes determined from the conventional NDE methods. Finally, UGW measurements-based residual strength estimation was studied from simple notched coupon tests and is an on-going study for more complex structures with realistic damage modes.

1. Introduction

1.1. Motivation

The first aircraft structure was built from wood, a natural composite, and since then aircraft structure material has evolved towards metal bodies to now an engineered composite material, namely fiber-reinforced polymer composite that provides exceptional strength for the weight. The aerospace industry has recently employed a major portion of its commercial aircraft structure built from composite laminate material. Boeing 787 is composed of 80% volume of composite material, that is approximately 50% of the weight of the aircraft, which enables a 20% fuel efficiency achievement.

Even with the great benefit achieved on aircraft structures from implementing a large percentile of composite laminate, damage induced from blunt impact on composite structures pose a great threat that generates substantial, but barely visible damage to the composite structure. Blunt impact damage (BID) occurs as a result of large-area contact, or impact, to a structure (e.g., from Ground Service Equipment (GSE) as shown in Figure 1.1.1), possibly causing significant internal damage with no visible denting, and thus can significantly reduce the strength of the structure even when it seems insignificant from an external, visual perspective. Blunt impacts on composite structures were studied to generate complex damage modes (matrix crack, fiber breakage, and delamination) [1-4]. Since BID is not always obvious on composite structures, extensive investigation using non-destructive evaluation (NDE) is needed to determine if damage was induced and repair is needed [5]. Especially, high energy wide area blunt impact (HEWABI) from GSE accident scenario testing on sub-component level composite structures generated very severe damage on the internal components that is hidden beneath the composite skin shell (see Figure 1.1.2.a and b) [4].

Figure 1.1.1. GSE on an aircraft at the ramp

A key question is whether blunt impacted composite structures incur damage in the internal structure, and whether the structures need an invasive inspection (disassembly of the interior panels to access internal side of the structures). Invasive inspection of composite aircraft fuselage is a costly process from the maintenance perspective, and the aircraft operation time loss from being out-of-service for maintenance is significant. Today, conventional NDE methods, such as ultrasonic testing (UT), eddy current testing (ET), radiography testing (RT), magnetic particle testing (MT), infrared thermography (IR), and more, are used in the field to evaluate the damage on aircraft structures.

Current NDE techniques are suitable to detect and determine damage on composite structures, but they are limited to only the external skin damage detection and cannot inspect for damages on the internal structure unless direct access to internal components is available (usually covered by aircraft interior materials). An NDE test method that can detect the existence of damage in the internal structure only from the external skin-side needs to be developed so to prevent unnecessary disassembly of aircraft structures for internal structure inspection. Research in this dissertation focuses on and evaluates Ultrasonic Guided Wave (UGW) test methods as a means to investigate internal structure of composite aircraft from the external side test only.

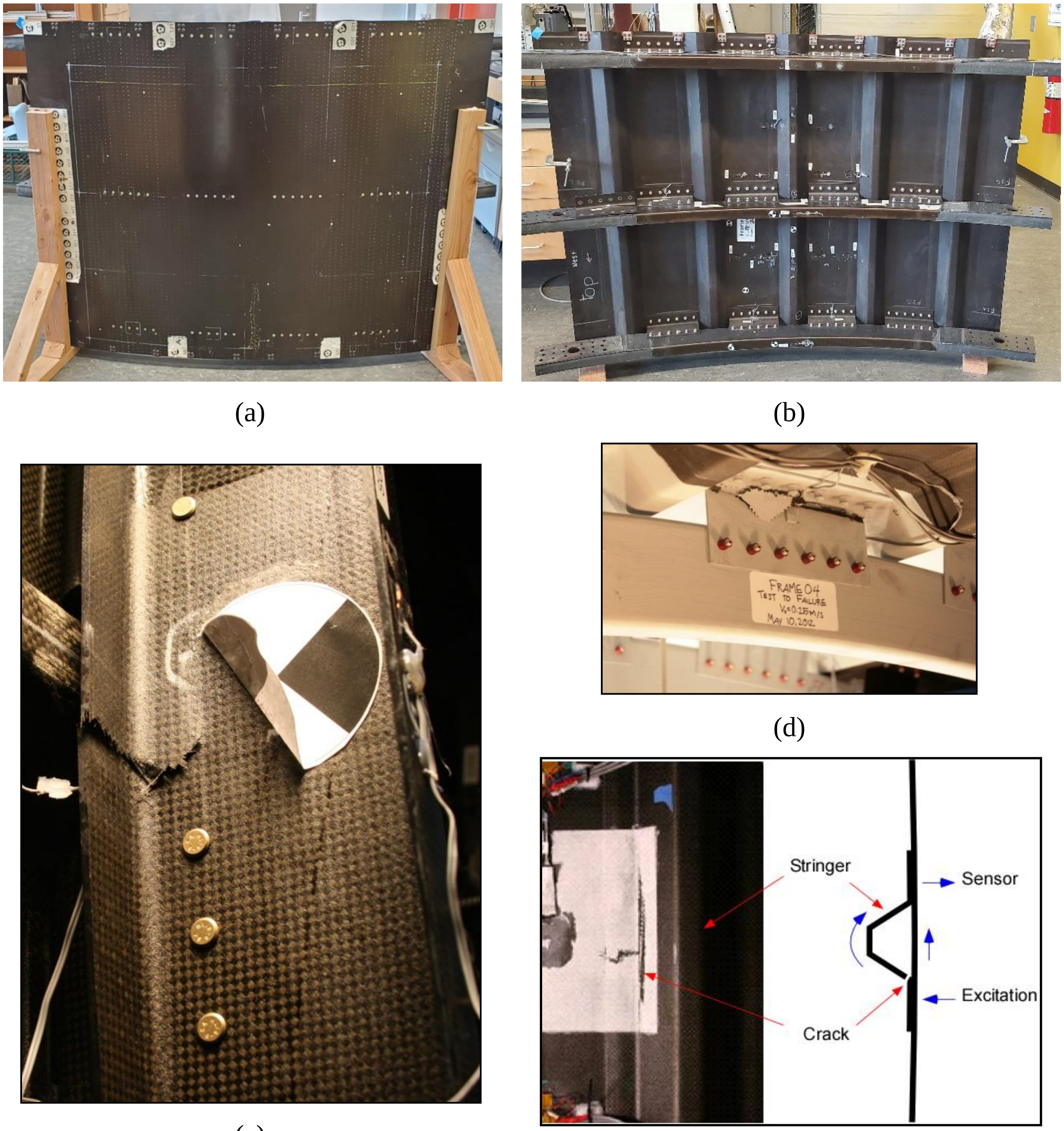
(a) (b)

(c) (d) (e)

Figure 1.1.2. Frame02 Panel from (a) external view, (b) interval view, and a few of the damage modes from HEWABI panels: (c) cracked C-frame, (d) shear tie, and (e) stringer heel

1.2. Objectives and Test Approach

The research objectives were as follows:

- The first objective of the research was to non-destructively detect damage on blunt impacted composite structures (i.e., panel shown in Figure 1.1.2) from a UGW test performed only from exterior skin-side access. UGW test on composite structure was primarily focused on detecting damage on the internal components, such as cracked shear ties and C-frames, and cracked and delaminated stringers (see Figure 1.1.2.c, d and e), but also for near the skin surface damage detection.
- The second objective was to assess UGW test results for detailed understanding of the damage status, such as damage modes, severity and location .
- Then, as the third objective, residual strength of the structure was studied from UGW-based damage status evaluation.
- The last objective of the research was to develop a practical UGW test system (lightweight, portable and ramp-friendly), achieved along with the primary objectives of the research, the UGW-based damage analysis.

The first objective was achieved from the UGW-based structural scanning scheme as shown in Figure 1.2.1. To elaborate the research hypothesis, excitation generated on the external skin propagates through thin composite structures as guided waves (ultrasonic frequency range in this study) to all the possible wave paths. Specifically, excitation generated on the skin-to-shear tie bolted joint, location 6 in Figure 1.2.1, was received from the adjacent skin-to-shear tie joint, location 5 or 7 in Figure 1.2.1, and the UGW that propagated through the bolted joint internal frame path was distinguished from the UGW transmitted through the skin and stringer paths (see

Figure 1.2.2). Differential comparison of the UGWs through structural mirroring wave paths was approached (e.g., compare received signals from location 5 and 7 to identify structural abnormality as proposed in the hypothesis). However, UGWs through mirror paths investigated from the systematic structural assembly as shown in Figure 1.2.3 were determined to deliver asymmetric waves through the mirroring structure on C-frame. Thus, the test approach modification was made to interrogate structural damage state from UGWs through each unique path. Nonetheless, UGW through the frame path was clearly identified from the received signal on the skin and was distinguished from the skin and stringer path UGW in discrete frequency band from a broadband frequency excitation test methodology. Broadband frequency excitation test method showed viability of internal structure damage detection of complex composite structures. Received signals were post-processed to extract out features sensitive to certain damage modes to determine damage modes, locations, and severity. Features of the UGW at the impact location were identified to be related to the damage severity, which is an on-going study to be correlated to the residual strength. Finally, the UGW test system was reduced in weight and volume significantly, less than 2.5 kg in weight, from invention of a mechanical broadband frequency excitation source, the mini-impactor.

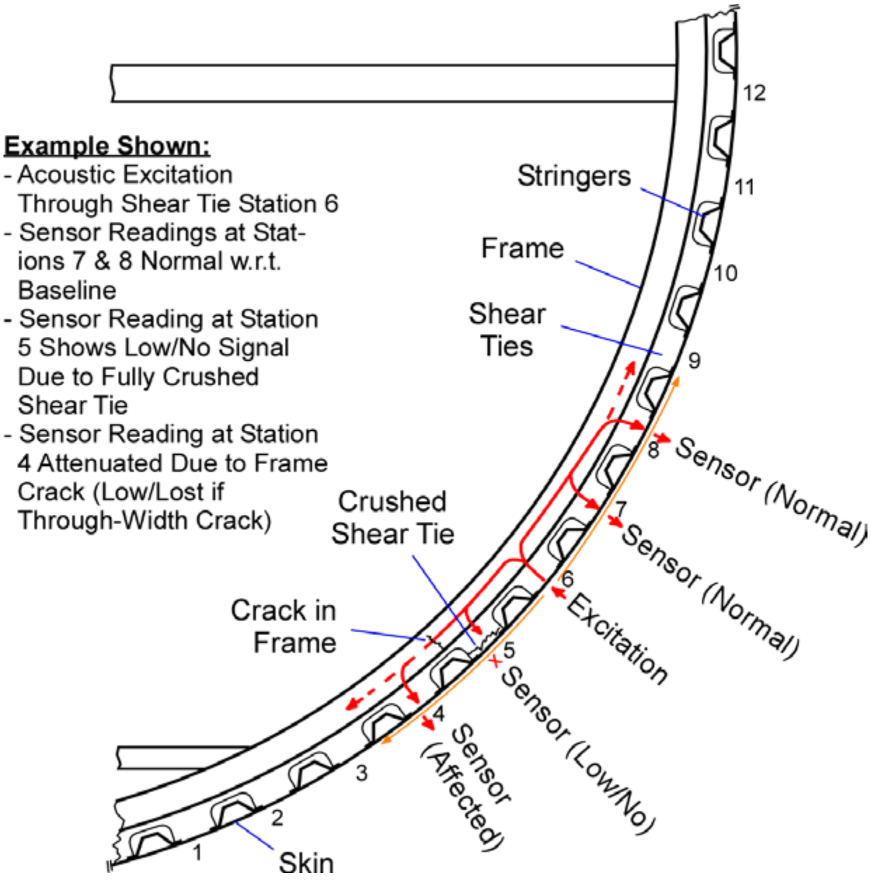

Figure 1.2.1 UGW experiment schematic

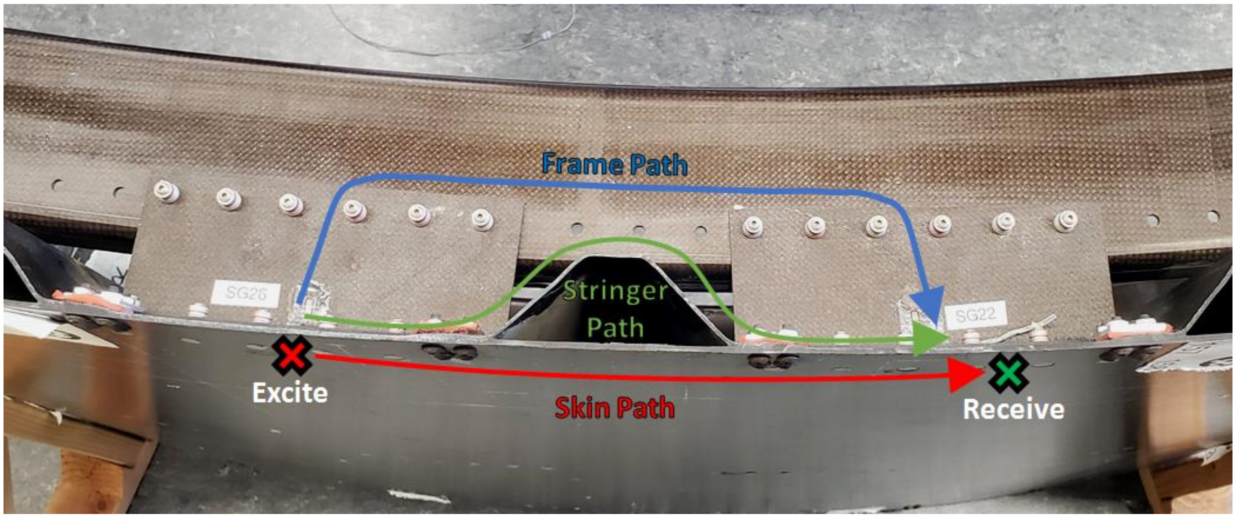

Figure 1.2.2 Wave transmission paths from an excitation and reception from exterior skin+shear tie joints

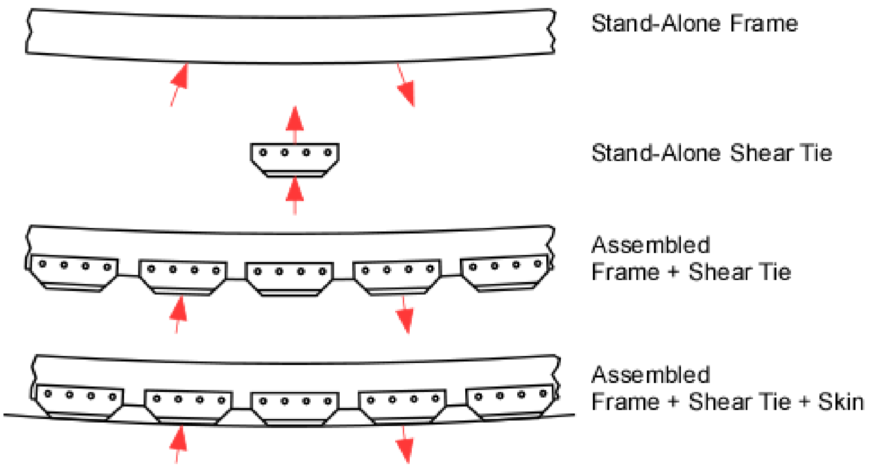

Figure 1.2.3 UGW experiment schematic on the systematic assembly of the structure

1.3. Novel Contributions

The foremost novel contribution to be noted from this research work is demonstrating capability of NDE damage detection of internal structural components from UGW tests performed only from the external skin-side. Damage located on shear ties, C-frames, and hat stringers (particularly at heel and/or cap of the hat stringer) cannot be identified from the current state-of-art NDE techniques. This study focused on UGW NDE method which would be used on structures only when an investigation is needed, unlike the Structural Health Monitoring (SHM) method that continuously monitors the structure using embedded sensors.

The second novel contribution is the invention of a mini-impactor, an excitation source, that generates broadband frequency excitation at high intensity. The mini-impactor, which is still in the stage of development, can generate broadband frequency excitation up to 400 kHz on composite laminate (current "off the shelf" systems generate up to 30 kHz) that is repeatable and very lightweight. Given the consistently repeatable high intensity excitation, heavy and bulky amplification equipment were eliminated from the UGW test system, making the whole system portable.

The third novel contribution is the correlation study of UGW results to the residual strength of composite laminate. Damage tolerance estimation requires accurate evaluation of the damage type, size and location from NDE measurements to increase the accuracy of the damage assessment. Open-hole notch sizes estimated from UGW test results on composite laminate were correlated to the residual tensile strengths of the corresponding notched composite laminate.

1.4. Background

1.4.1. Blunt Impact Damage on Composite Laminate

Air vehicles are prone to blunt impact accidents from nature (e.g., ice hail impacts and bird strikes) and from human mistakes (e.g., GSE accidents and tool drops). Blunt impact accidents on composite structures is not always obvious, but can result in major internal damage which significantly diminishes the strength of the structure. Impact on composite laminates generate complex damage modes which varies by many factors from the impact source: impact area, shape, material, velocity, etc.

Low velocity blunt impact study with varying radius of hemispherical impactor tip from pendulum impactor showed that higher energy was required to generate damage on composite laminates as the radius of the impactor increased due to the larger contact area from increasing tip radius [2]. Whisler and Kim [2] also stated that composite laminates tested from a blunter impactor tip with larger radius reacted with the surrounding structural members (or test support boundary conditions) leading to the observation that damage may be generated away from the impact location as the contact area increases (i.e., more blunt). Quasi-static loading from a D-shaped aluminum vs. rubber impactor showed that the stringer stiffened panels contained localized damage modes for the aluminum impactor compared to the rubber impactor that generated damage away from the impact location, as well as local damage at the impact site [6].

HEWABI accidents studied from the Federal Aviation Administration (FAA)-funded project [4, 6] were found to generate only a small dent depth on the external skin-side, which is not an easily-detectable visual damage indication, while in actuality the internal structure was very severely crushed (i.e., repair scenario per FAA AC 20-107B [7]). HEWABI Frame panels were a partial composite structure with reinforcing internal components, such as hat stringers, shear ties, and C-frames. Dynamically loaded FrameXX panels (XX is ID: 03 and 04) from the wide area cylindrical hollow rubber impactor at speed of 0.5 m/s experienced discrete shear tie failure or C-frame failure at about 4 cm of skin displacement under the impactor bumper as shown in load-displacement profile in Figure 1.4.1.1. Composite skin of the dynamically loaded Frame panels was undamaged, but left only minor, permanent deformation (less than 6 mm) at the impact location. Since this minor residual "dent" is spread out over ~1m length scale, the visual detectability was nil, as the tested Frame03 panel shows in Figure 1.4.1.2.

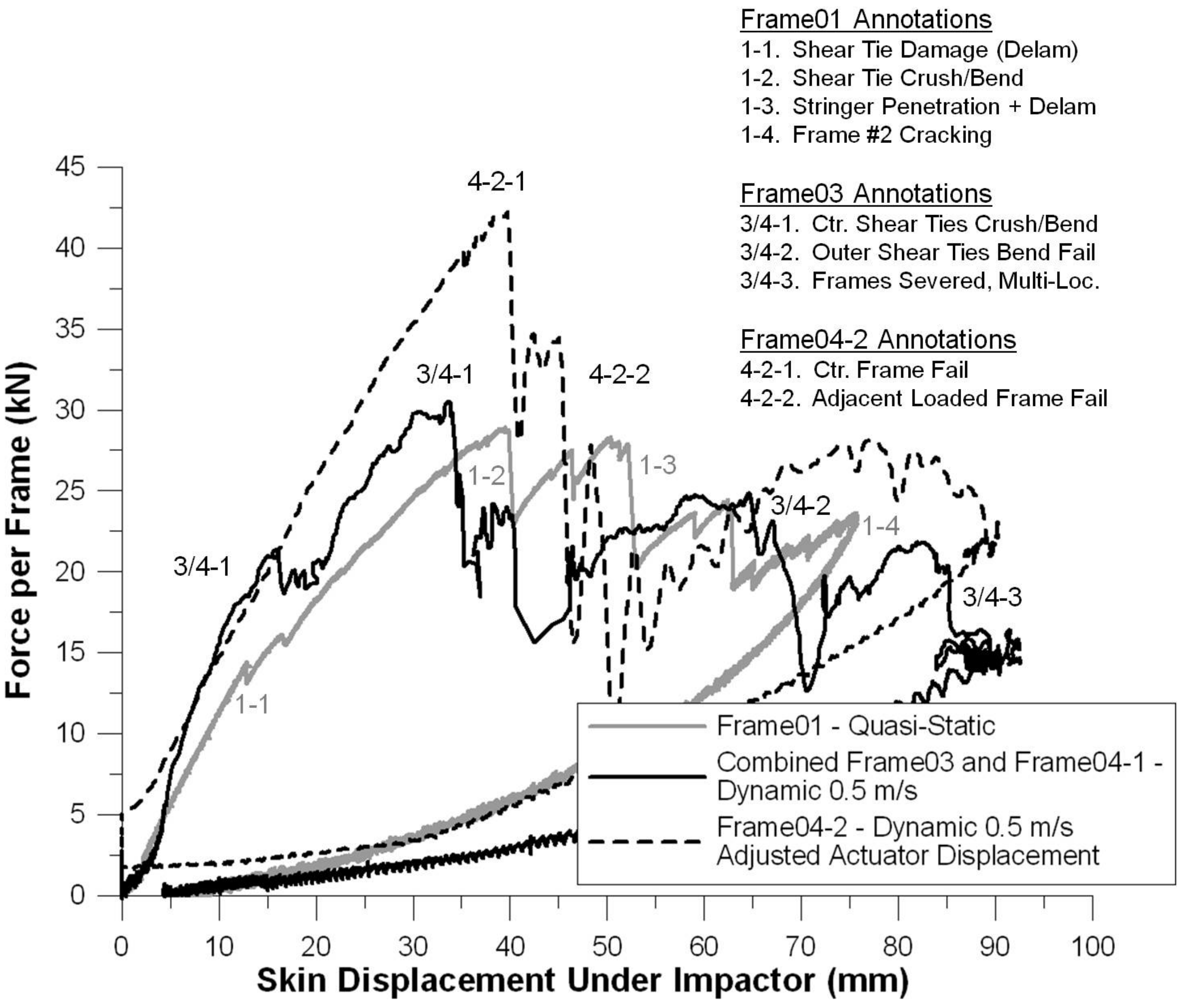

Figure 1.4.1.1 Frame panels load history comparison [4]

Quasi-statistically loaded FrameXX panels (01 and 02) from wide area cylindrical hollow rubber impactor had complete/partial cracked discrete shear ties at about 4 cm displacement and stringer damage slightly past 5 cm. These quasi-statistically tested panels were less severely damaged compared to the dynamically loaded panels. Quasi-statically loaded Stringer03 panel from D-shaped rubber bumper experienced stringer heel crack and disbond [6]. Stringer disbond damage was generated on the stringer that was loaded, but away from the impact location near the fixed boundary. Impact also generated barely visible skin damage on the stringer stiffened region as shown in Figure 1.4.1.3. Thus, blunt impact damage generated from rubber material is subject to much more complex, non-local damage modes on composite structures.

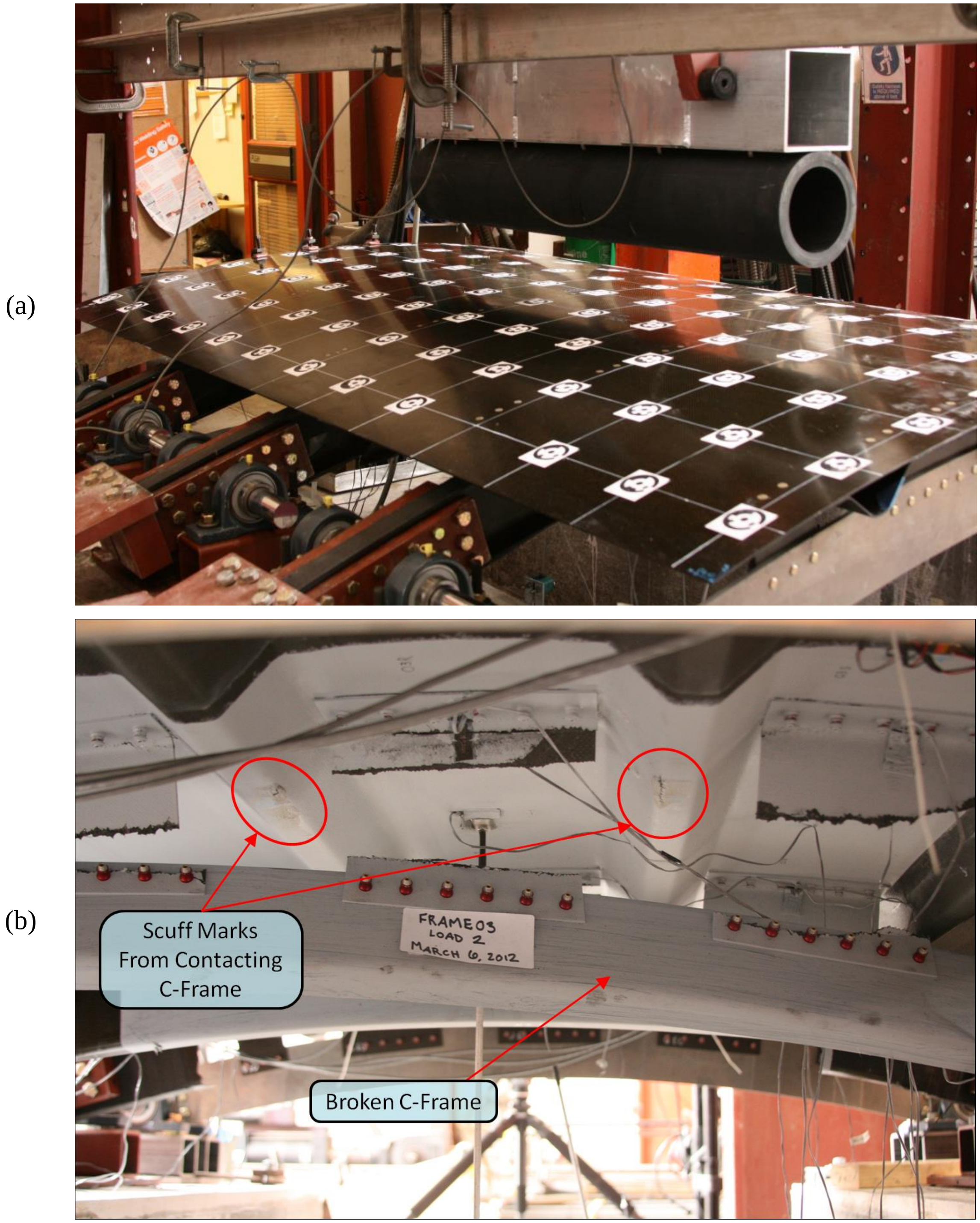

Figure 1.4.1.2 Frame03 panel after loading 2: (a) external view and (b) internal view [4]

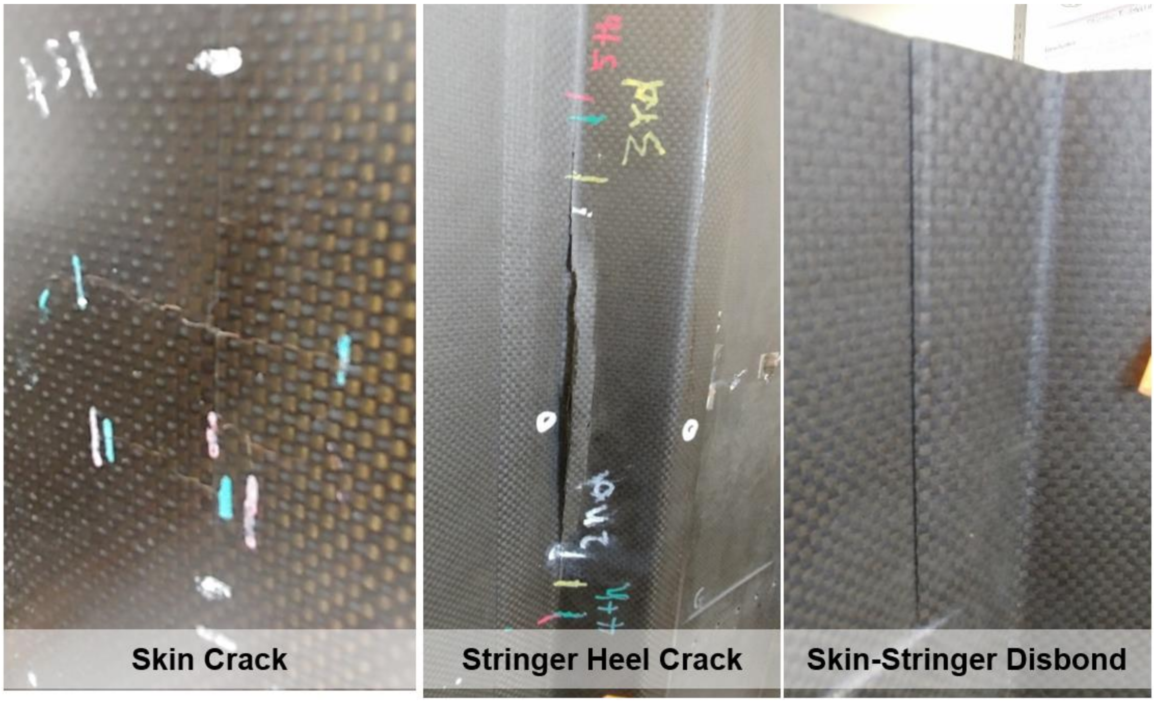

Figure 1.4.1.3 Damage modes on Stringer03 panel

1.4.2. Guided Waves

Guided waves were identified by Lord Rayleigh and Horace Lamb in the form of surface waves (Rayleigh waves) and plate waves (Lamb waves) [8, 9]. Today, "guided wave" refers to the Rayleigh-Lamb wave as a general term. Guided wave is formed from superposition of the reflected waves within the traction-free (i.e., free surface) boundaries of a thin plate, generally thinner than a wavelength, that propagates in symmetric and antisymmetric wave modes. Transcendental equation, also known as the Rayleigh-Lamb equation, derived from Helmholtz decomposition of the equation of motion is used to describe the dispersion curves for symmetric and antisymmetric modes of an isotropic plate [10]. Principles of the guided wave propagation, and experimental and model simulation methods for guided waves-based damage detection with various signal processing technique perspectives to distinguish damage, have been well-summarized by renowned researchers [10-12].

Numerous damage detection methods using guided waves have been established over a few decades after the first guided wave-based damage detection study was validated [13]. Guided waves were investigated to have dependable sensitivity to the damage based on frequency-thickness values of the wave modes: both numerical and experimental results verified that specific frequency-thickness value has higher sensitivity to the notch damage depth level based on the wave attenuation level results [14]. Dispersion curve shifting of the lowest symmetric and antisymmetric modes was experimentally validated from progressive stiffness reduction of the composite laminate from the cyclic tension fatigue damage [15]. Composite laminates with a through-hole, matrix crack and delamination damage types were studied at low frequency guided wave tests at 15 and 50 kHz, and the guided wave test results of different damage modes showed that the low frequency A0 wave results contained sufficient information to identify the damage mode [16]. Low frequency guided wave test is advantageous from the analytical perspective since no higher guided wave modes, except first symmetric and antisymmetric modes, are generated. Multi-layer delamination damage formed from low energy impact on composite laminate was detected from attenuation of A0 guided wave mode from interaction with the damage [17]. Power spectrum density amplitude decreased when guided waves propagated directly through the multi-layer delamination damage, but guided wave energy amplitude increased when the guided waves propagated were received at ±30 to 45 degrees off from the damaged site (actuator to receiver at same distance), due to the constructive interference of guided waves reflected from the damage.

Propagation of guided waves through complex boundary conditions was reviewed to help understand wave transmissivity behavior through complex composite structures (e.g., multi-part bolted assemblies) as studied in this dissertation. Guided waves through thickness-varying regions have been studied to cause wave scattering and mode conversion whether the thickness variation is from taper up or down [18]. However, guided waves through tapered thickness change showed minor reflection of the waves compared to step thickness change. Also, guided wave transmission rate through bolted joint structure was studied to identify bolt loosening [19]. Wave energy transmission through outer skin component increased as the fasteners loosened, since reduction of true contact area between bolted joint components leads to lower energy leakage into the fastened components. Guided wave transmission through the bolted-joint region of two large plates was examined with minimal interference of the waves from boundary reflection at various frequencies and torque levels [20]. Guided waves through a bolted joint interface were observed to be consistent past 2.26 N·m torque level at frequency below 320 kHz.

1.4.3. Residual Strength Estimation

Linear elastic fracture mechanics (LEFM)-based residual strength estimation for composite laminate has been developed from an experimental study [21]. Notched composite laminates were tested for residual strength from various notch types and the test results showed that the notch length affected their strength whereas discontinuity shape did not [22]. A two-parameter model for composite laminate residual strength estimation has been developed and the experimental results showed great estimation accuracy even for large holes [23]. This two-parameter model was further developed to estimate residual strength of blunt impacted composite laminates by correlating the impact energy level to the notch size [24].

Some aspects of residual strength estimation from NDE results were investigated. Residual interlaminar shear strength and ultrasonic wave attenuation rate of the composite laminate was examined correspondingly to the void content percentage levels separately [25].

Composite laminate residual interlaminar strength estimation from the ultrasonic attenuation slope was implemented after attenuation slope to the void content level relationship was empirically determined [26].

2. UGW Test on HEWABI Panels

Complex composite panels from High Energy Wide Area Blunt Impact (HEWABI) tests (i.e., GSE accidents) [4, 6] generated significant damage modes on the internal structural components, such as disbonded skin-to-stringer joints and severely cracked shear ties, C-frames, and stringers, without indication of such damage from the external skin view as shown in Figure 1.1.2 and Figure 1.4.1.3. As stated in the previous chapter, the main objective of the research was to utilize UGW test methods to detect and characterize blunt impact damage modes on composite structures. This chapter reviews contact- and non-contact-based UGW test methods that achieved detection of major damage modes in the internal structure of complex composite panels only from the external skin-side as shown in Figure 1.2.1.

Contact-based UGW tests were performed on HEWABI specimen Frame02 panel [4, 6] for damage detection within its bolted joint internal components. UGW tests were conducted systematically on Frame02 panel (see Figure 1.2.3) to understand UGW behavior through each component prior to UGW-based internal structure damage scanning of the complex assembled panel. First, UGW transmission and its sensitivity to damage were explored on individual components of the composite panel: C-frame, shear tie, and stringer co-cured skin. Second, UGW tests were performed from the external skin-side on an assembled/disassembled panel to comprehend propagation of guided waves through bolted joint interfaces on the internal frame path. Finally, UGW transmission from single skin excitation through split wave paths (see Figure 1.2.2) was further explored: waves through the internal frame and stringer path compared to the external skin path. Analysis of the transmitted UGWs through bolted joint interfaces on the internal frame path was assisted from the supplemental experiments performed on the bolted joint composite plates.

Non-contact-based UGW tests were performed on HEWABI specimen Stringer03 panel for damage detection on the stringer. Air-coupled transducers were utilized to eliminate couplant application process and were mounted on a wheeled-cart to rapidly scan along the length of the stringer. Non-contact scanning method was developed to improve contact-based stringer scanning method performed on Frame01 and 02 panels (contact-based scanning will not be discussed herein) [27].

Most of the work presented in Chapter 2 was a collaborative work with Margherita Capriotti. From preliminary studies in understanding UGW behavior on composite structure's complex wave paths to detecting major damage modes on composite panels, all work was thoroughly discussed with her. Especially, damage detection using statistical outlier analysis with damage index to identify location of the damage was mainly her work.

2.1. Panels Overview

Blunt impact tested sub-component level composite panels were fabricated from Cytec X840/Z60 12k unidirectional tape and 6k woven fabric prepreg [4]. All composite parts were autoclave cured at San Diego Composites (SDC) at cure temperature of 170 C (350 F). Laminate layup sequences and material properties of the elemental parts are listed in Table 2.1.1 and Table 2.1.2, respectively. Shear ties and C-frames were mechanically fastened to the co-cured skin-stringer shell as a representation of a portion of a fuselage structure of a wide-body composite aircraft in a region that is vulnerable to GSE accidents.

Frame02 panel, investigated via contact-based method in this chapter, was quasi-statically loaded at 3 mm/min by a hollow cylindrical rubber bumper at the center of the stringer (Figure 2.1.1) and the damage modes generated within the internal structure are as shown in Figure 2.1.2. This panel experienced crack damage mode on the skin, shear ties, stringer and C-frame in sequential order. Major skin crack damage was generated only on Frame02 panel out of four FrameXX panels, but regardless of the skin damage, Frame02 panel was investigated for bolted joint internal component damage detection because it was the only FrameXX panel containing continuous internal wave path with partially cracked shear ties.

Table 2.1.1: Laminate layup information [6]

Element	Material	Layup Sequence (Degrees)	Thickness (mm)
Skin	Tape, with 6K fabric ply on each outer face	$[0/45/90/-45]_{2S}$ 0° dir. along stringer direction	2.65
Stringer	Tape, with 6k fabric ply on each outer face	$[0/45/-45/90/45/-45/0]_{S}$ 0° dir. along stringer main axis	2.37
Shear Tie	Fabric	$[\pm 45/0]_{3S}$ 0° dir. perpendicular to skin	2.5
C-frame	Fabric	Web: $[\pm 45/0]_{3S}$ Flange: $[\ \pm 45/0/0/\pm 45/0/\pm 45/0]_{S}$ 0° dir. along frame main axis	Web: 2.50 Flange: 2.92

Table 2.1.2: X840 Z60 carbon/epoxy lamina elastic properties [6]

Material	ρ (g/cm3)	E1 (GPa)	E2 (GPa)	ν12	G12 (GPa)	G13 (GPa)	G23 (GPa)
Tape	1.63	168	10.3	0.27	6.89	6.89	3.72
Fabric	1.61	80.0	80.0	0.06	6.48	5.10	4.07

StringerXX panels were manufactured from the same material and layup as the FrameXX panels. Stringer03 panel, investigated via non-contact-based method in this chapter, was quasi-statically tested at 12 mm/min with a D-shaped rubber bumper at the center of the stringer across and along the hat stiffened region between the shear ties. Stringer disbond damage was discovered to extend along the stringer away from the loaded zone from a hand-held UT A-scan, even though the D-shaped bumper was a localized indentation load, as shown in Figure 2.1.3. Barely visible skin crack and severe stringer heel crack damage modes were located at the loaded region, and skin-stringer disbond damage was located near the tip of the stringer heel crack damage to the end of the panel (white hatched zone on stringer flanges in Figure 2.1.3).

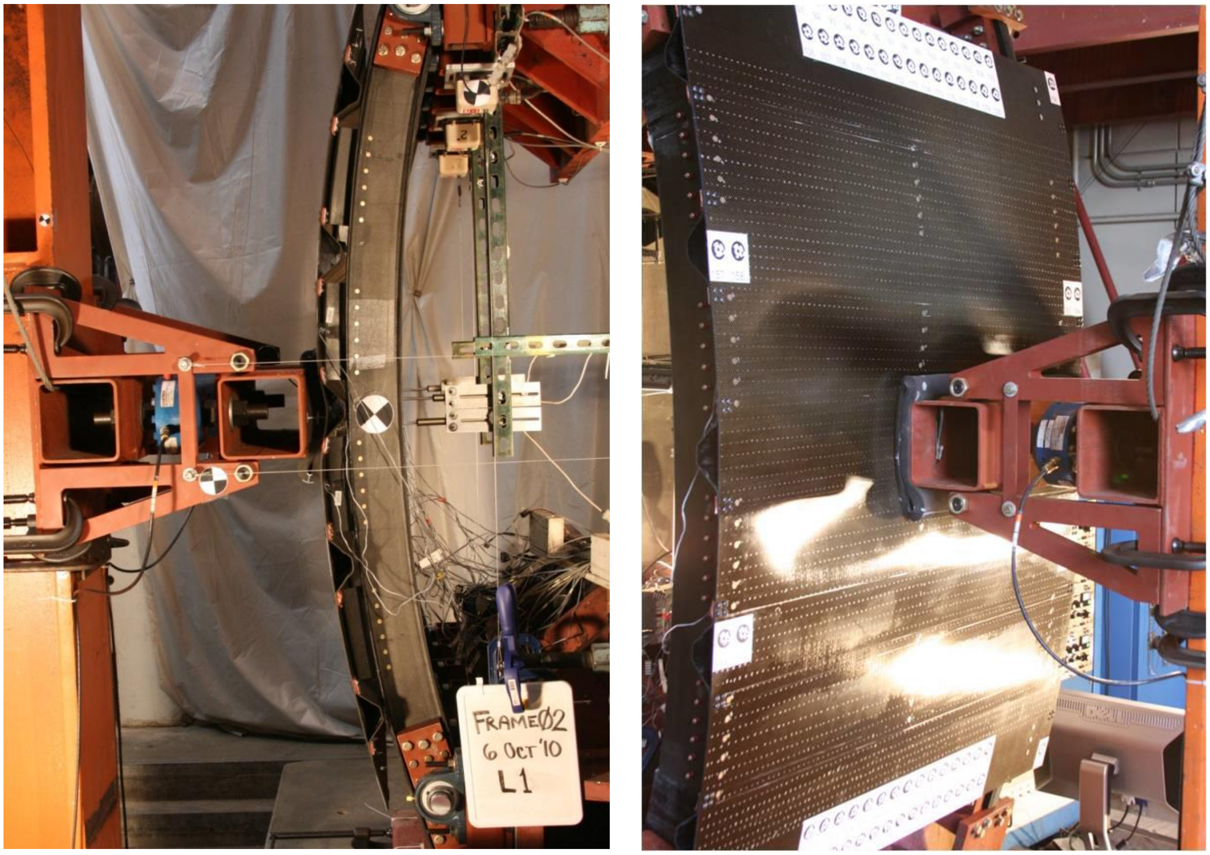

(a) (b)

Figure 2.1.1. Frame02 panels with at (a) Load1 (side-view) and (b) Load2 (skin-view) [4]

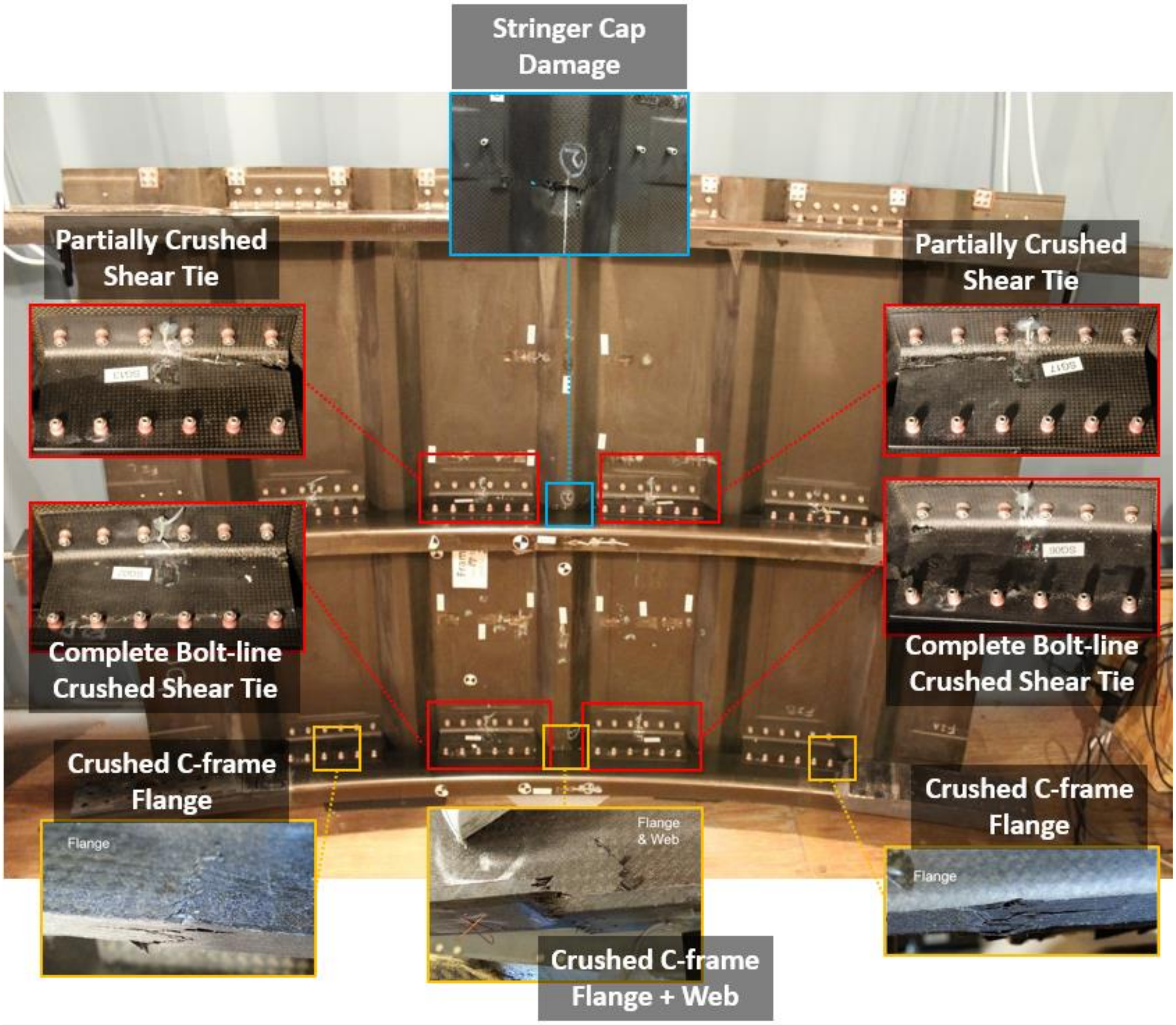

Figure 2.1.2. Frame02 panels with internal damage modes

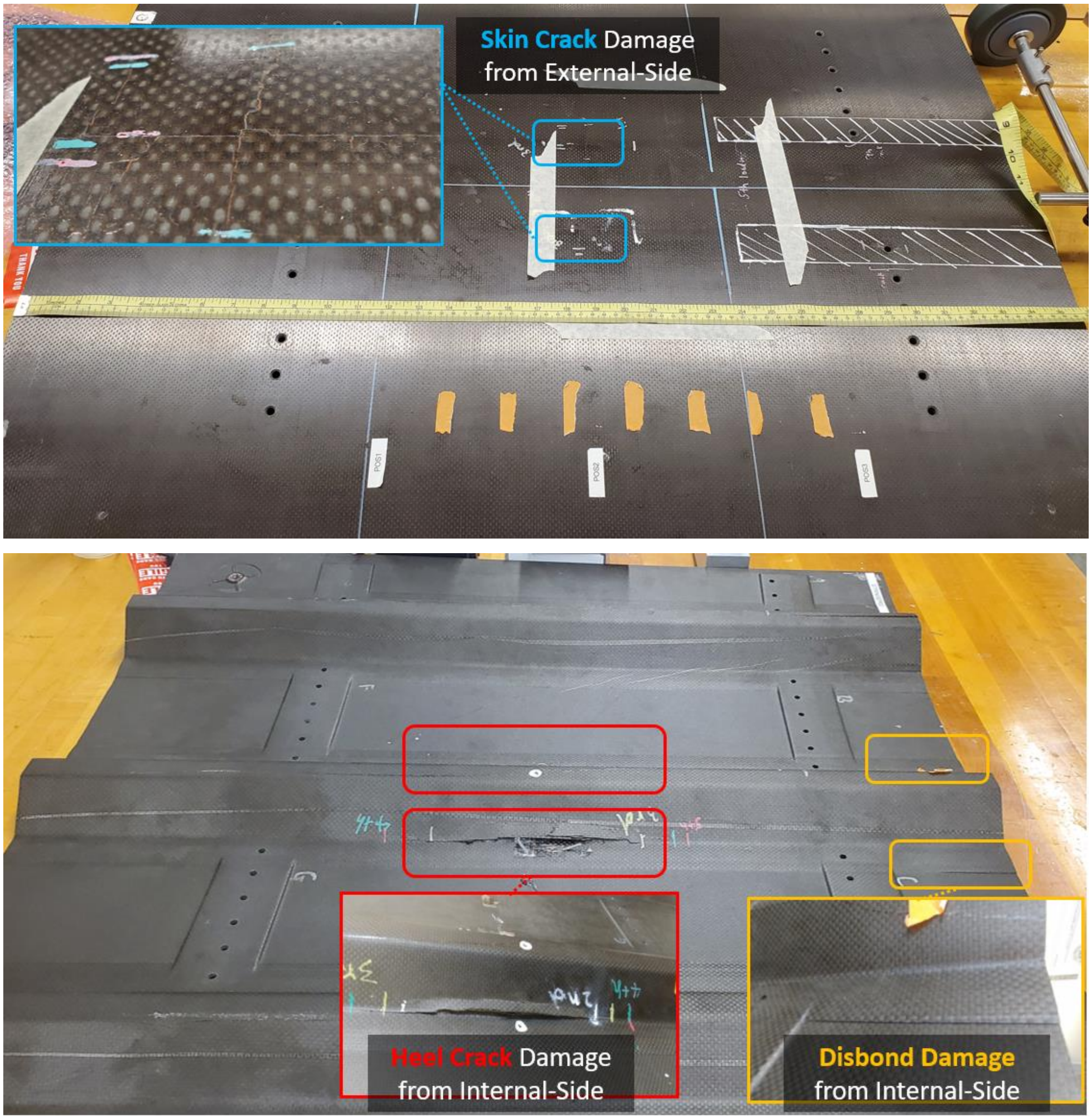

Figure 2.1.3. Stringer03 Panel exterior (top) and interior (bottom) view with damage modes from rubber bumper blunt impact

2.2. Preliminary UGW Tests on HEWABI Frame02 Panel

2.2.1. Preliminary UGW Tests Experimental Setup

UGW tests were conducted on individual components of the Frame02 panel to investigate guided wave propagation through each component. UGW transmission through composite panel parts with complex waveguides (i.e., curvature, thickness variation, bolted joint interface, and more) were experimentally examined at ultrasonic frequency range of 50-500 kHz. Such frequency range was focused on to transmit and receive significantly strong signals through complex waveguides over long distances of the panel. Preliminary UGW tests were performed with PICO or R15S transducers from Mistras with PicoScope 4824 as a function generator and an oscilloscope to generate and acquire guided waves (see Figure 2.2.1.1). PicoScope6 software was used to control PicoScope 4824. Linear amplifier and preamplifiers were used to condition the signals for better signal-to-noise ratio (SNR) than the tests with transducers only.

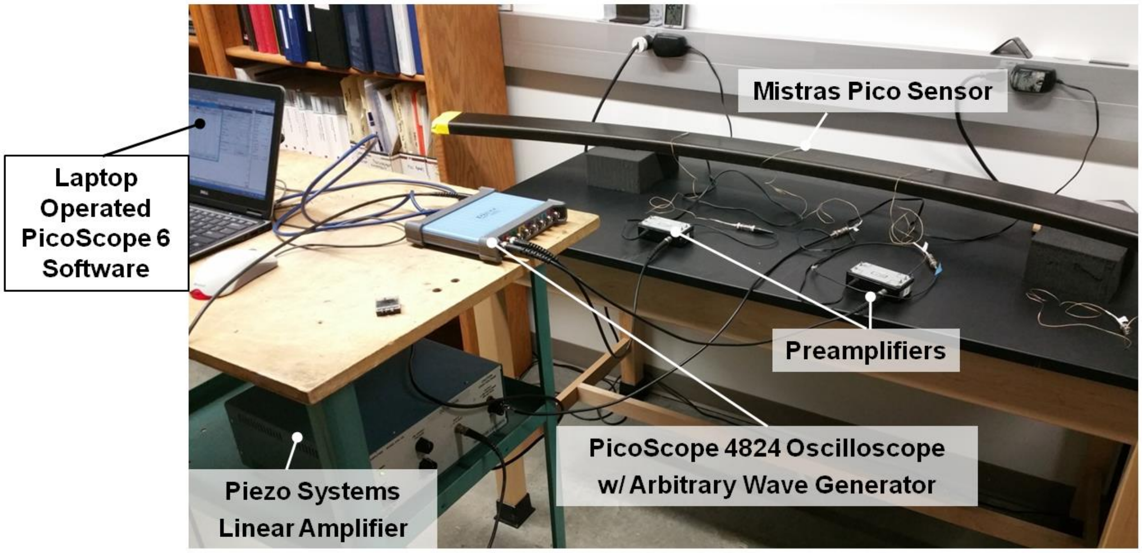

Figure 2.2.1.1. Preliminary UGW test system setup for a C-frame

First, UGW tests were executed on pristine and flange cracked C-frames to examine UGW sensitivity to the damage on the C-frame. Excitation and reception PICO transducers were wax coupled onto the C-frame at 305 mm distance apart from each other as shown in Figure 2.2.1.2. Both pristine and damaged C-frames were tested by a differential scanning approach to compare the UGWs of the symmetric wave paths (see Figure 2.2.1.2). A five-cycle Hanning window gated sine tone burst was excited by the waveform generator on the PicoScope 4824.

After the transmitted UGWs on pristine C-frame were observed to not deliver symmetric waves through its symmetric structure, UGW propagation through the C-frame was further investigated. Initially, test specimen to the transducers' coupling were presumed as a cause. However, after numerous coupling tests were performed on an aluminum plate, it was found that UGW measurements from minor discrepancies of coupling did not alter waveforms as significantly as the initial C-frame tests . Thus, C-frame UGW tests were re-performed to evaluate wave propagation behavior through the pristine C-frame for regions indicated in Figure 2.2.1.3. Mistras R15S contact transducers were mounted onto the center of the shear tie bolted joint regions with 3D printed transducer hold-downs. Hold-downs were held firmly onto the specimen using 3M VHB 4941 double-sided tape. 1/4" Neoprene foam was cut-to-fit inside the transducer slot of the hold-downs to provide even spring pressure on the transducer on the surface together with Ultragel II from Sonotech applied prior to being mounted. The gel coupling transducer setup described was used because the setup provided very consistent UGW test results. Same data acquisition with amplification systems was used and UGW tests from 50-250 kHz frequencies with 10 kHz increments were executed.

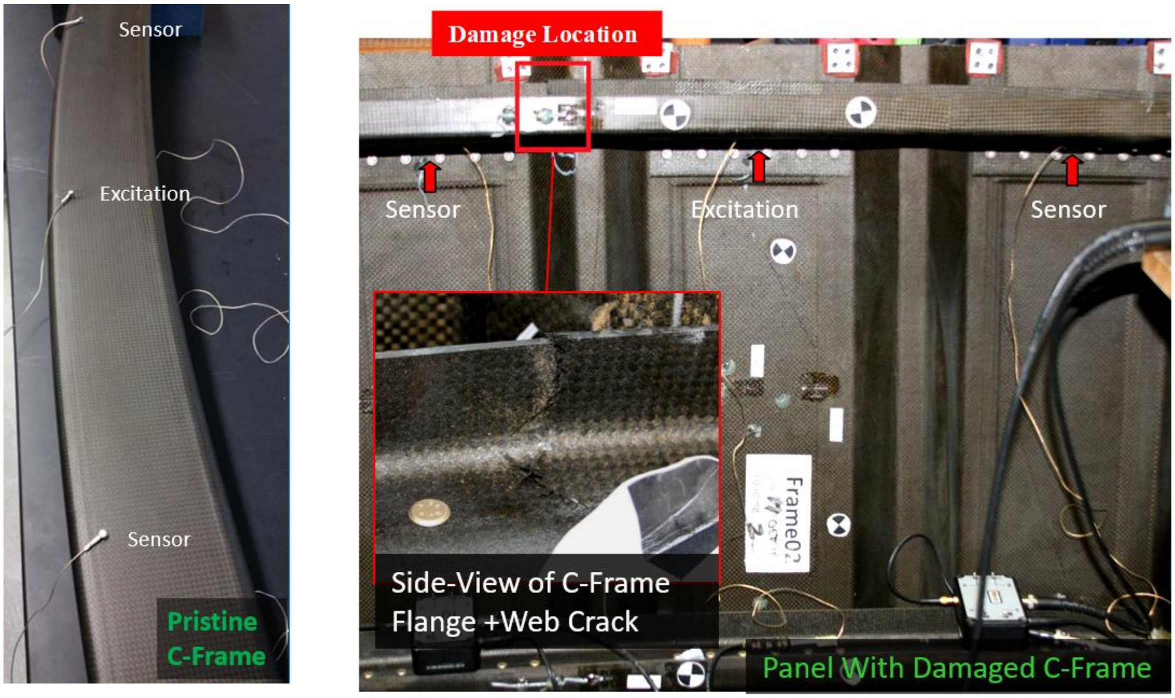

(a) (b)

Figure 2.2.1.2. Initial C-frame UGW test setup: (a) pristine C-frame and (b) impacted C-frame with through-the-flange crack

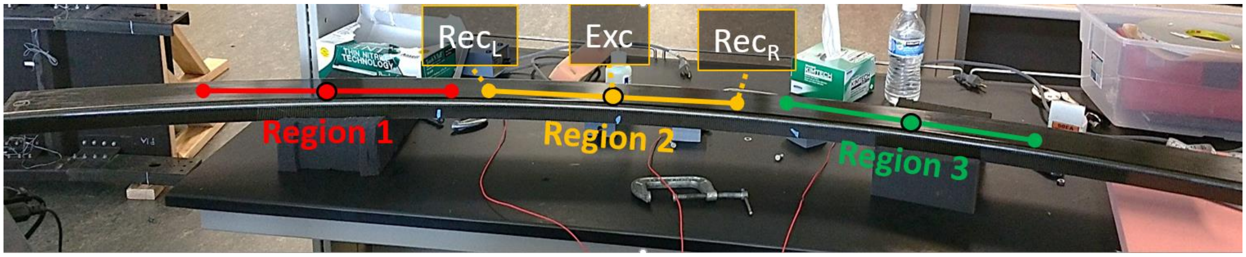

Figure 2.2.1.3. C-frame UGW test setup on pristine C-frame for symmetricity

Next, shear ties with different levels of damage severity on Frame02 Panel were UGW tested. As Figure 2.1.2 shows, two shear ties on the middle C-frame were partially cracked through the corner of the shear ties about half-way, and two shear ties on the bottom C-frame were fully crushed along the bolt-line of the C-frame. Excitation was generated from the center of the shear tie joint and received from the C-frame at the edge of the shear tie fastened region (see Figure 2.2.1.4.a, b and c). Shear tie UGW tests were conducted with shear ties assembled on the panel, because meaningful results were not identified from discrete shear tie UGW tests due to the significant interferences from boundary-reflected waves. The same UGW test system setup as previous C-frame preliminary tests was executed with R15S sensors.

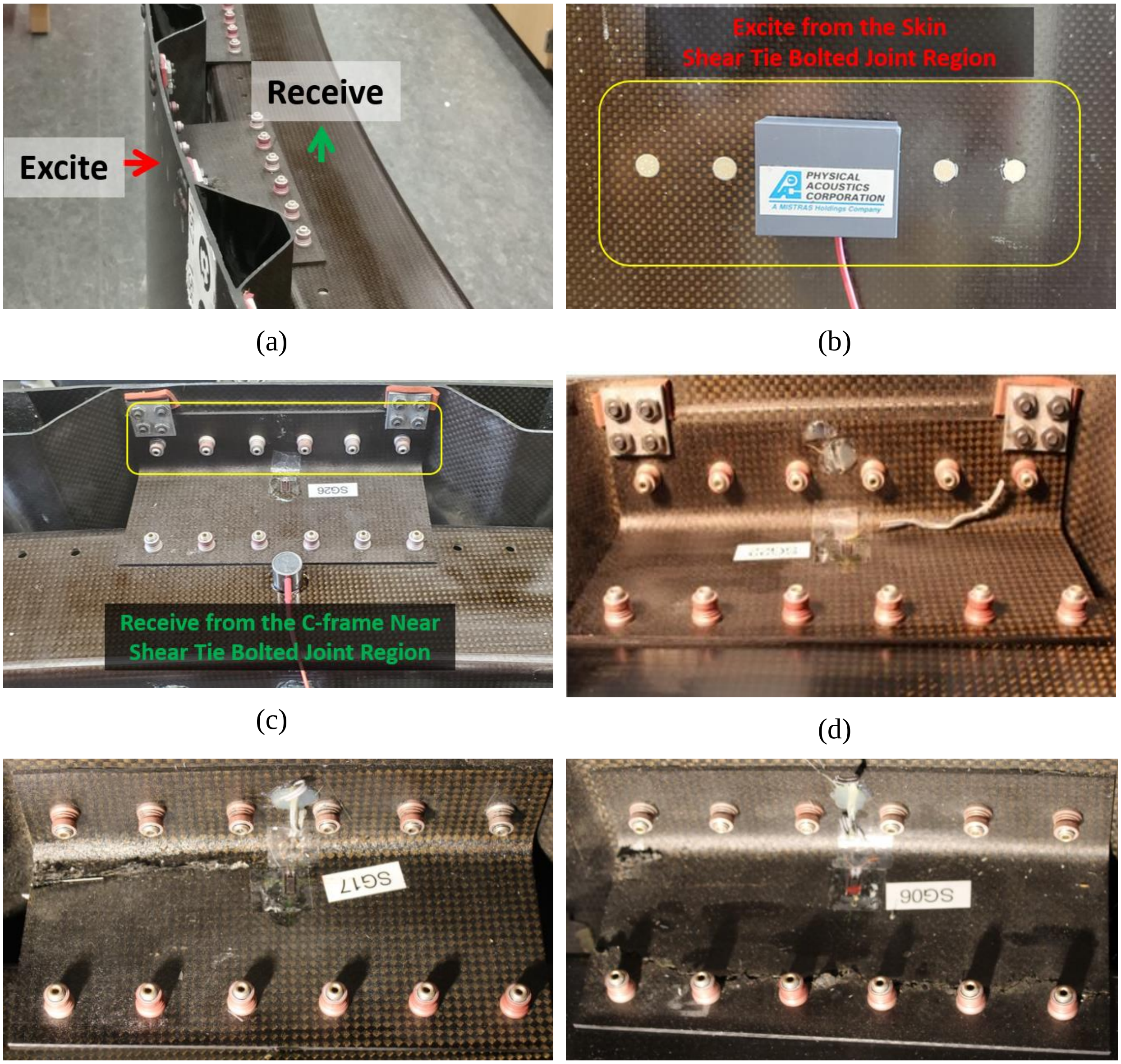

(a) (b)

(c) (d)

(e) (f)

Figure 2.2.1.4. Shear tie test setup: (a) side-view where excitation and reception is made, (b) R15S actuator on exterior skin using magnetic transducer hold down, (c) R15S receiver on C-frame, (d) undamaged shear tie (ST11), (e) partially cracked shear tie (ST06), and (f) fully cracked shear tie (ST02)

After exploring UGW transmission through shear tie and C-frame components, UGW tests were performed on the external skin-side only as a whole panel scale: actuator and receiver on bolt-fastened regions to transmit and receive UGWs through the frame path. The panel was disassembled/assembled as displayed in Figure 2.2.1.5, to examine how much of the UGWs enter into the internal frame path and exits out to the external skin. The panel was first disassembled and re-assembled as UGW tests were conducted on systematic build-up of the panel. Pristine shear ties replaced the damaged shear ties for the re-assembly UGW tests and the components were fastened with Hi-Lok pins and standard hex-nuts to 7.9 N·m torque level (the original torque level of the Hi-Lok 70-8 collars' assembly) using Dial torque wrench from CDI. Although damage existed on the cap of the hat stringer as seen in Figure 2.1.2, the damage was treated as an intrinsic defect since it did not interfere with the UGWs through the frame path. R15S transducers were mounted and remained coupled on the external skin-side at the center shear tie joint through the whole disassembly/assembly UGW tests using air-suction cups to hold a 3D-printed transducer bracket in place.

Transmitted guided waves from comparison of continuous and discontinuous internal frame paths from the panel re-assembly test on full-path (shear tie-to-shear tie) showed barely noticeable change from the external skin receiver to identify internal UGW transmitting back out to the adjacent skin-shear tie joint, as the details will be discussed in the results section of this chapter. Thus, UGW tests were conducted on a fully re-assembled complex panel with pristine shear ties at half path (see Figure 2.2.1.6) to compare transmitted UGWs from skin vs. frame paths. R15S actuator transducer was mounted at the center of the shear tie joint on the external skin surface and receiver sensors were mounted on the skin and C-frame at half of the full wave path as shown in Figure 2.2.1.6. Half-path UGW tests were performed at frequency ranges of 50-

250 kHz to obtain a frequency parameter that delivers UGWs through the internal path with least energy loss as possible by comparing UGW transmission through the skin and frame split wave path. The frame path had four fastener joints for the internally transmitted waves to propagate back out to the receiver sensor on the outer skin. Skin to shear tie joints (joints 1 and 4 in Figure 2.2.1.6) are rough to smooth surfaces, respectively, and shear tie to C-frame joints (joints 2 and 3 in Figure 2.2.1.6) are smooth to smooth surfaces, respectively. However, UGWs propagated through only two interfaces from the half-path UGW test. So, consequent wave attenuation was anticipated for the full path wave transmission and investigated from the supplemental UGW tests on simple composite plates with bolted joint rough/smooth surfaces.

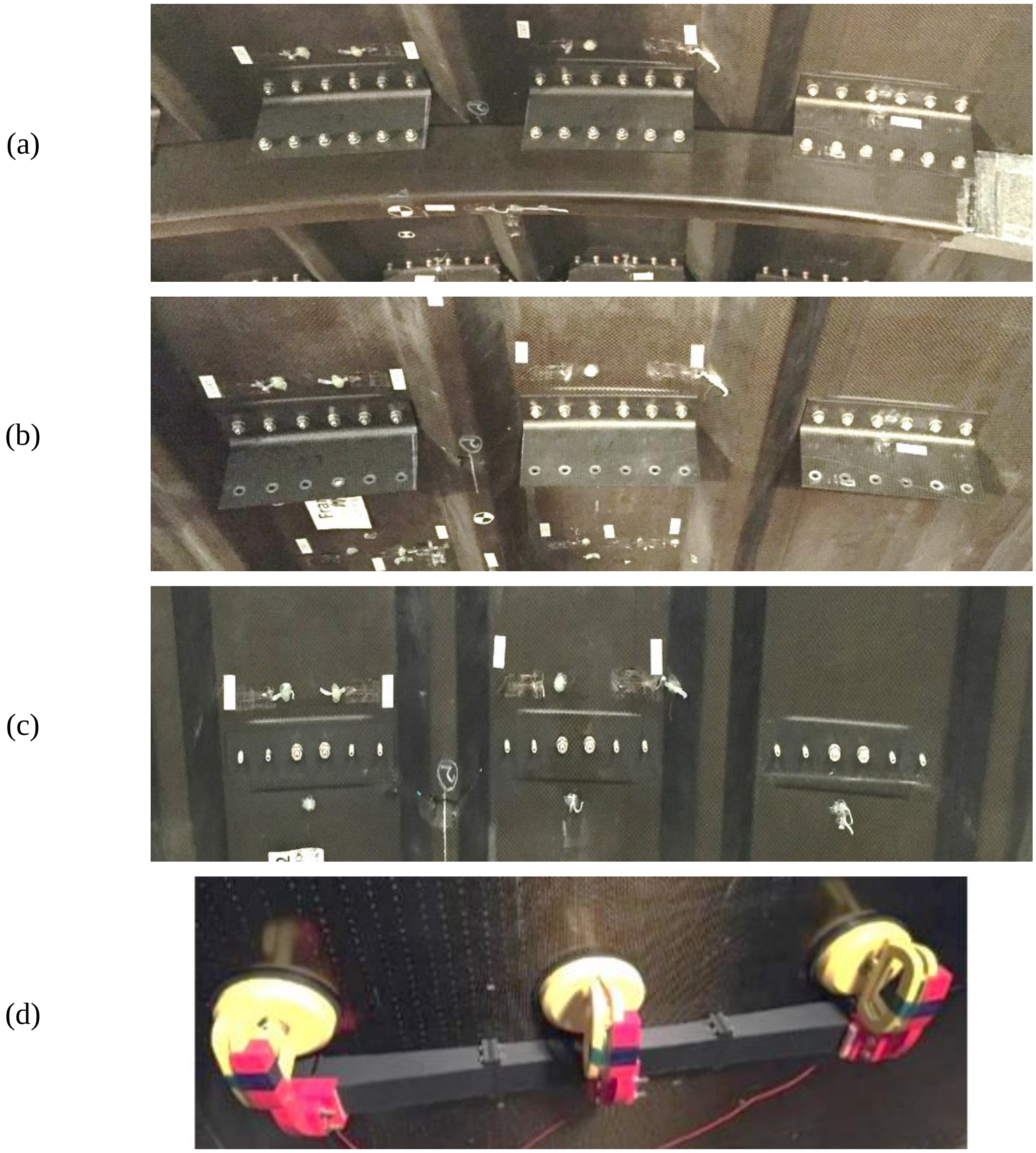

Figure 2.2.1.5. Disassembly UGW tests: (a) fully assembled panel with C-frame and shear ties, (b) C-frame removed, (c) C-frame and shear ties removed, and (d) 3D-printed hold-down bracket mounted on the outer skin

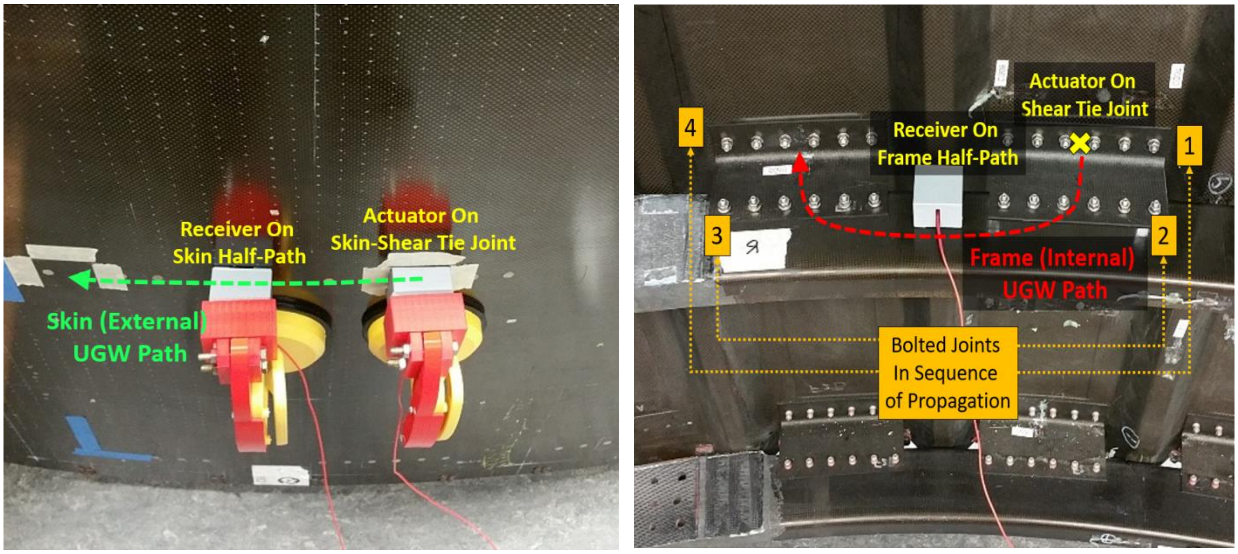

(a) (b)

Figure 2.2.1.6. Frame02 panel half-path UGW transmission test setup: (a) external side and (b) internal side

2.2.2. Preliminary UGW Test Results

Pristine and damaged C-frame UGW test results from the test configuration shown in Figure 2.2.1.2 for 80 kHz test frequency are displayed in Figure 2.2.2.1, which shows raw signals and their corresponding frequency responses. UGW results of two receiver transducers equally distanced away from the actuator transducer at symmetrical locations along the C-frame were compared. Frequency response peak values dropped nearly 55% from the damaged path compared to the undamaged path from the flange damaged C-frame (see Figure 2.2.2.1.b). Pristine C-frame test results showed 15% difference in frequency response peak values (see Figure 2.2.2.1.a), even though damage was not present on either path on the pristine C-frame. Several factors that could lead to discrepancies of the tests were investigated: majorly polar pattern of the transducer and transducer to C-frame coupling, and these factors were found to not cause significant inequality in transmitted waves when UGW tests were performed on an aluminum plate.

UGW propagation through symmetrical paths on the C-frame was further examined at three highlighted regions (see Figure 2.2.1.3). UGW tests were performed with R15S transducers with 3D-printed hold-downs and repeated at least three times by re-applying couplant for every re-mounting of transducers to confirm consistency of the test method (results confirmed to not vary from coupling). Experimental results for 50 and 150 kHz test frequencies at center region of the C-frame (Region 2 in Figure 2.2.1.3) show guided waves propagated asymmetrically through the symmetric wave path from the center region of the C-frame, as shown in Figure 2.2.2.2. Frequency response energies for test frequency range from 50 to 250 kHz at 10 kHz increments were extracted from UGW tests of each C-frame segmented region (Regions 1, 2, and 3 for left, center, and right portion of the C-frame, respectively) and were compared in Figure 2.2.2.3. Intensity of transmitted UGWs conflicts strong towards one direction than the other through symmetric waveguide, which was an unexpected behavior based on the energy results seen in Figure 2.2.2.3: transmitted wave energy was not simply stronger towards one direction, left or right (see direction defined in Figure 2.2.2.3).

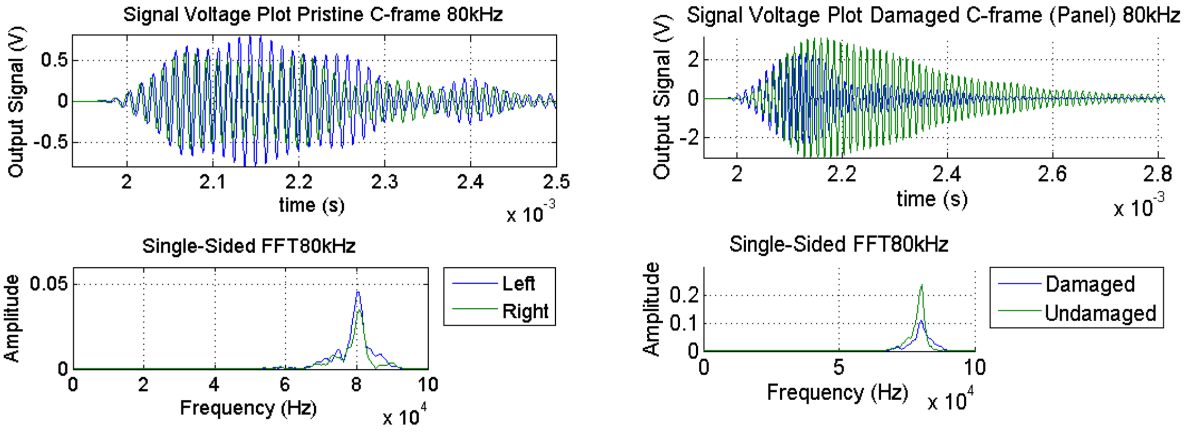

(a)

(b)

Figure 2.2.2.1. Initial C-frame UGW test result comparison: (a) pristine C-frame and (b) C-frame with through-the-flange crack

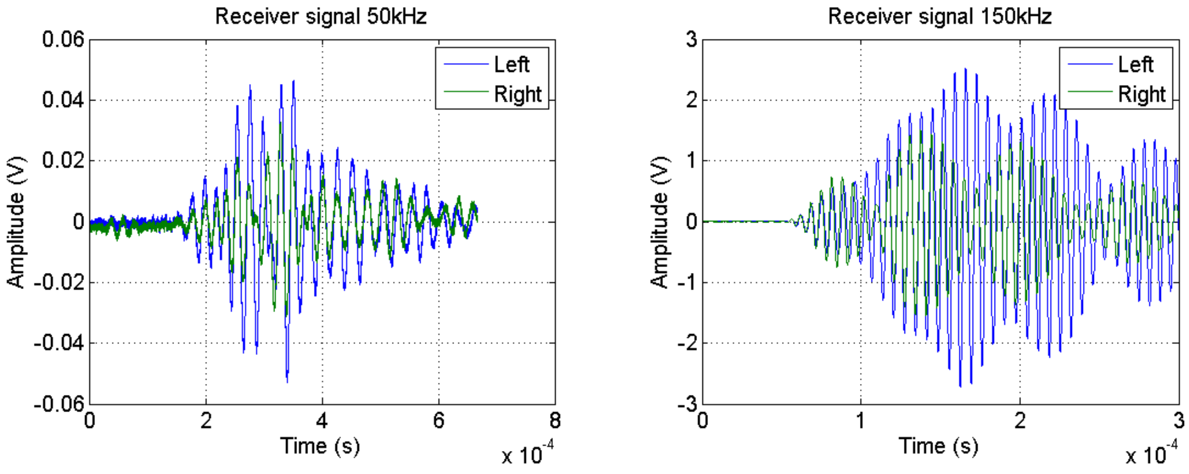

(a) (b)

Figure 2.2.2.2. UGW test on C-frame at (a) 50 kHz and (b) 150 kHz

Abaqus finite element analysis tool was used to interrogate wave transmission behavior through the undamaged C-frame with details on simulation parameters covered in Appendix A. The C-frame was manufactured with 610 mm long splice joint patches for each ply as shown in Figure 2.2.2.4, with specific stacking sequences as found from the manufacturing note for the HEWABI panel. Partitioned splice joint patches were tangentially 13 degrees offset from each patch to fabricate a curved C-frame. A C-frame with complete splice joint layup was not simulated, but single ply of 610 mm partitioned section was given 13 degrees offset to examine how severely wave transmission is affected. Figure 2.2.2.5 shows wave transmission through symmetrical path with uniform layup and single partitioned ply with 13 degrees offset. Model results from segments of single ply offset show how orientation affects transmission of the wave. Considering that C-frame is comprised of total 72 spliced joints (4 splices per ply), it is evident that angle offset definitely affects and leads to asymmetric wave transmission behavior. Also, physical C-frame has an overlap region (see Figure 2.2.2.4), where thickness and local layup are more complex than the model, which could also affect wave transmission throughout the C-frame. Due to its complex wave behavior, differential scanning approach on the frame path was not pursued herein.

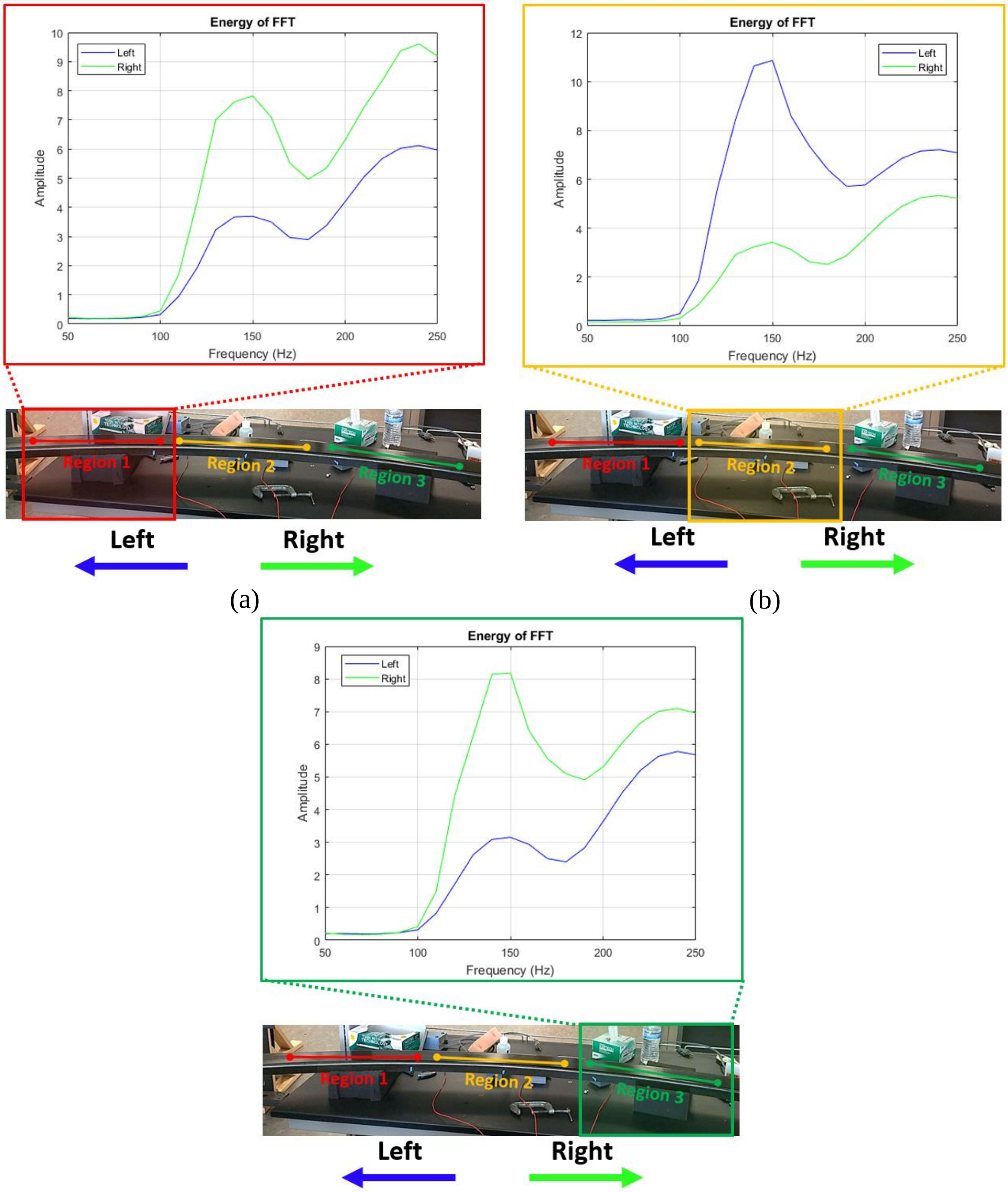

(a) (b)

(c)

Figure 2.2.2.3. Energy from the frequency response results of UGW test for regions (a) 1, (b) 2, and (c) 3 on C-frame

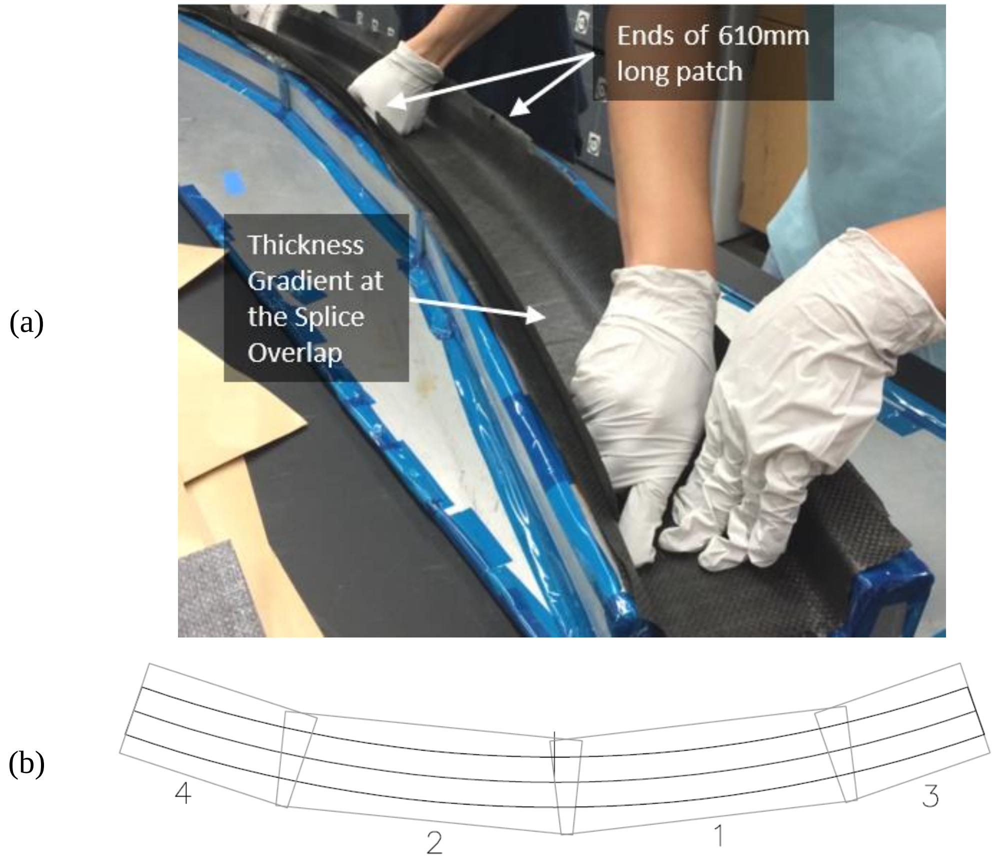

Figure 2.2.2.4. (a) Manufacturing process of C-frame and (b) C-frame first ply spliced joint layup with stacking sequences drawing

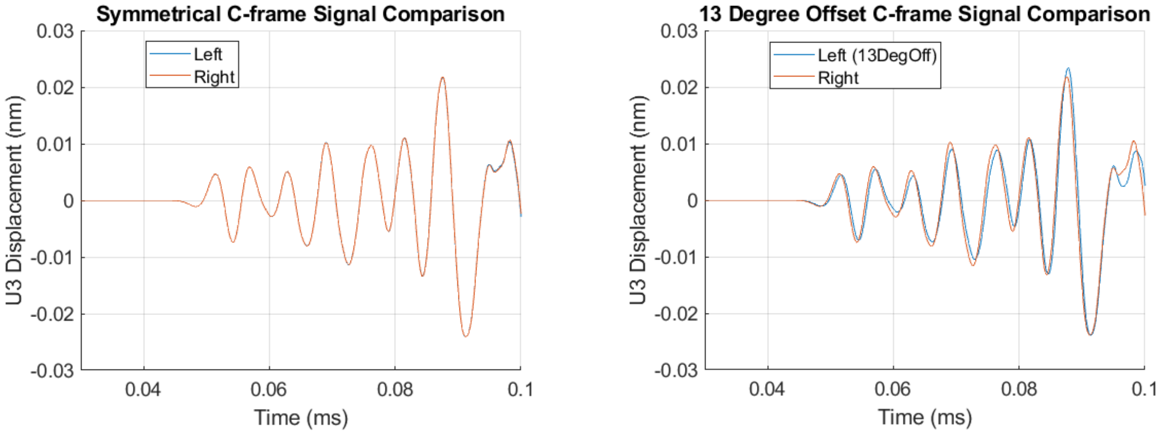

(a) (b)

Figure 2.2.2.5. FE model guided wave simulation results of pristine C-frame (a) no angle offset (b) 13 degrees angle offset on a single ply for 150 kHz test frequency

UGW test results for different shear tie damage cases on Frame02 panel were examined using 50 and 150 kHz and are presented in Figure 2.2.2.6. Hanning window gated flexural wave mode of each shear tie from R15S transducer receiver (Figure 2.2.1.4.c) were compared for the pristine (ST11 in Figure 2.2.1.4.d), partially cracked (ST06 in Figure 2.2.1.4.e), and fully cracked (ST02 in Figure 2.2.1.4.f) shear ties. Comparing the FFT peak values of test frequencies, wave energy reduced at 78% and 18% through the partial corner cracked shear tie and the pristine shear tie at 150 kHz and 50 kHz, respectively. Test frequency of 150 kHz showed remarkable sensitivity to the shear tie damage. However, UGW transmission studies through multiple bolted joint interfaces found 150 kHz test frequency is not suitable for the internal frame path wave transmission, which will be discussed further in the following section.

Frame02 panel with damaged shear ties replaced to pristine shear ties at the middle frame region (see Figure 2.2.1.5.a) was UGW tested with actuator and receiver transducers mounted on the external skin surface to analyze wave transmission through full frame path. UGW test results for 150 kHz test frequency for different panel configurations are shown in Figure 2.2.2.7. Whole panel configuration (Figure 2.2.1.5.a) result compared to the skin-only panel configuration (Figure 2.2.1.5.c) delivered 86% reduced wave energy based on max peak value difference of the first wave packet as displayed in Figure 2.2.2.7.a. Also, comparing the UGW test results of C-frame disassembled configuration skin+shear ties (as seen in Figure 2.2.1.5.b) to the whole panel configuration shows a contradicting result from the anticipated waveform: peak value of the wave packet increased when the C-frame was disassembled from the panel as displayed in Figure 2.2.2.7.b. Increased wave transmission through external skin-side with disassembled C-frame is thought to be caused by the following: discontinuous wave path reflected the UGW transmitted through the skin path to the adjacent shear tie joint, frame path transmitted wave had destructive interference with skin path transmitted wave, and/or the weight of the C-frame caused bending moment to change the bolted joint interfacial contact area. Regardless, the difference in transmitted waves through the C-frame disassembled configuration was considered trivial to possibly estimate frame path transmitted energy almost completely attenuated at test frequency of 150 kHz.

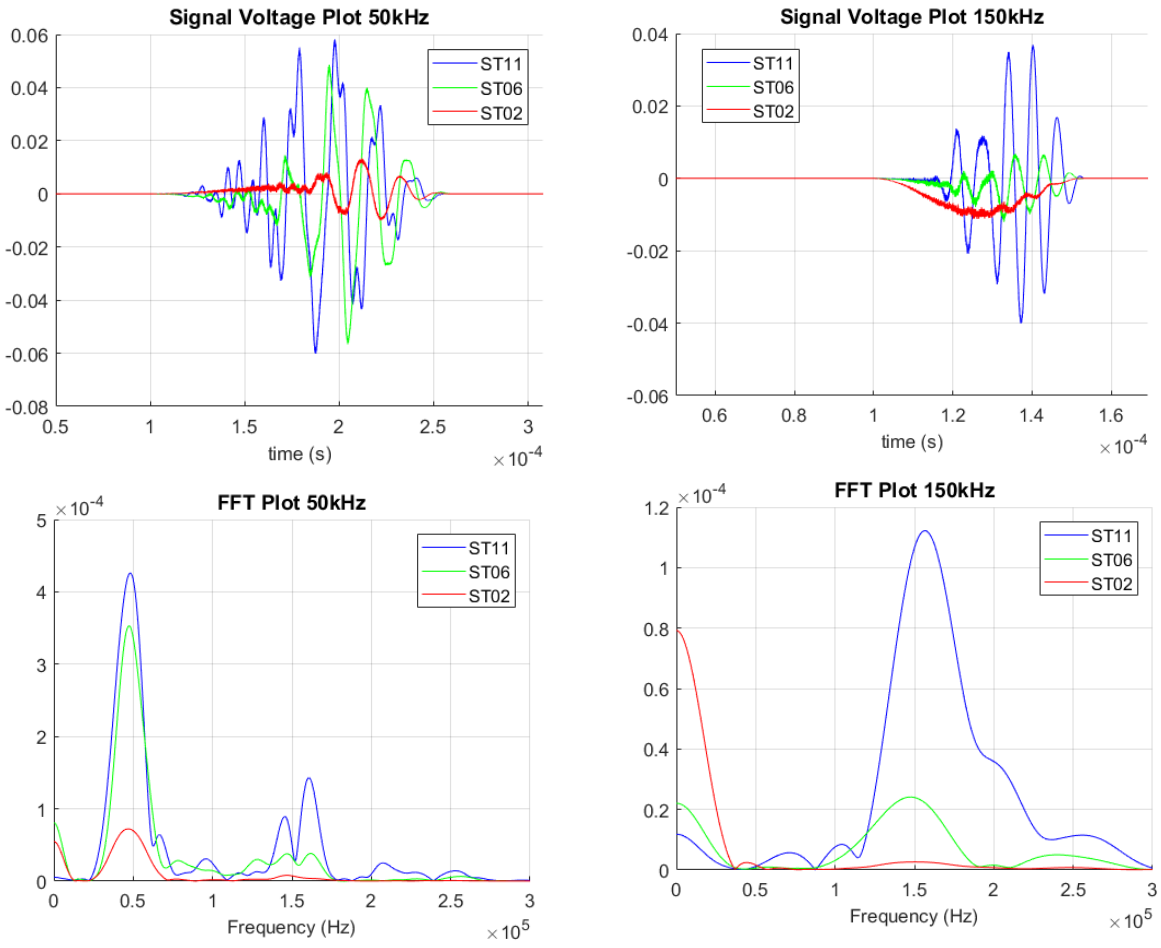

(a) (b)

Figure 2.2.2.6. Shear tie test results comparison: (a) signal and FFT result 50 kHz and (b) signal and FFT result 150 kHz

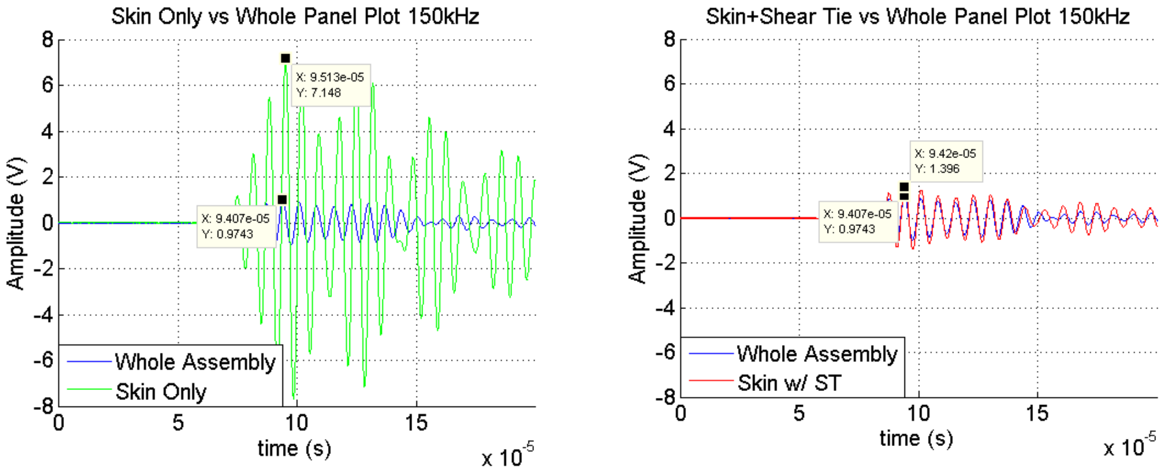

(a) (b)

Figure 2.2.2.7. Systematic UGW test results at 150 kHz: (a) Full assembly vs C-frame + Shear Tie disassembled and (b) C-frame disassembly vs C-frame + Shear Tie disassembly

Half-path UGW tests (test configuration as in Figure 2.2.1.6) were performed from 50 to 250 kHz test frequency range, followed by full-path UGW analysis from panel assembly tests. Half-path test results of 50 kHz and 150 kHz are displayed in Figure 2.2.2.8. Half-frame path (internal) transmitted waves received on the C-frame is discernably high compared to the half-skin path (external) transmitted waves on skin at 50 kHz. In contrast, internally transmitted waves through the C-frame is remarkably lower than the external skin transmitted energy at 150 kHz. It should be noted that UGW through full frame-path further attenuates through two additional bolted joints (joints 3 and 4 in Figure 2.2.1.6), while UGW through full skin-path merge with UGW propagated through the stringer, conceivably in a constructive manner. Wave energy loss through bolted joint interfaces from Frame02 panel is supported in later sections -- study of wave penetration through bolted joints' relationship to the frequency.

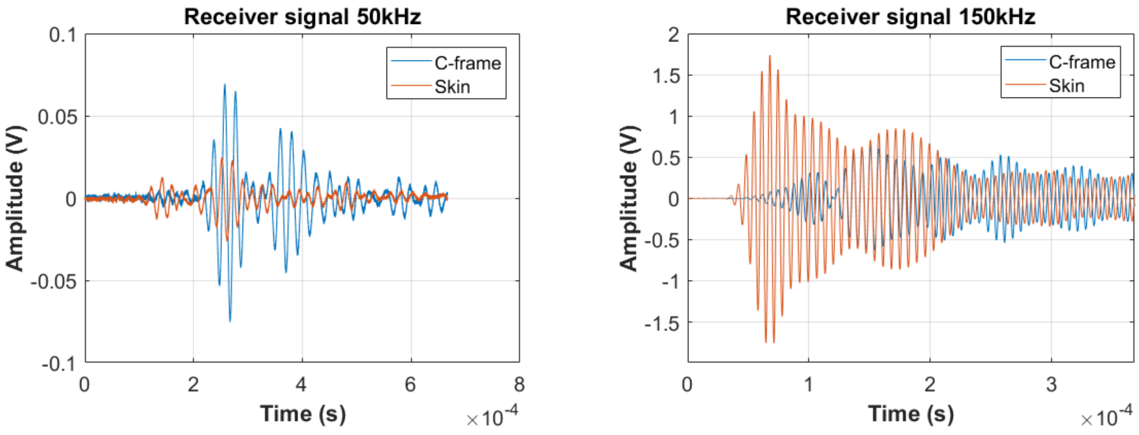

(a) (b)

Figure 2.2.2.8. Frame02 Panel UGW test raw signals comparison between receiver on skin surface and on C-frame at (a) 50 kHz and (b) 150 kHz

2.2.3. Supplementary Bolted Joint Composite Plates

2.2.3.1. Bolted Joint UGW Experimental Setup

A Hexcel 282/SC-780 (carbon fabric/epoxy) large plate was fabricated through the Vacuum Assisted Resin Transfer Molding (VARTM) process in $[0]_{10}$ layup; three 270 mm x 210 mm plates in 2.4 mm thickness were trimmed out from the large plate. The three plates were jointly bolted as shown in Figure 2.2.3.1.1 and a UGW experiment was executed for two types of surface joints: rough surfaces joint (vacuum bag-side surfaces) and smooth surfaces joint (tool mold-side surfaces). As stated by Yang and Chang [19], the true contact area between bolted joint surfaces determines the transmitted and leaked wave energy through the joint components. Different surface joints were studied to help understand UGW propagation through this complex composite panel as it has mixed surface joints.

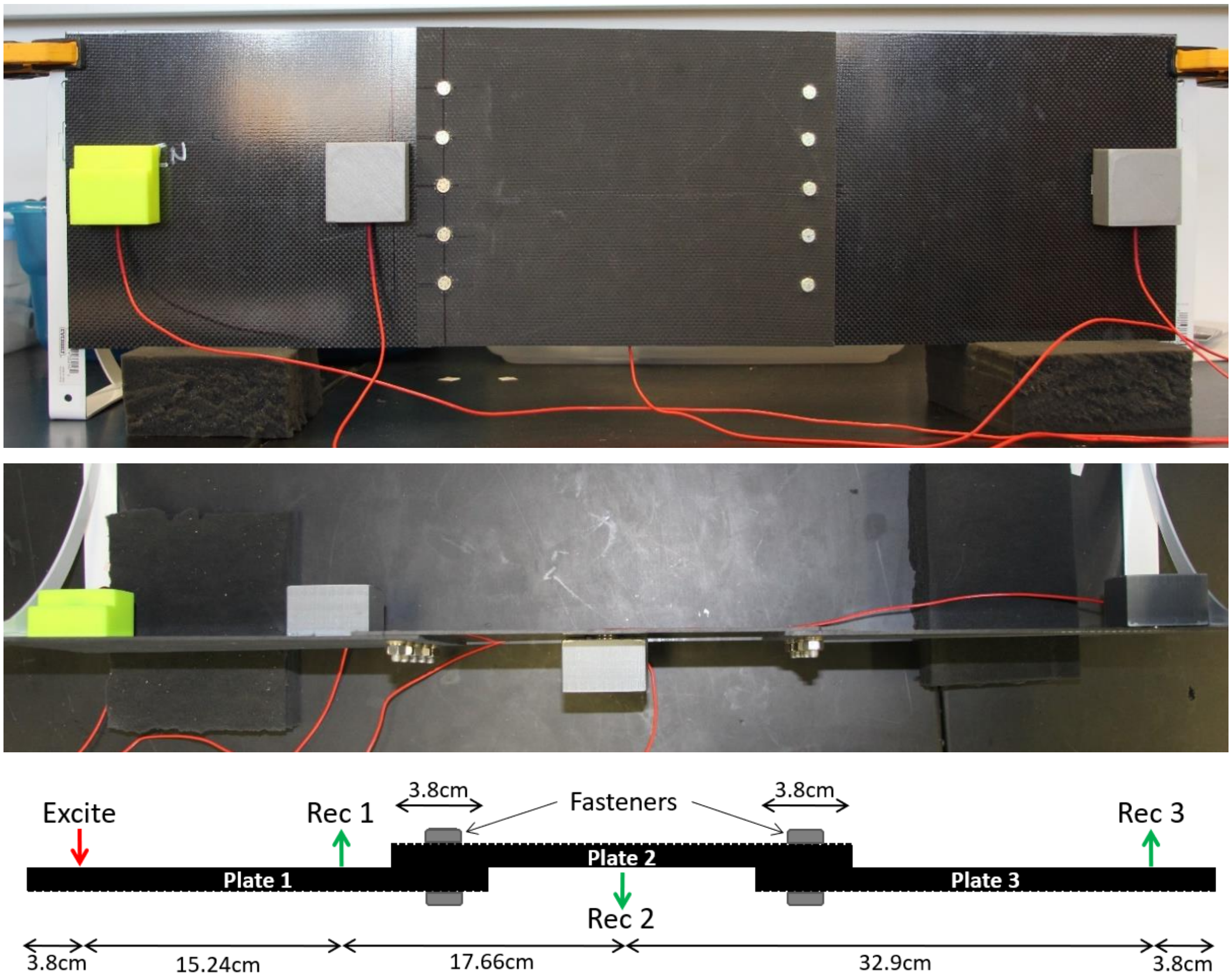

Figure 2.2.3.1.1. Bolted joint VARTM plates with R15S sensors mounted with 3D printed transducer hold-down: front view, top view, and setup schematics in descending order

UGW tests were performed in a range of bolt torque levels from 0 N·m (hand-torque) to 8 N·m at 1 N·m increment, with same bolts and nuts from the Frame02 panel (Hi-Lok protruding pins and standard nuts), in order to experimentally explore wave energy transmitting through the bolted joint plates. All ten bolts were torqued to the same level simultaneously using Dial torque wrench from CDI, and UGW tests were performed for a 50 to 450 kHz frequency range for each torque level increment. Such UGW testing was performed to select a test frequency that optimally transmits UGWs through multiple bolted joint interfaces. Bolt torque level above 8

N·m, the original level for the composite panel assembly, was not tested because excess torque compression on composite parts could cause delamination damage [29].

For excitation and acquisition in the UGW tests, Mistras R15S contact transducers were mounted onto the smooth surface of the plates with neoprene foam filled 3D printed transducer hold-downs as seen in Figure 2.2.3.1.1. Test setup was the same as previous tests with PicoScope 4824 as an oscilloscope with amplification devices to increase SNR. A 3-cycle Hanning windowed sine tone burst was excited from PicoScope 4824's built-in arbitrary waveform generator.

2.2.3.2. Bolted Joint UGW Experimental Results

UGW results from a series of bolted joint composite plates were post-processed to investigate the energy of transmitted waves through multiple joints. The first wave packet of UGW signals was gated for test sets at various frequencies and torque levels to analyze clean signals only, that are free from boundary-reflected waves. Gated first wave packet was calculated for the wave energy feature, root mean square (RMS) of the signal, and ratio of RMS of a gated waveform received at receiver 2 and 3, with respect to the RMS at receiver 1, was analyzed in plots with torque levels in domain as shown in Figure 2.2.3.2.1. The signal acquired at receiver 1 contains UGWs prior to their propagation through the bolted joints, so the ratio of energy displayed in Figure 2.2.3.2.1 provides information about the wave transmission energy loss through the series of bolted joint plate interfaces. Yang and Chang [19] described the relationship of transmitted wave energy, E^o, at the bolted joint (see Figure 2.2.3.2.2 to the contact pressure, P, as shown in Equation (2.2.3.2.1), where c is an empirical constant.

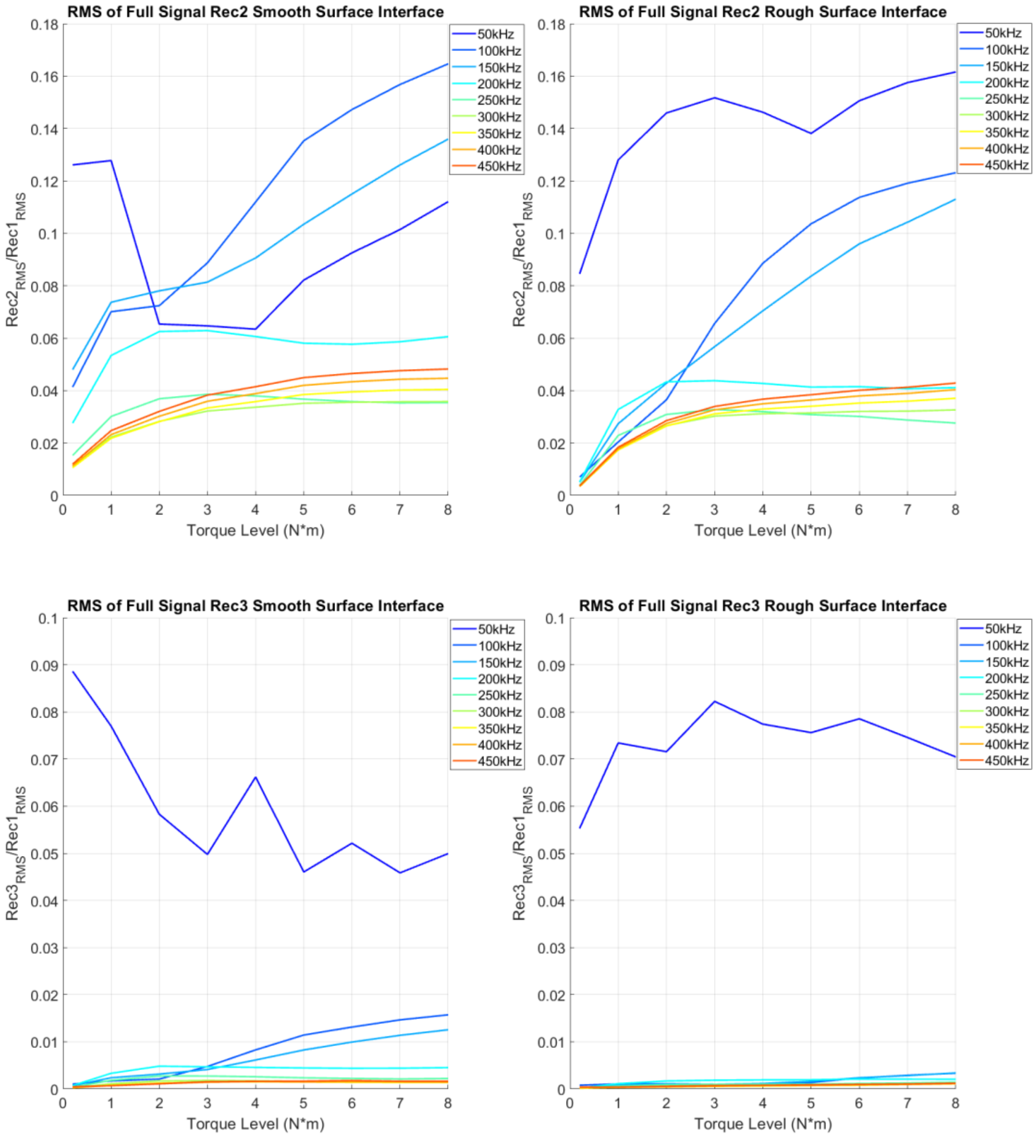

Figure 2.2.3.2.1. Energy feature, RMS, ratio results from UGW through multiple bolted joints

$$E^{o} \propto 1 - c\sqrt{(P)} \qquad (2.2.3.2.1)$$

The wave energy leaked through the bolted joint component, E^{l}, was written in Equation (2.2.3.2.2), assuming no wave energy loss occurs at the joint interface.

$$E^{l} \propto c\sqrt{(P)} \qquad (2.2.3.2.2)$$

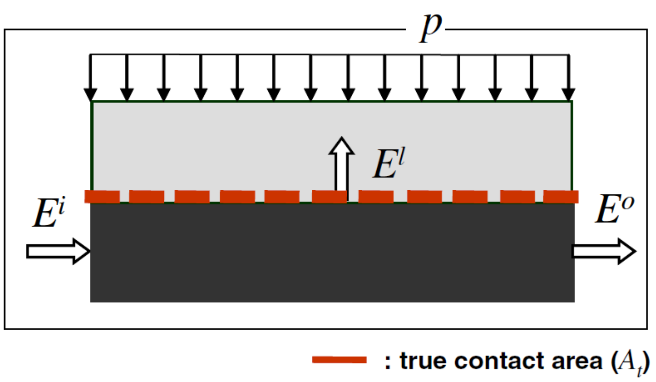

Figure 2.2.3.2.2. Energy transmission at the contact interface [11]

RMS ratio results show that the transmitted wave energy converges to Equation (2.2.3.2.2) only at frequencies above 200 kHz (see Figure 2.2.3.2.1). RMS ratios of receiver 2 and 3 results show that higher the energy that was admitted through the fastener joints, the lower the test frequency. From the investigation of the wave energy through the bolted joints, it could be noted that the test frequency controls the wave admittance rate through the bolted joints. RMS ratio results at 8 N·m torque level for various frequencies are reported in Table 2.2.3.2.1. As listed in the table, UGW energy scattering is substantially lower through rough surfaces joint than smooth surfaces joint, especially at frequencies below 200 kHz.

The UGW result of panel assembly torque level, 8 N·m, combined with half-path UGW test on Frame02 panel lead to the conclusion that 50 kHz test frequency, or even lower, is suitable for a strong wave transmission through bolted joints. However, wave behavior through bolted joints at 50 kHz is theoretically not understood. Also, the sensitivity to damage detection drops at lower test frequency as observed from preliminary UGW tests on different shear tie damage cases.

Table 2.2.3.2.1: Energy feature ratio of S0 mode UGW through bolted joints

	RMS_{Rough}		RMS_{Smooth}		RMS_{Rough}	RMS_{Smooth}
	$\left(\frac{Rec2}{Rec1}\right)$	$\left(\frac{Rec3}{Rec1}\right)$	$\left(\frac{Rec2}{Rec1}\right)$	$\left(\frac{Rec3}{Rec1}\right)$	$\left(\frac{Rec3}{Rec2}\right)$	$\left(\frac{Rec3}{Rec2}\right)$
50 kHz	0.0869	0.0353	0.0949	0.0351	40.62%	36.99%
100 kHz	0.1364	0.0042	0.1878	0.0201	3.08%	10.70%
150 kHz	0.1223	0.0037	0.1479	0.0142	3.03%	9.60%
200 kHz	0.0491	0.0024	0.0752	0.0055	4.89%	7.31%
250 kHz	0.0254	0.0020	0.0399	0.0031	7.87%	7.77%
300 kHz	0.0309	0.0017	0.0352	0.0021	5.50%	5.97%
350 kHz	0.0347	0.0015	0.0372	0.0016	4.32%	4.30%
400 kHz	0.0366	0.0013	0.0392	0.0013	3.55%	3.32%
450 kHz	0.0381	0.0012	0.0414	0.0013	3.15%	3.14%

2.3. Mini-Impactor

A mini-impactor was developed to generate a broadband frequency excitation source that is capable of delivering high energy UGWs through complex composite panels. The mini-impactor was designed to generate mechanical impulse, J, having a duration as short as possible to excite ultrasonic range frequencies based on Impulse-Momentum Theorem in Equation (2.3.1). Short duration impulse, which is directly related to the frequency response, was studied to be proportional to the hardness of the impactor tip and inversely proportional to the mass of the impactor by Halvorsen and Brown [28]. Hence, the mini-impactor was designed with a light-weight flat aluminum tip at the end of a flexible lightweight carbon/epoxy composite beam. Aluminum sheet of 0.635 mm thickness was trimmed and bonded to the composite strip as shown in Figure 2.3.1.

$$J = \int F * dt \tag{2.3.1}$$

Finite element model (FEM) simulation was used to estimate the approximate frequency range when various metal tips were impacted on an aluminum plate (see Appendix A). Then the first batch of physical mini-impactors was fabricated with 0.5 mm thick flat aluminum impactor tip (post-surface preparation) bonded onto the $[0]_8$ layup unidirectional carbon/epoxy composite strip, followed by abrasive surface preparation for proper bonding, as shown in Figure 2.3.1.a. A thin sheet of aluminum of the same thickness as the metal tip served as a shim to allow flat-wise impact: i.e., the whole surface of the impactor tip should uniformly impact the aluminum plate (see Figure 2.3.1.b and Figure 2.3.1.1). Mini-impactors with various surface area with same thickness aluminum tips were examined. The second batch of mini-impactors was fabricated using T800/3900-2 unidirectional prepreg of $[0]_4$ layup with impact tips of different thicknesses, 0.2 mm and 0.5 mm.

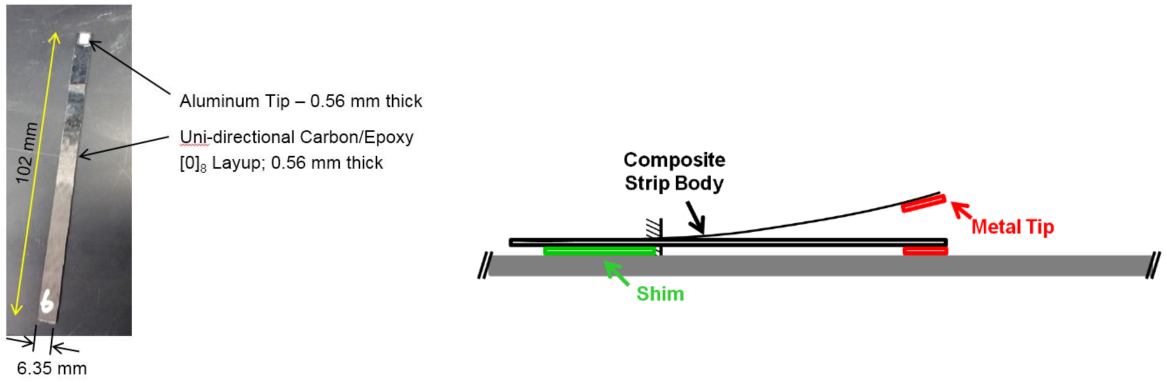

(a) (b)

Figure 2.3.1. Mini-impactor: (a) mini-impactor structure and (b) impact exertion

2.3.1. Mini-Impactor Experimental Setup

Experimental tests of the mini-impactor were performed on an aluminum plate with various receiver sensors to observe frequency responses (see Figure 2.3.1.1). The mini-impactors' responses were analyzed and compared to the 0.5 mm sharp pencil-lead break test using the contact and non-contact transducers. Impact duration and response of the mini-impactor were visually investigated using a Phantom v7.3 high-speed camera (see Figure 2.3.1.2)

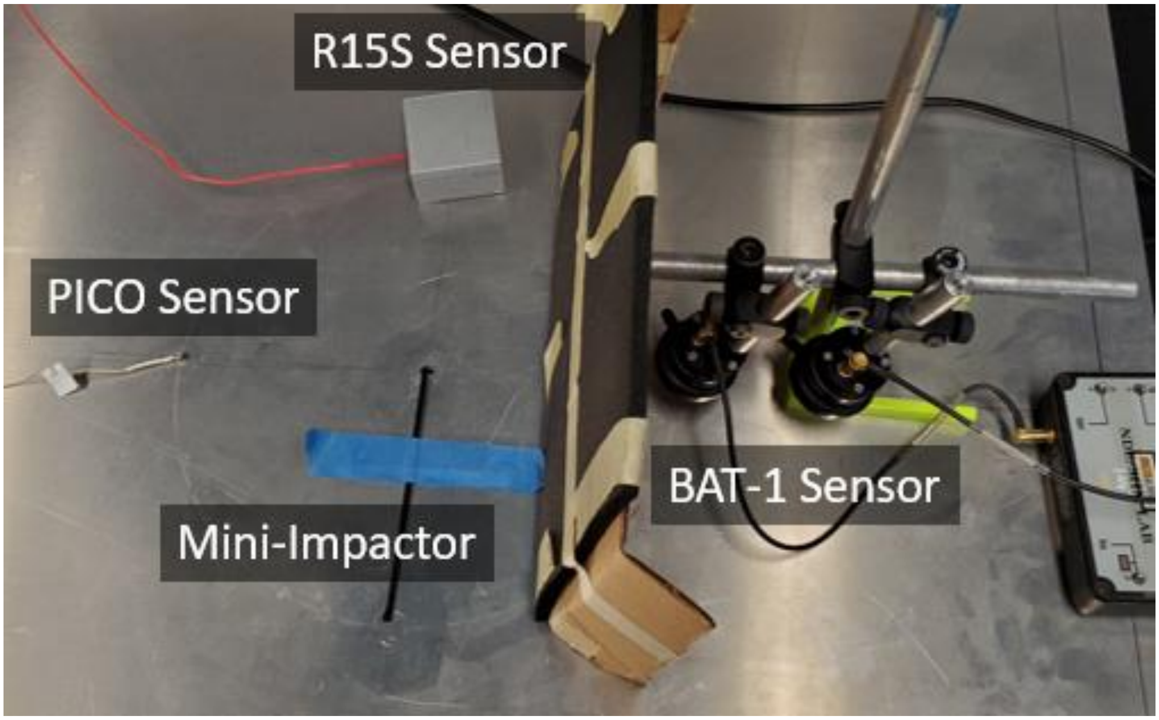

Figure 2.3.1.1. Mini-impactor test setup on an aluminum plate

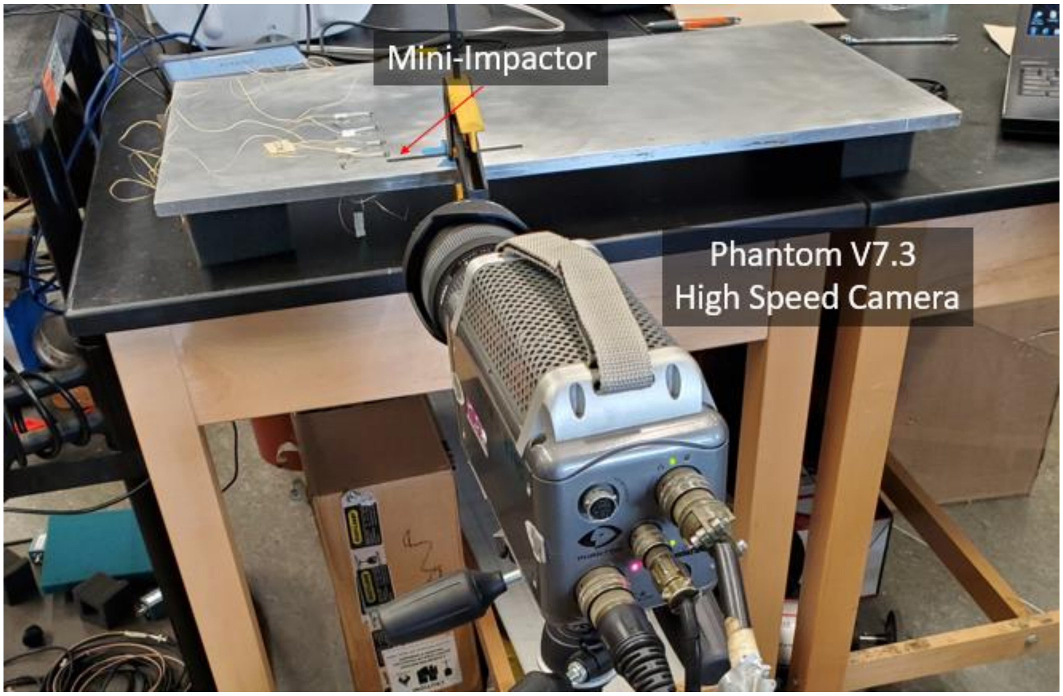

Figure 2.3.1.2. Mini-impactor test with high-speed camera

2.3.2. Mini-Impactor Experimental Results

Mini-impactors with different “target” tip areas, 1 x 1, 2 x 2 and 3 x 3 mm^2, were reported as their weight, 5.1, 15.8 and 46.0 mg, respectively, instead of their exact area. A mini-impactor with 5.1 mg tip was tested on an aluminum plate with PICO sensors at 12.7 cm distance away and the result of the first received wave packet was window gated (red signal in Figure 2.3.2.1.a) from the full signal response (blue signal in Figure 2.3.2.1.a) to analyze the excited frequency response of the mini-impactor. Frequency response from the mini-impactor with 5.1 mg impactor tip shows 42 kHz resonance frequency excitation with activated frequency response up to ~500 kHz. Figure 2.3.2.2 shows frequency response of the mini-impactors with 15.8 mg and 46.0 mg impactor tips of the same thickness as the 5.1 mg tip from the same test setup. All three mini-impactors generated frequency excitation nearly up to 500 kHz, but the mini-impactor with wider area was exciting higher resonance frequency, 58 kHz and 68 kHz for 15.8 mg and 46.0 mg tips, respectively. Also, mini-impactors with wider flat surface area were discerned to activate higher energy response for higher frequency range. It should be noted that mini-impactor response tests were conducted without the need of a preamplifier to boost the received signal in the PICO transducer.

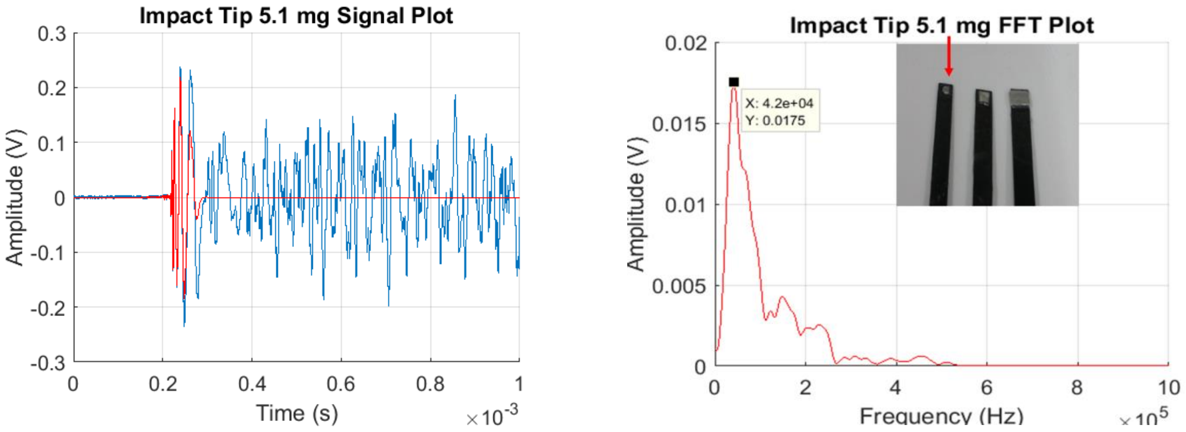

(a) (b)

Figure 2.3.2.1. Mini-impactor (a) signal and (b) frequency response of red window gated signal from 1 x 1 mm^2 impactor tip

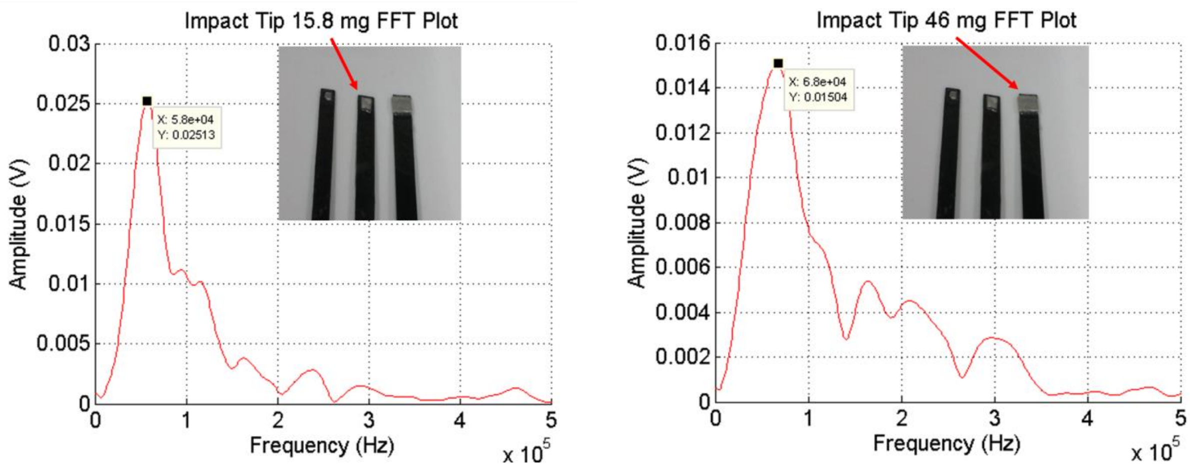

(a) (b)

Figure 2.3.2.2. Frequency responses of mini-impactors with (a) 2 x 2 mm^2 and (b) 3 x 3 mm^2 tip area

A mini-impactor of 3x3 mm^2 area (46 mg) was tested on an aluminum plate with an air-coupled transducer and was compared to the test response of 0.5 mm pencil-lead break from the same setting. The mini-impactor and pencil-lead break both generated broadband frequency excitation, but the mini-impactor exerted much higher intensity excitation (Figure 2.3.2.3.a) than the pencil-lead break excitation (Figure 2.3.2.3.b), nearly one order of magnitude higher. In turn, surrounding noise received by an air-coupled transducer appeared on the spectrogram plot in Figure 2.3.2.3.b, especially between 0.05-0.1 ms.

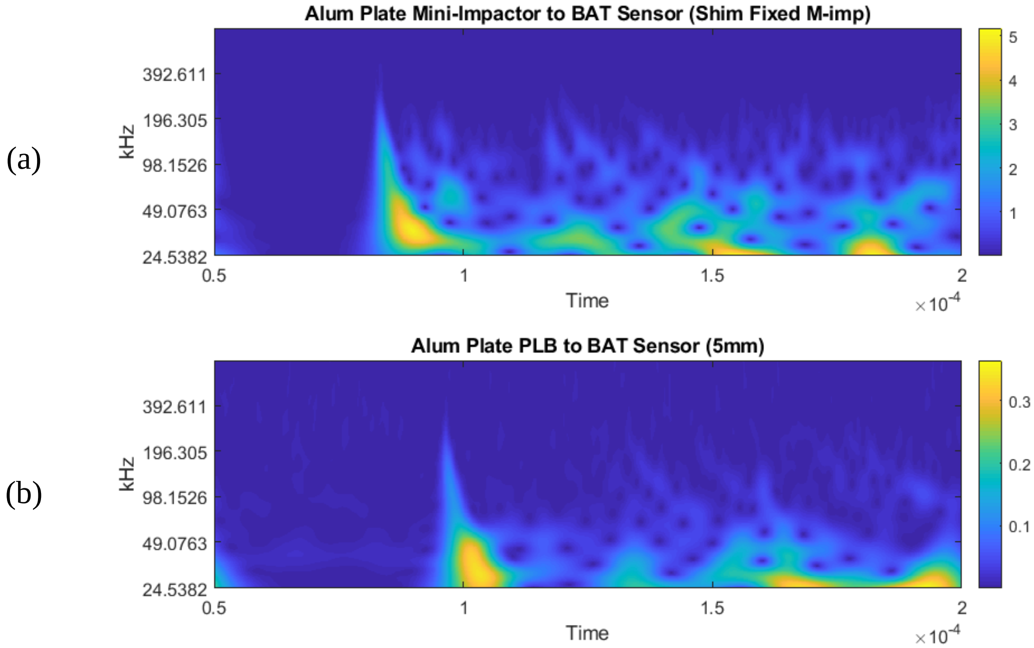

Figure 2.3.2.3. Spectrograms of (a) mini-impactor and (b) pencil-lead break responses

A second batch of mini-impactors was examined for their physical response at the time of impact using a high-speed camera. It was observed that mini-impactors with 0.2 mm thick impactor tip allowed composite beams to contact post-impact, while 0.5 mm thick impactor tip did not have the same follow-up contact with composite beams. Visually observed contact duration for both impactor tips were 11μs (0.2 mm tip) and 33μs (0.5 mm tip). Second contact from the mini-impactor was also observed 159 frames (11 μs/frame at 128 x 128 pixel resolution) after first contact for the mini-impactor with 0.2 mm tip and 337 frames (9 μs/frame at 128 x 80 pixel resolution) for the mini-impactor with 0.5 mm tip (see Figure 2.3.2.4). In other words, second contact of the mini-impactors with 0.2 and 0.5 mm tip occurred 1.75 and 3.03 ms after the first contact, respectively. Mini-impacts' frequency response plot is shown in Figure 2.3.2.5.

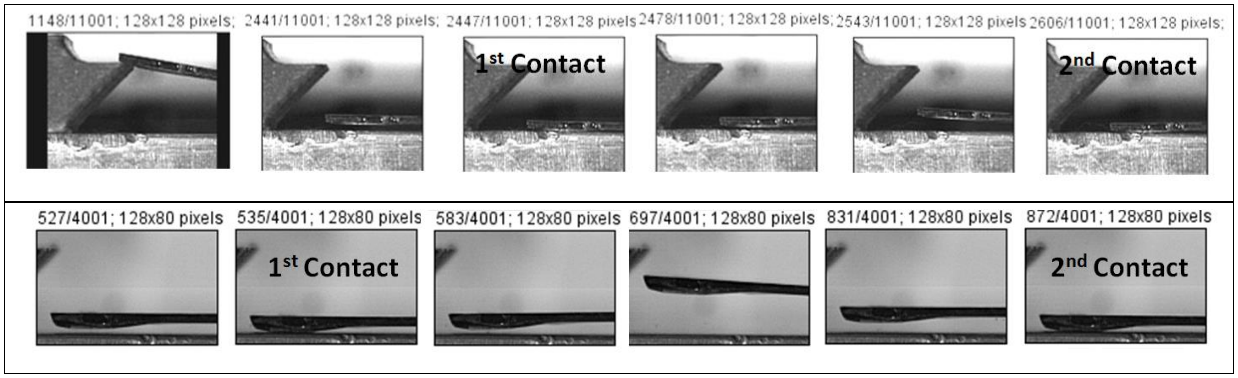

Figure 2.3.2.4. High-speed motion capture of mini-impactor response

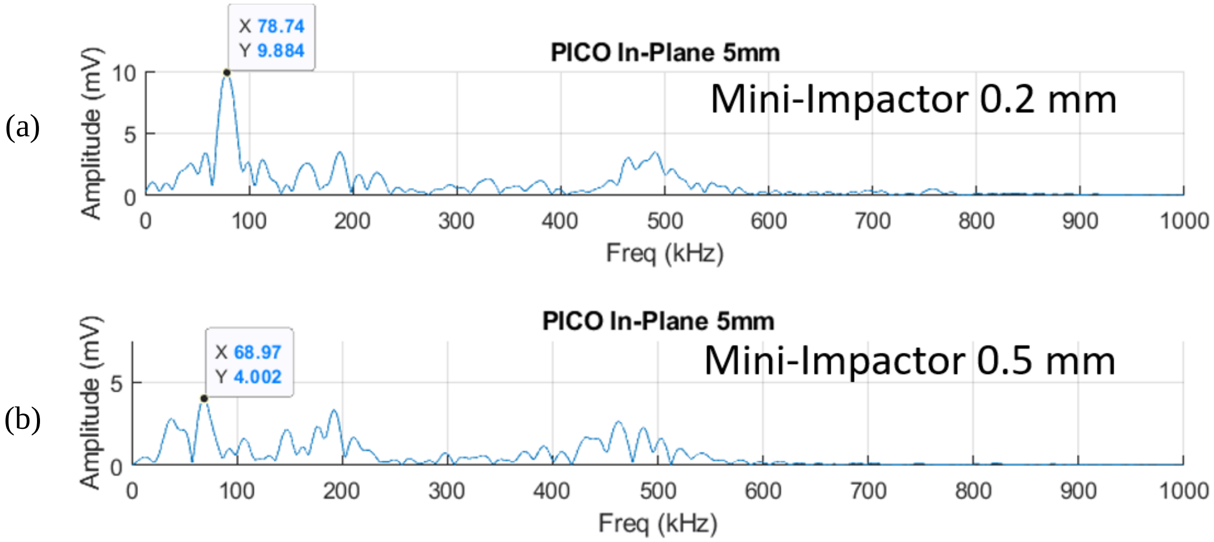

Figure 2.3.2.5. Frequency response of mini-impactor with (a) 0.25 mm and (b) 0.64 mm impactor tip thicknesses

2.4. Contact-Based Frame02 Panel Internal Structure Scan

2.4.1. Contact-Based Frame02 Panel Internal Structure Scan Experimental Setup

The mini-impactor was used as a broadband excitation source for the UGW-based internal damage detection tests after extensive analysis on the frequency response of the mini-impactor. R15S transducers served as a receiver for Frame02 panel damage detection, but amplification devices were removed from the system due to high intensity excitation produced by the mini-impactor (no amplification needed). The mini-impactor was chosen as an excitation source instead of actuator transducer because it generates broadband frequency excitation that delivers UGWs through complex waveguides on the Frame02 panel at frequencies each waveguide favors. Mini-impactor with R15S transducer combo delivered strong UGWs through the skin and frame paths at 150 kHz and 40 kHz frequencies (results presented in the following section).

The mini-impactor was taped down onto the skin with the shim, same thickness as the impactor tip, at the center of the shear tie joint, and a R15S receiver transducer was mounted onto the center of the shear tie joint skin surface, adjacent to the excitation location with a 3D printed hold-down (see Figure 2.4.1.1). Internal structure scanning system was composed of a PicoScope 4824 with a laptop for data acquisition, the mini-impactor for excitation, and a R15S for receiver transducer. It is worth noting that this system, since it doesn't need amplifiers, weighs less than 2.5 kg.

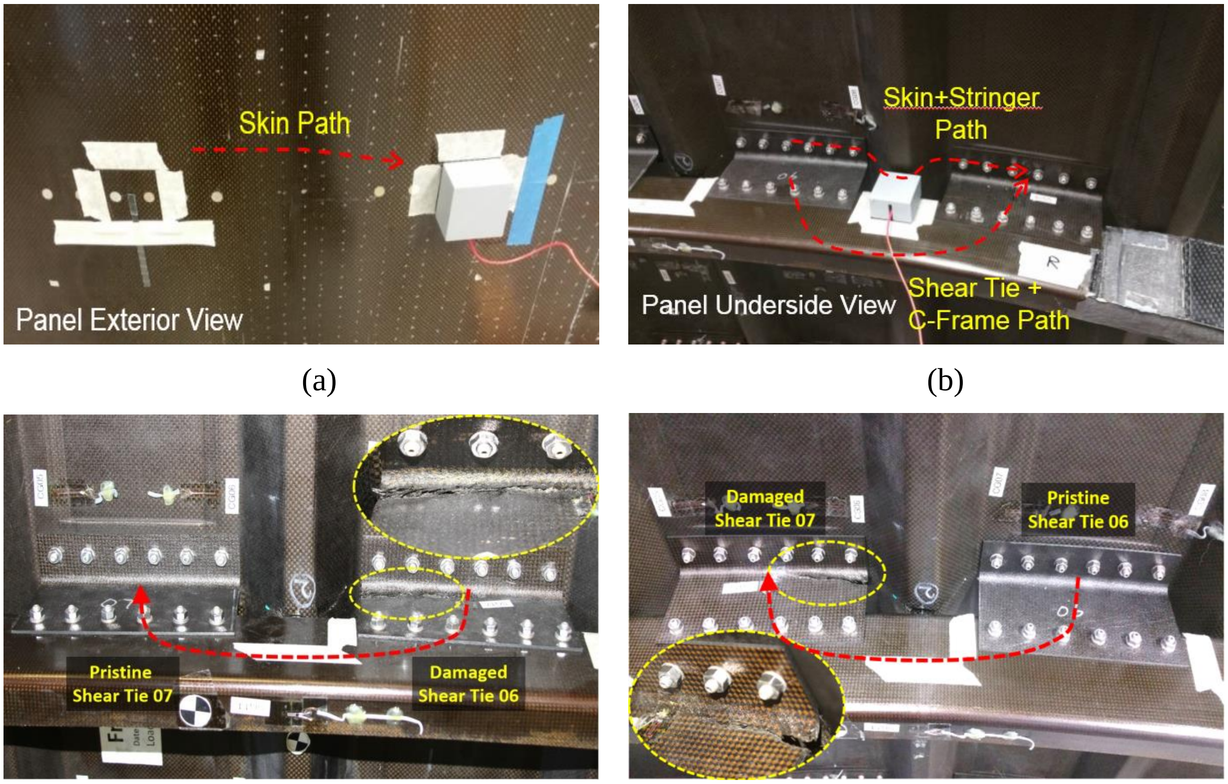

(a) (b)

(c) (d)

Figure 2.4.1.1. Frame02 panel UGW internal damage detection setup: (a) test setup on the external skin-side with (b) pristine shear ties, (c) partially cracked shear tie at the inlet and (d) outlet of the internal frame path

Prior to UGW internal structure damage assessment, UGW tests on full Frame panel (Figure 2.2.1.5.a) and C-frame disassembled Frame panel (Figure 2.2.1.5.b) were compared to confirm that internal wave transmission occurs at low frequency generated from the mini-impactor. Finally, full Frame panel tests were executed with pristine and damaged shear ties to interrogate UGW sensitivity to the presence of damage in the frame path.

2.4.2. Contact-Based Frame02 Panel Internal Structure Scan Experimental Results

Based on the preliminary UGW results of the Frame02 panel, 50 kHz test frequency was focused on to inspect the internal structure of the Frame02 panel. A UGW test was executed with a mini-impactor and an R15S receiver on the outer skin surface (Figure 2.4.1.1.a) on Frame02 panel with (Figure 2.4.1.1b) and without a C-frame (Figure 2.2.1.5.b), and the test results are presented in spectrograms, after applying Continuous Wavelet Transform (CWT) (Figure 2.4.2.1). The spectrogram shows UGW energy concentrated mostly near the 40 kHz and 150 kHz for the test performed on a fully assembled panel (Figure 2.4.2.1.a).. When the C-frame was disassembled from the panel (Figure 2.4.2.1.b)., the dominant UGW energy in the 40 kHz range disappeared. The test validates that received UGWs at around 40 kHz are mostly associated with waves that are internally transmitted. Additionally, the mini-impactor's broadband frequency excitation delivered robust 150 kHz and 40 kHz UGW content through skin and frame path, respectively, compared to other frequencies to R15S receiver transducer.

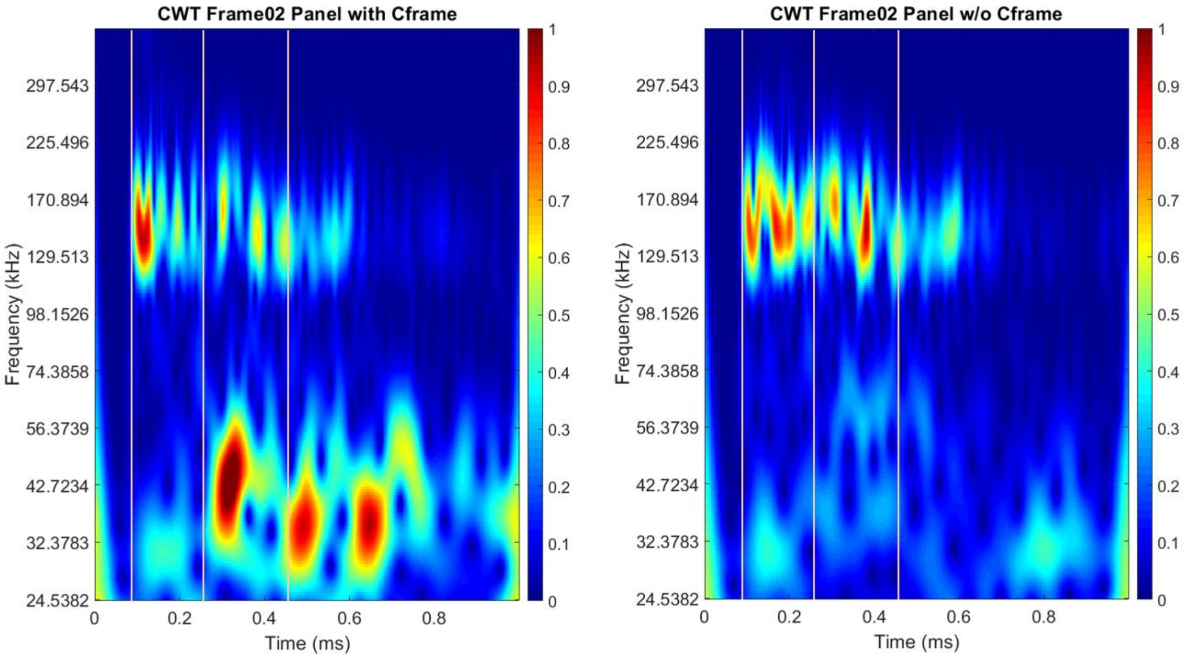

(a) (b)

Figure 2.4.2.1. Mini-Impactor and R15S receiver UGW test results from external skin-side: internal frame path (a) continuous and (b) discontinuous

UGW test spectrogram results on the Frame02 panel, comparing pristine shear ties (Figure 2.4.1.1.b) versus one partially cracked shear tie (Figure 2.4.1.1.c or d), show significantly reduced wave energy at around 30 kHz when damaged shear tie was present in the frame path (Figure 2.4.2.2 and Figure 2.4.2.3). Empirically recognized first flexural wave packet of internally transmitted UGWs (0.35-0.55 ms) at low frequency shows discernable energy drop in the frequency response plots in Figure 2.4.2.2 and Figure 2.4.2.3, which enables binary state judgement of damage presence in the internal structure. Despite the severity or location of the partially cracked shear ties, energy scattering due to a partially cracked shear tie shows significant wave energy drop whether shear tie damage was near the inlet or the outlet of the wave path.

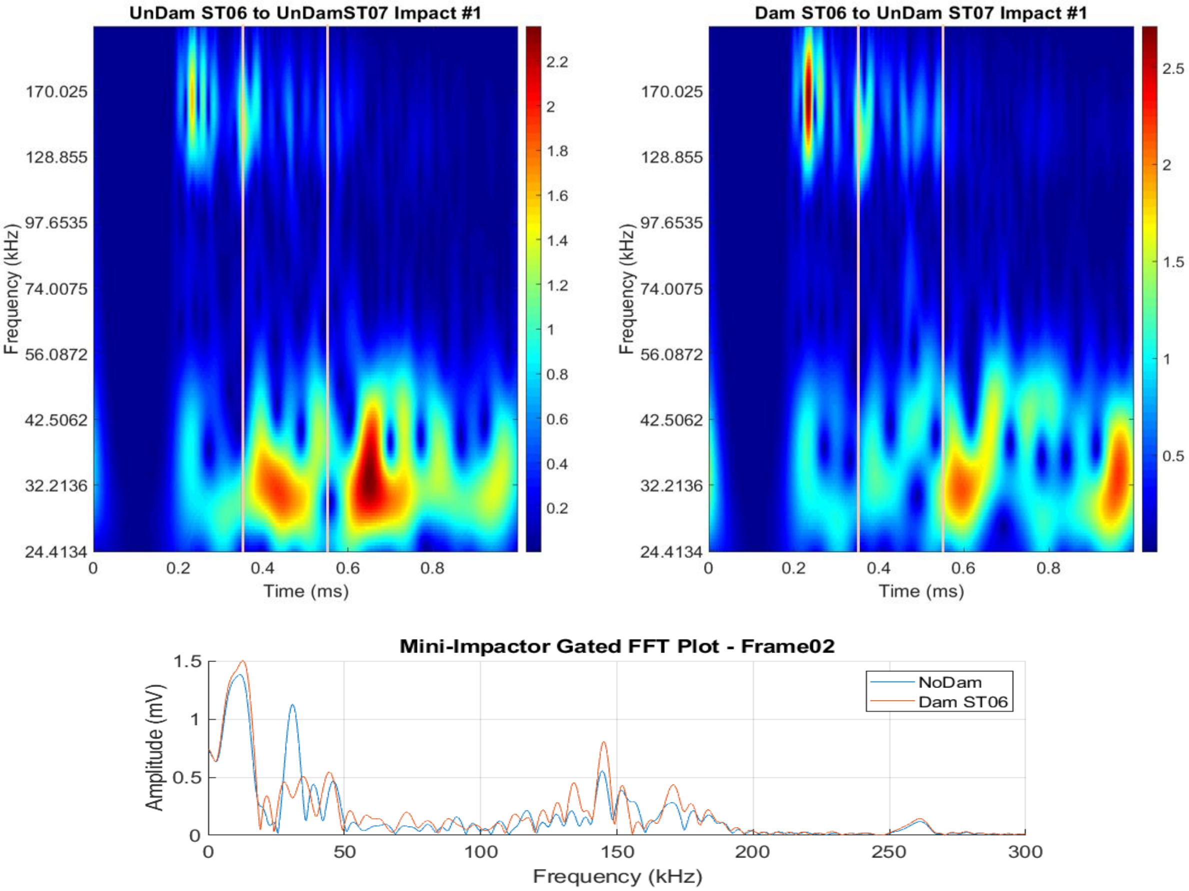

Figure 2.4.2.2. UGW spectrogram results and frequency responses of gated signal in orange vertical line boundaries with pristine vs damaged shear tie 06

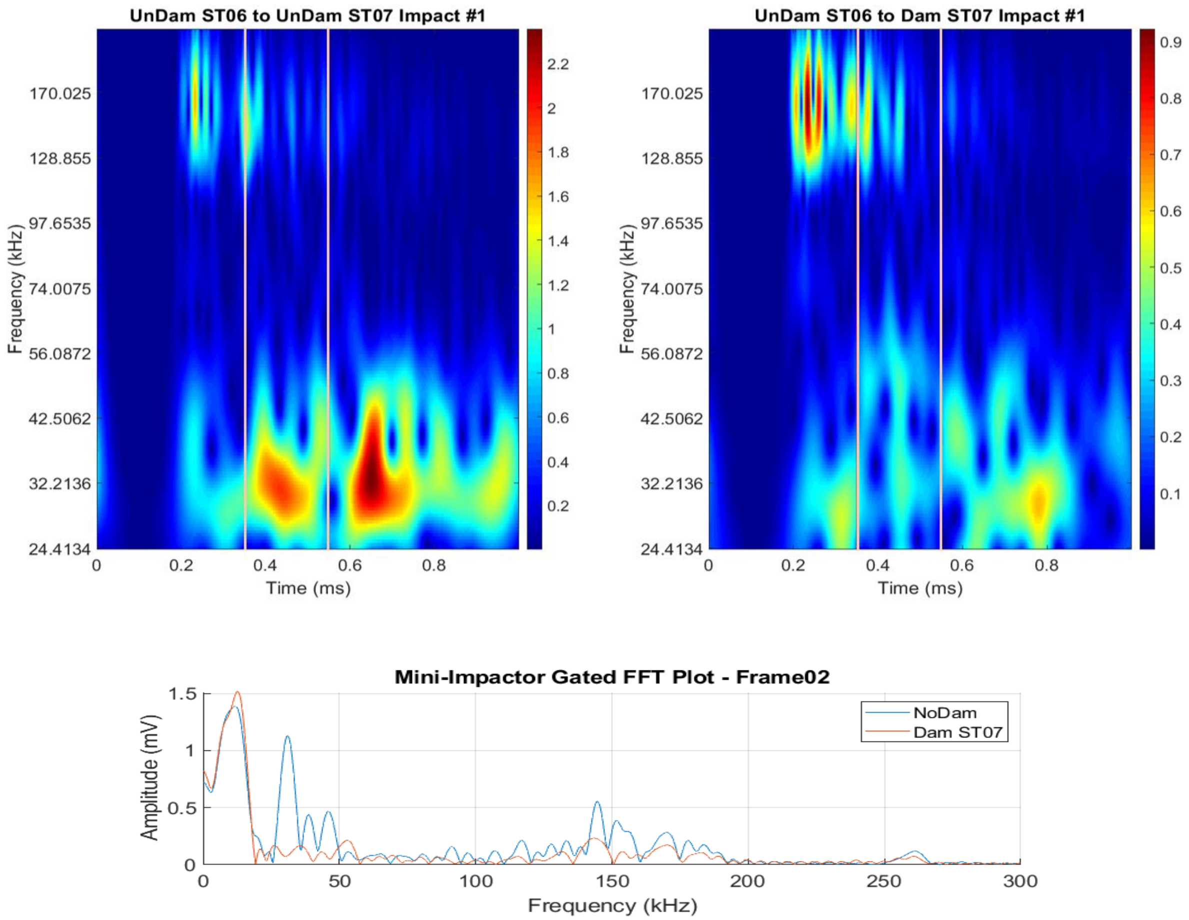

Figure 2.4.2.3. UGW spectrogram results and frequency responses of gated signal in orange vertical line boundaries with pristine vs damaged shear tie 07

2.5. Non-Contact-Based Cart Scan

Contact-based stringer scanning method [27] required great effort in scanning along the stringer -- couplants had to be applied before mounting the transducers per scan point. A non-contact-based rapid cart scan system was developed to achieve better performance than the contact-based stringer scanning method to scan along the co-cured stringer from the external skin-side only, as it scanned along a meter-long stringer within a few seconds and reduced errors occurring from faulty coupling. As such, contact-based stringer scan method will be omitted, and only non-contact-based stringer scanning method is discussed herein.

This portion of the research was co-developed in collaboration with another PhD student, Margherita Capriotti [27]. This project was supported by the FAA, and together we developed and designed the data acquisition system to analyze the collected UGW data. Capriotti developed the multivariate outlier analysis computing code to successfully detect and locate damage along the stringer.

2.5.1. Non-Contact-Based Cart Scan Experimental Setup

Air-coupled transducers were assembled onto a wheeled cart to scan along the stringer rapidly while transmitting and receiving guided waves across the skin-stringer cross-section, as seen in Figure 2.5.1.1 A cylindrically focused air-coupled transmitter (NCG200-S50-C76-EP-X) and an unfocused air-coupled receiver (NCG200-S19) from Ultran were utilized on the cart system and transducers were oriented 14 degrees from normal of the skin surface towards one another to focus flexural modes excitation and reception according to Snell's law (Equation (2.5.1.1)). Transducer orientation angle, θ_{air}, was calculated from the experimentally evaluated flexural wave mode velocity, v_f, that is about 1400 m/s at 170 kHz test frequency using Equation (2.5.1.1). Also, transducers were fixed at specific distances away from the skin surface as suggested by the manufacturer: cylindrically focused transmitter at 7.6 cm and unfocused receiver at 3.18 cm away from the composite panel.

$$\theta_{air} = sin^{-1}\left(\frac{v_{air}}{v_f}\sin\theta_f\right) \tag{2.5.1.1}$$

Stringer03 panel was UGW tested with this moving cart system from the exterior skin-side to scan for damage modes presented in Figure 2.1.3. A foam block was placed between transducers as a barrier for air-transmitted waves to only allow UGWs propagated through the composite panel to be received. R21-P wheeled encoder was assembled onto the cart system to trigger a five-cycle Hanning window gated tone burst excitation as a pulse was generated from the encoder per scan to record the location. Single stringer of 80 cm span was scanned in 8 seconds with 1 cm resolution. Linear amplifier and preamplifier were used increase the signal to noise ratio.

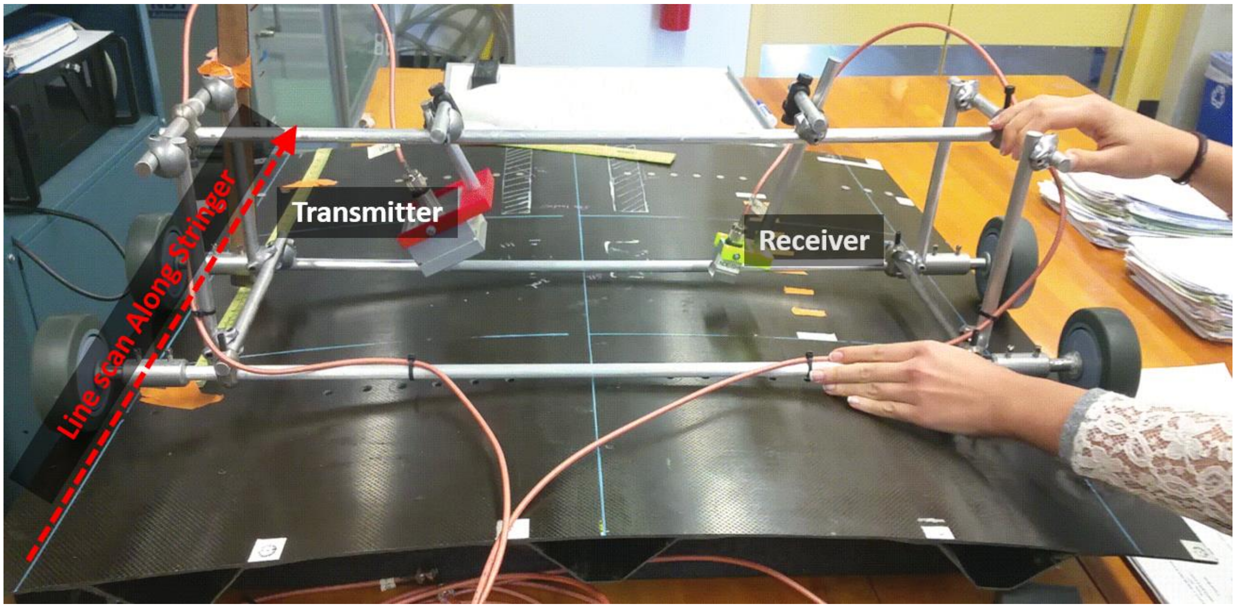

Figure 2.5.1.1. Non-contact-based scanning experimental test setup

2.5.2. Non-Contact-Based Cart Scan Experimental Results

UGW cart scan on Stringer03 panel of 1 m long stringer was completed in 8 seconds and the raw signals of the three scans were averaged as shown in Figure 2.5.2.1. Skin and heel of the stringer were cracked at the impact location, and the UGW result at the impact location compared to the pristine location shows that the TOF and amplitude of the wave packet were delayed and attenuated due to the presence of the damage. And the stringer disbond damage also caused a delay in TOF, but amplitude of the first wave packet was increased.

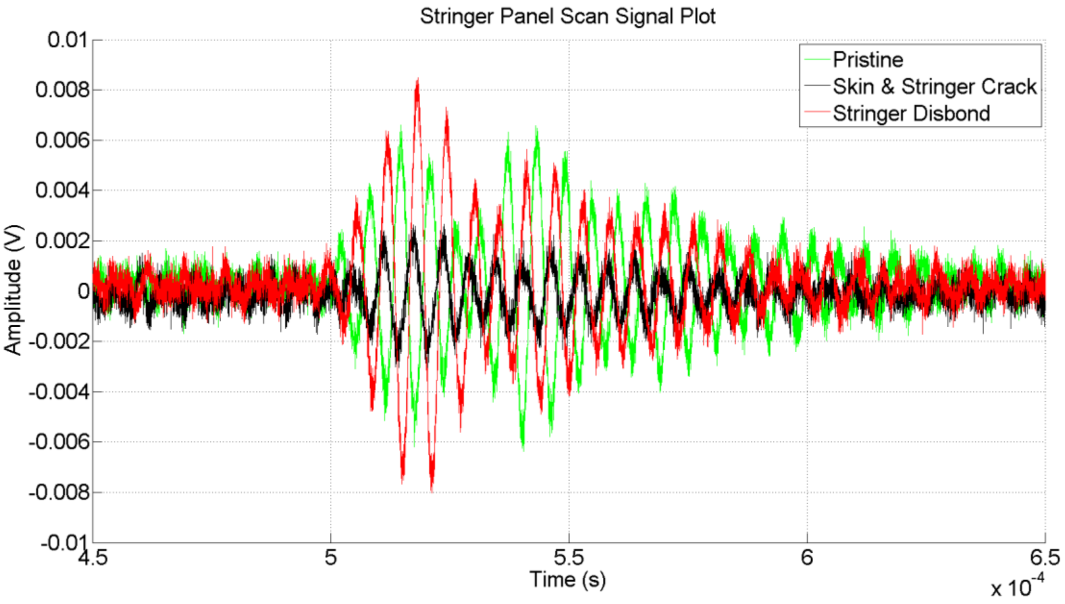

Figure 2.5.2.1. Non-contact cart scan averaged raw signals

The waveform from the cart scan result was segmented based on TOF for specific wave modes from skin and stringer wave paths (see Figure 2.5.2.2) to distinguish the damage information at higher precision. Amplitude feature, peak values of frequency response, did not clearly detect damage from the scan because amplitude value change was small and inconsistent (amplified and reduced for disbond and cracked damage modes, respectively). However, damage index computed along the stringer scan from multiple features with an average baseline vector clearly identified the damage location (see Figure 2.5.2.3).

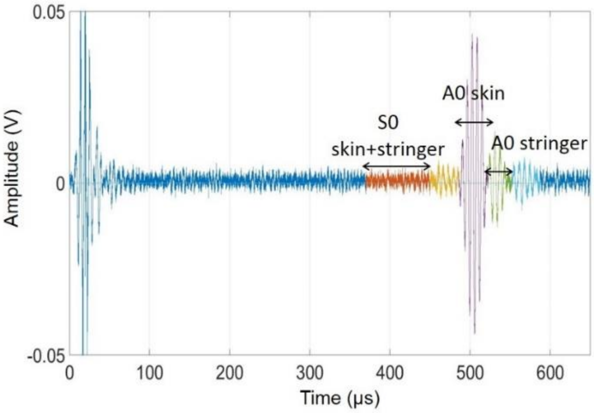

Figure 2.5.2.2. Typical signal from non-contact technique with gated wave packets [27]

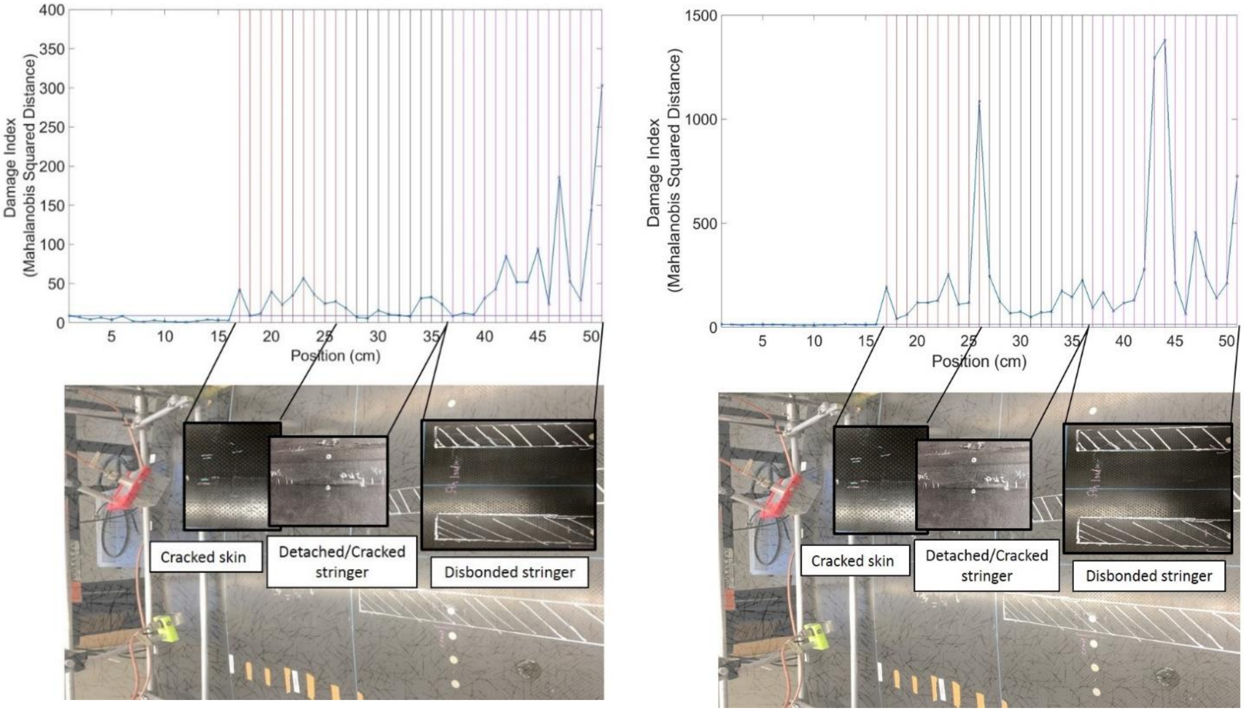

(a)

(b)

Figure 2.5.2.3. Non-contact defect-detection technique DI: (a) skin-only modes and (b) skin and stringer modes [27]

2.6. Discussion

The results of the tests from Frame02 panel deduces that the hypothesized differential approach is not feasible because the C-frame was recognized to transmit asymmetric UGWs throughout its structure caused by ply splice overlap joints inherent to this structure's manufacturing. However, an advanced manufacturing method, automated fiber placement, should allow manufacturing in continuous ply without splice overlap, which will allow differential comparison method from achieving symmetrical wave propagation.

Regardless of the disagreement of the wave transmission as hypothesized, UGW tests were performed through a single path to study the feasibility of the UGW-based damage detection in the internal structure damage. Partially cracked shear tie UGW damage detection test in full-path showed more than half of the energy loss from the frequency response at 30 kHz (Figure 2.4.2.2 and Figure 2.4.2.3), which is a much higher wave energy scattering obtained from the UGW tests from different shear tie damage cases (Figure 2.2.2.6). UGW-based shear tie damage detection using the mini-impactor increased in sensitivity because the partial cracked shear tie damage is located exactly in the internal wave path, and UGW results from discrete shear ties with damage were received from the center receiver from three receivers in Figure 2.2.1.4.b. Such amplitude-based damage detection has limited capability to identify damage characteristics, such as damage type, severity and location, from the exterior skin-side test results. UGW-based C-frame damage detection through full-frame path wasn't further executed because internal damage was studied to be first generated on shear ties. Thus, shear tie damage detection should be prioritized for the bolted joint internal structure damage detection.

UGWs propagated through the skin path and the frame path dominantly at 150 kHz and 40 kHz frequency, respectively, for the test setup with a mini-impactor and an R15S transducer. Such broadband UGW frequency dominance through the wave path was achieved from the mini-impactor paired with the R15S transducer, which has lateral vibration mode resonance near 150 kHz. Dominance test frequency through each wave path could be changed if the test structure changes. However, the UGW test system can be modified to find another frequency combo to distinguish waves transmitted through different wave paths. Excitation resonance frequency of the mini-impactor can be ramped up with different material impact tip (e.g., steel) and wider impact surface area. Impact intensity could also be ramped up by increasing the flexural rigidity of the composite beam by introducing angled layup in the plies.

Stringer damage modes on Stringer03 panel were investigated and detected using a scanning cart with air-coupled transducers operating at 170 kHz. Although rapid cart scan provided acceptable results, adequate number of signal averaging was necessarily performed to reduced noise level of received signals from the cart scan which affects the speed at which the cart scanning can be achieved.

2.7. Conclusions

UGW-based damage detection feasibility tests were executed on blunt impact tested complex (i.e., multi-component assemblies) composite panels with major internal damage modes that include fiber damage and cracks. UGW propagation through a complex composite panel was first scrutinized from discrete elements to assembled components: C-frame, shear tie, and co-cured skin-stringer shell were initially investigated for their UGW propagation and complex bolted joint components were investigated for UGW transmission through multiple waveguides on full bolted joint assembled sub-component level composite structure. UGW transmission through full skin and frame wave path (Figure 2.4.1.1.a and Figure 2.4.1.1.b, respectively) was perceived to discretely propagate at 150 kHz and 40 kHz in respect to each wave path from the mini-impactor and R15S test method. UGW propagation at different frequencies through in-plane skin path and out-of-plane frame path from the mini-impactor excitation in various experiments was combined together prior to damage detection tests. 42 kHz resonance frequency excitation UGW from a mini-impactor propagates substantially through frame path and attenuates moderately through a series of bolted joints, and 150 kHz UGW from a mini-impactor that propagates through the skin path are notably significant due to the lateral mode resonance of the R15S receiver transducer.

UGW experiments for damage detection of internal structural components of complex composite panel were accomplished to detect damage on shear ties from tests performed only on the external skin-side. Major damage modes on internal composite components were generated followed by shear tie damage. Hence, damage detection of bolted joint internal structure is certainly possible with comparable baseline dataset, unless the structure has its own comparable symmetric UGW wave path to apply differential technique to compare results for damage analysis.

Advanced non-contact-based cart scan system was collaboratively [27] developed to scan for damage on composite stringer from the panel using narrowband air-coupled transducers of 170 kHz center frequency. The cart scan system is capable of scanning a meter-long stringer in 8 seconds with scan position recorded from a wheeled encoder assembled onto the cart. A powerful amplifier device and an adequate signal averaging were required in order to collect UGWs with high SNR because of high attenuation in air-transmitted waves. A hybrid scanning system with a mini-impactor and a non-contact transducer were developed – a system that serves a better purpose in terms of portability -- and it will be discussed in the following chapter.

Acknowledgements

Chapter 2 work was a collaborative work with Margherita Capriotti under the co-support from the FAA. Research work presented in chapter 2 was completed mostly together with Margherita and her advanced processing of complex data helped with the understanding of the subject in greater depth.

Chapter 2 contains publication material as it may appear in "Non-Destructive Inspection of Impact Damage in Composite Aircraft Panels by Ultrasonic Guided Waves and Statistical Processing." Capriotti, Margherita; Kim, Hyungsuk E.; Lanza di Scalea, Francesco; Kim, Hyonny. Materials, 2017. The dissertation author was the primary investigator and author of this paper.

Chapter 2 also contains material currently being prepared for submission for publication. "Ultrasonic Guided Wave Testing for Damage Detection on Bolted Joint Internal Components of Composite Structures." Kim, Hyungsuk E.; Kim, Hyonny; Capriotti, Margherita. The dissertation author was the primary investigator and author of this material.

Chapter 2 also contains material currently being prepared for submission for publication. "Non-Destructive Evaluation Methods for Detecting Major Damage in Internal Composite Structural Components." Capriotti, Margherita; Kim, Hyungsuk E.; Lanza di Scalea, Francesco; Kim, Hyonny. The dissertation author was the primary investigator and author of this material.

3. UGW-Based Stringer Panel Damage Detection and Characterization

3.1. Panel Overview

Two large (1 x 1.3 m) five-stringer stiffened composite panels were manufactured for study of impact damage on co-cured composite stringers. Impacts were conducted on the cap and the flange of the stringers (see Figure 3.1.1) on Flat Stringer Panel 1 (FSP1) and Flat Stringer Panel 2 (FSP2), respectively. FSPs were manufactured from Toray T800S/3900-2B unidirectional tape prepreg with $[45/-45/0/45/90/-45/0/90]_s$ layup for both skin and stringer with an additional 90° ply between skin and stringer flange; 16 plies thick for both skin and stringer, and 33 plies thick for skin-to-stringer co-cured flange. Dimension of the panels were 1 x 1.3 m, and the omega stringer stiffeners were 260 mm apart from each other, as shown in Figure 3.1.2.

UGW tests were executed on whole panels (i.e., as shown in Figure 3.1.2), pre- and post-impacts, to eliminate boundary reflected waves interfering with important signal information if panels were trimmed and examined as single-stringer element specimens. UGW test results were directly compared to pulse-echo Ultrasonic Testing (UT) and X-ray Computed Tomography (CT), to validate UGW tests' potential to interpret damage status comparable to the conventional methods. Panels were trimmed into single-stringer elements after all NDE investigations, and finally Compression-After-Impact (CAI) tested to evaluate damage tolerance of the stringer composite panels.

The objectives of the UGW experiments on FSPs were to explore not only the detection of blunt impact damage on the stringers, but to examine UGW test capability to estimate blunt impact damage modes, location, severity, and relationship to residual strength.

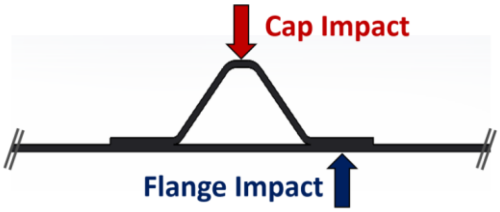

Figure 3.1.1. Impact locations on omega stringer: cap impact (red) and flange impact (navy)

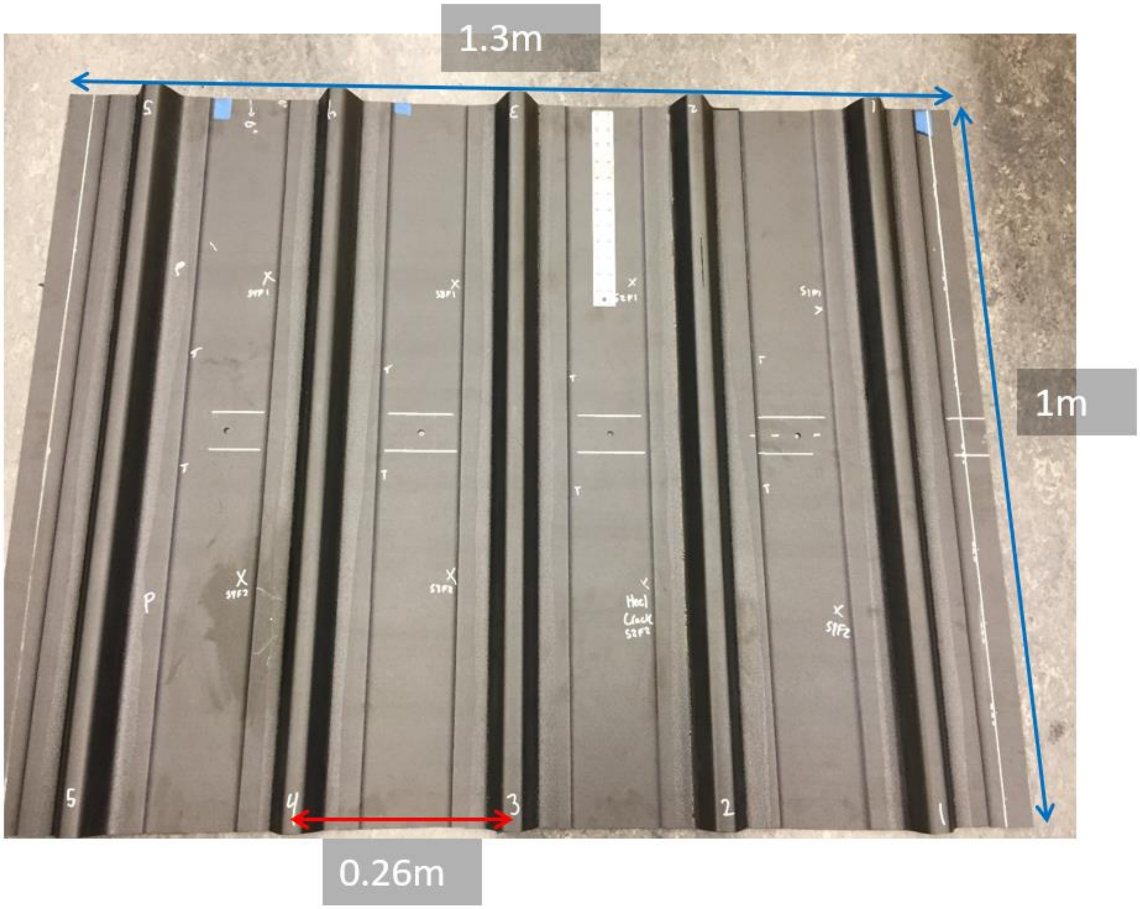

Figure 3.1.2. FSP2 with drilled holes at center of the panel for the pendulum impactor fixture

3.2. Experimental Summary

3.2.1. Impact and CAI Strength Tests

FSP1 was blunt impacted on the caps of the stringers at “target” impact levels of 30, 50, and 70 J at the center of 254 mm span distance between fixed inner ends for each designated regions as shown in Figure 3.2.1.1.a. Similarly, FSP2 was blunt impacted on stringers’ flanges at the center of 457 mm span distance of fixture inner ends (see Figure 3.2.1.1.b). Impacts on the stringer flange were performed from external skin-side at “target” impact levels of 70 and 90 J. Total of 12 impacts and 4 impacts were executed on stringer cap of the 12 regions on FSP1 and on stringer flange of the 4 regions on FSP2, respectively.

Blunt impacts were conducted on the pendulum impactor with a hemispherical metal impactor tip, 50.8 mm in diameter, with stack of masses added to the impactor (Figure 3.2.1.2). Dytran 1060V5 force sensor assembled on the impactor was used to acquire force response. A whole panel was fixed onto the pendulum impact fixture with the clamping-type aluminum bracket fixture on inner and outer skin surfaces [30]. Angular position, α, of the impactor (Equation (3.2.1.1)) was controlled and measured with an absolute encoder to estimate the height required for the target impact levels ($\alpha = 0$ at rest of the pivoting bar, vertical position). Impact levels were calculated from potential energy Equation (3.2.1.2) with effective mass of the impactor, m_{imp}, and length of the pivoting bar, L_B. True impact energies were calculated from the kinetic energy Equation (3.2.1.3) based on the velocity of the impactor, v_{in}, measured using the laser sensor photogate just before the impact. Details about the impact are summarized in Table 3.2.1.1.

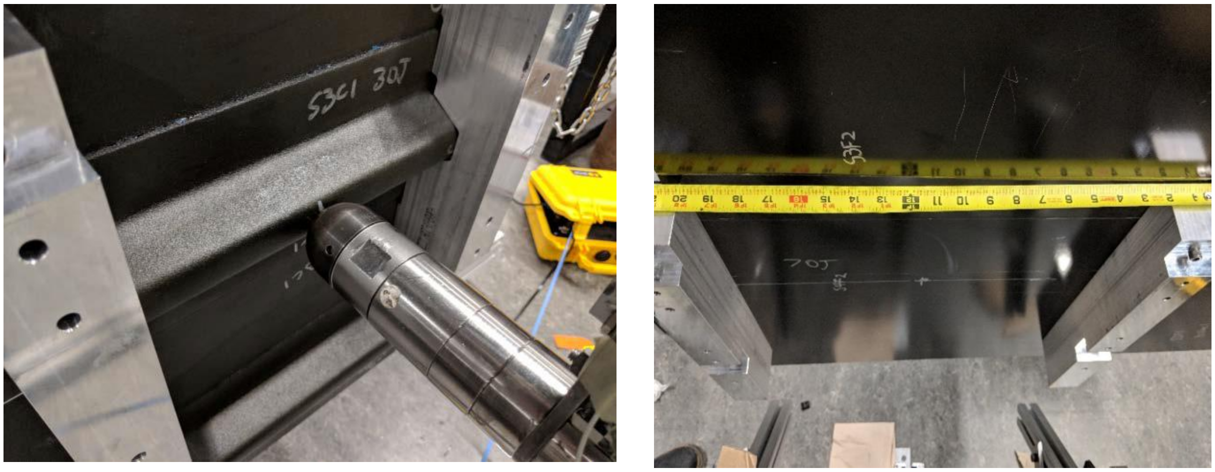

(a) (b)

Figure 3.2.1.1. FSPs fixed onto the pendulum impactor for (a) cap and (b) flange impact

Figure 3.2.1.2. Pendulum impactor setting for the cap impact at region S3C1 for 30 J target impact

$$\alpha = \arccos\left(1 - \frac{h}{L_B}\right) \tag{3.2.1.1}$$

$$PE = m_{imp} g h \tag{3.2.1.2}$$

$$KE = \frac{1}{2} m_{imp} {v_{in}}^2 \tag{3.2.1.3}$$

Post-impacted panels were first scanned with the UGW system, and then cut into single-stringer elements in 162 x 292 mm and 260 x 495 mm (across x along the stringer) dimensions for the cap and flange impacted regions, respectively. Single-stringer elements were potted at both ends of the stringer using EpoxAcast 655, aluminum powder infused epoxy, for the Compression-After-Impact (CAI) test (Figure 3.2.1.3). Compression tests were performed at NASA Langley [30] and compression failure load results are listed in Table 3.2.1.1.

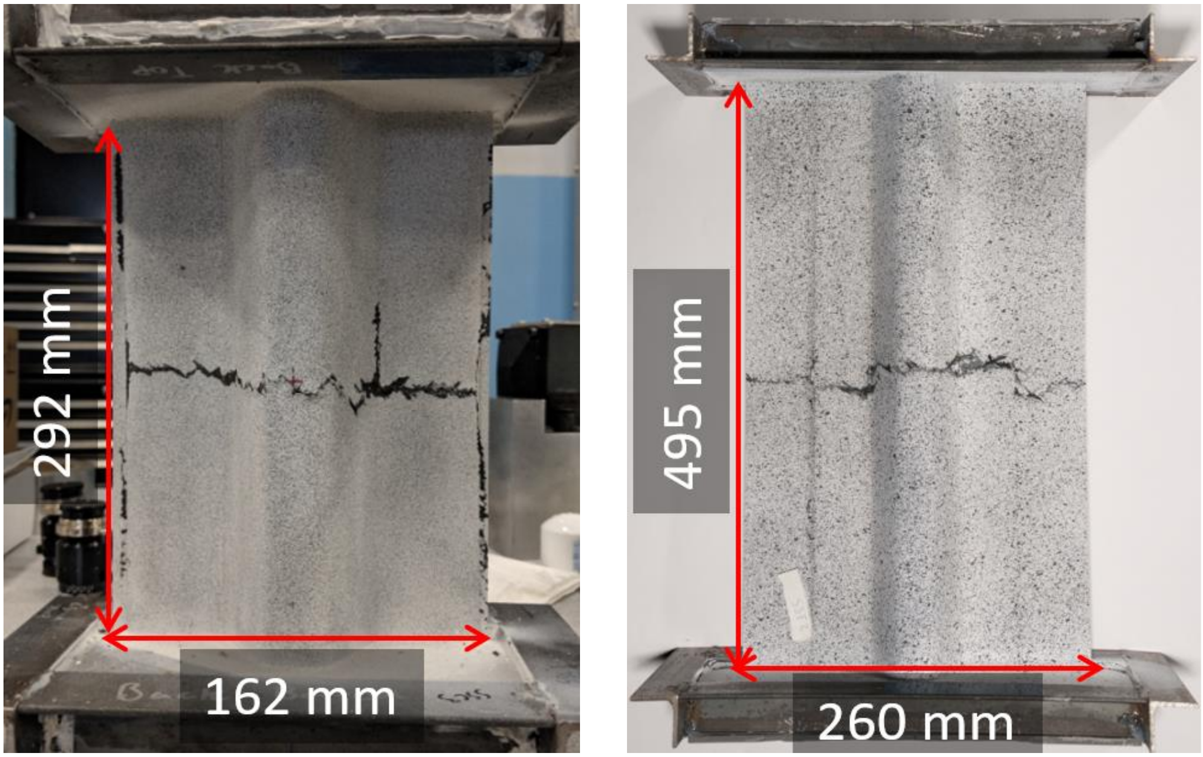

(a) (b)

Figure 3.2.1.3. Potted and compression tested (a) cap and (b) flange impacted specimens

Table 3.2.1.1: FSPs experimental results summary

	Specimen ID	Impact Energy		Inbound speed v_{in} [m/s]	UT A-Scan Damage Span [mm]	CAI Failure Load [kN]
		Target [J]	Actual [J]			
FSP1	S4PC1	0	-	-	-	456.8
	S1PC2		-	-	-	478.3
	SSC2	30	28.85	3.35	76	-
	S1C3		28.41	3.33	68	-
	S2C1		28.36	3.32	77	-
	S3C1		28.49	3.33	78	-
	SSC1	50	47.30	4.29	89	
	S2C2		47.58	4.30	81	205.2
	S3C2		47.58	4.30	78	-
	S4C3		47.11	4.28	96	216.6
	SSC3	70	66.50	5.09	98	113.4
	S2C3		65.72	5.06	88	-
	S3C3		65.87	5.07	96	-
	S4C2		66.65	5.09	96	104.6
FSP2	S5PF1	0	-	-	-	471.0
	S3F1	90	84.48	5.74	-	347.2
	S3F2		82.72	5.68	-	347.2
	S4F1	70	64.81	5.02	-	-
	S4F2		64.81	5.02	-	376.2

3.2.2. Conventional NDE Inspection

Impacted panels were UT A-scanned using hand-held Pocket UT from Mistras with a 3.5 MHz delay-line transducer. Damage areas discovered from the A-scan were highlighted as shown in Figure 3.2.2.1 that shows 28 J impact resulted in damage on the cap of the stringer only, while 47 and 66 J impacts generated damage that expanded down to the web. Damage span on the cap and the web expanded according to the increase in impact intensity on stringer cap, and it did not expand further onto the flange. From visual inspection, blunt impact with the 50.8 mm diameter tip left only a small dent at the Center-of-Impact (COI) on the cap, and it is notable that 66 J impacts which left barely visible matrix crack.

Flange impacted stringers were also A-scanned and this showed trapezoidal damage shape in Figure 3.2.2.1: damage span opens wide towards the skin bay (towards away from the stringer) and closes narrow towards the stringer web (towards the center of the stringer). Even though skin-to-stringer disbond was clearly identified from the Time-of-Flight (TOF) of the UT scan results of the flange impact, they were not visually perceptible.

Prior to the CAI tests, the potted single-stringer specimens were UT and x-ray CT scanned (NASA Langley Floating automated UT system for C-scan and North Start Imaging X3000 for x-ray CT scan) [30]. Due to the curved geometry of the omega stringer from the stringer-side, the C-scan was performed on the cap of the stringer only for the cap-impacted specimens that well captured damage severity only on the cap of the stringer. The C-scan for the flange-impacted specimens presented an excellent quality scan image (see Figure 3.2.2.2). C-scan results were post-processed to separate damage into three modes based on TOF interpretation: skin laminate damage, skin-to-stringer disbond, and stringer flange laminate damage (see Figure 3.2.2.3) [30]. In contrast to the UT scans, the CT scans provided excellent and fair quality cross-sectional images for the cap-impacted specimens and flange-impacted specimens, respectively (see Figure 3.2.2.4).

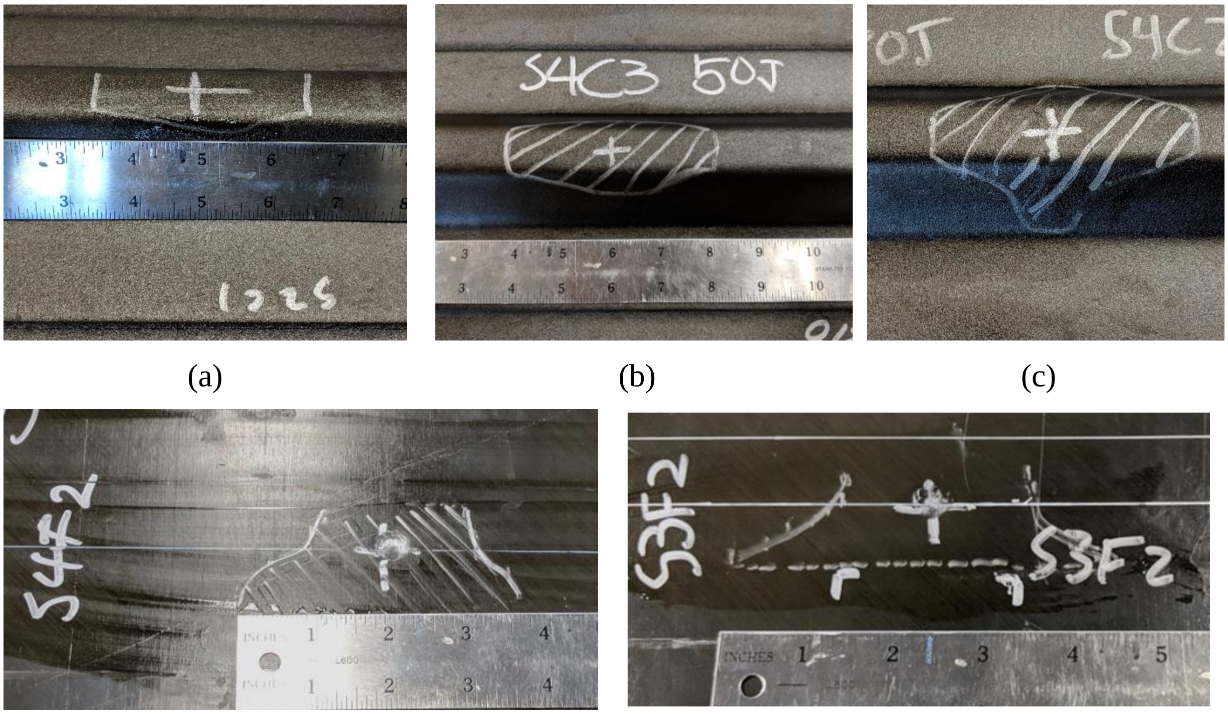

(a) (b) (c)

(d) (e)

Figure 3.2.2.1. Hand-held UT scan for cap impact damage for (a) 28 J, (b) 47 J and (c) 66 J ,and flange impact damage for (d) 65 J and (e) 83 J

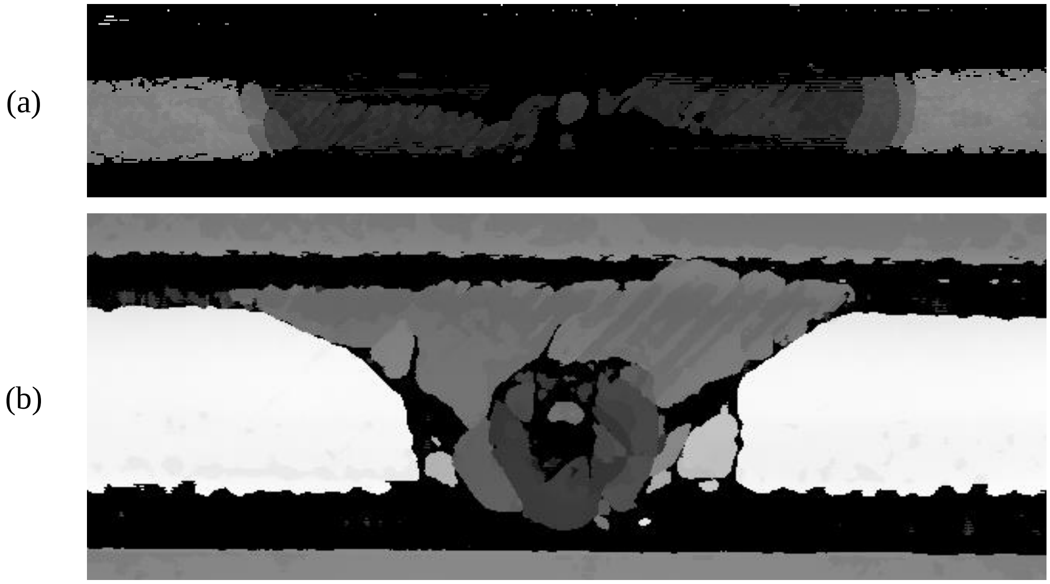

Figure 3.2.2.2. Floating System UT C-scan for (a) 66 J Cap-Impacted S4C2 and (b) 84 J Flange-Impacted S3F1 [30]

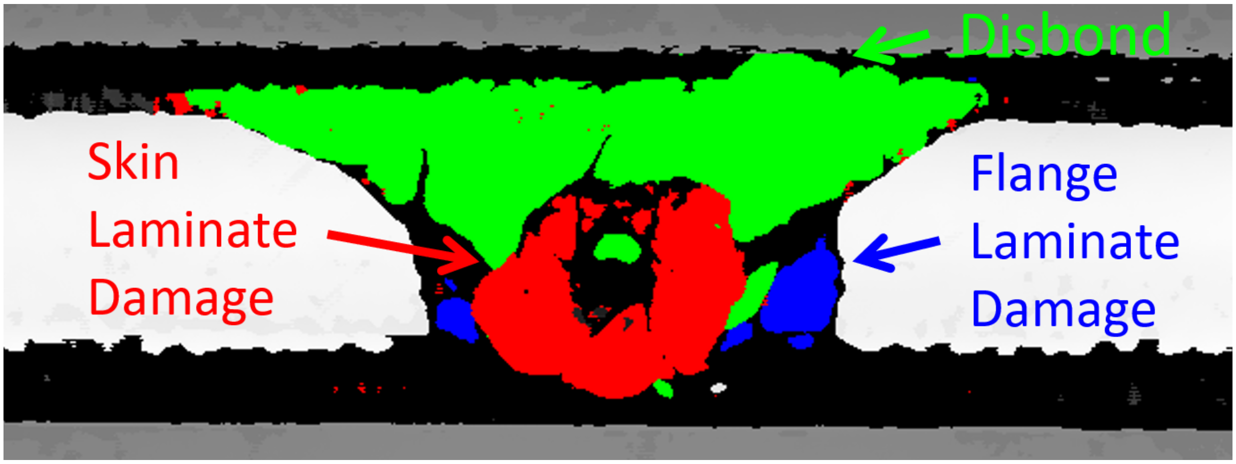

Figure 3.2.2.3. Color-coded S3F1 C-scan for damage type segments [30]

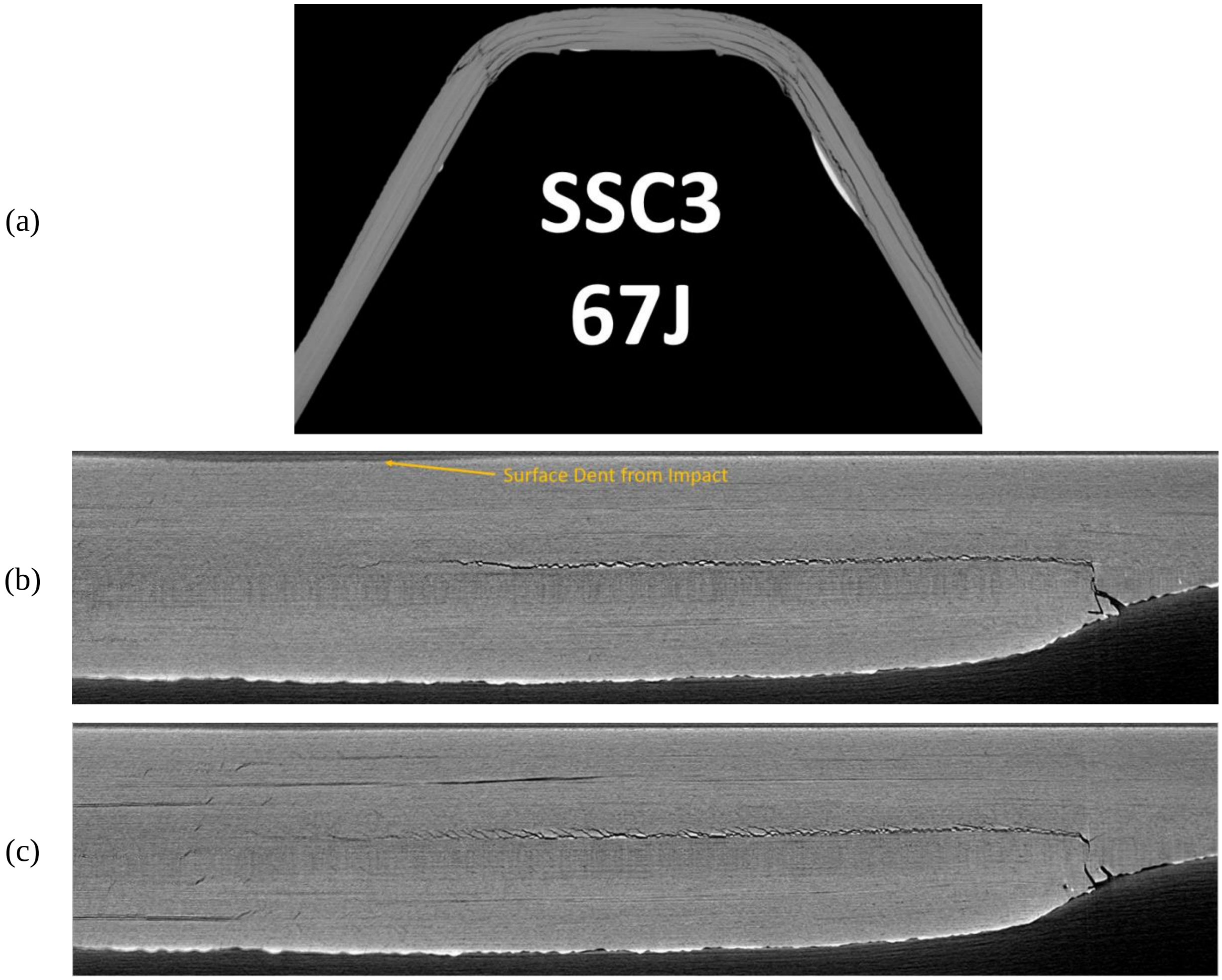

Figure 3.2.2.4. Cross-sectional CT scan image of the (a) 67 J cap-impacted SSC3, and (b) 65 J flange-impacted S4F1 at COI and (c) 1.5 cm away from COI [30]

3.3. UGW Tests

3.3.1. Test Setup

UGW tests were performed on the panels using three systems: non-contact rapid scanning cart system (developed for HEWABI stringer panel scan), semi-contact hybrid system with a Mini-impactor and Broadband Air-coupled Transducer (BAT) receivers, and contact scan with R15S transducers. But only the hybrid system will be discussed herein, because the cart and contact scan systems (delved in the previous chapter) were performed as a supplemental study to verify test methods developed for the HEWABI panels work on different composite structures as well. UGW tests were performed only from the external skin-side to fulfill the main objective of the research to non-invasively detect and characterize the impact damage on composite structures.

UGW baseline data of each panel were collected after holes were drilled on the panel for the pendulum impactor fixtures (UGW test configuration as shown in Figure 3.3.1.1 and Figure 3.3.1.2); location of the holes were used as a guide to determine expected impact location to conduct UGW scanning according to the presumed COI (see Figure 3.1.2). For cap- and flange-impacted regions, scanning spans were 17 cm and 21 cm, respectively, with center of the scan at the COI. UGW post-impact data were collected from the same location and the same setup as the baseline. All UGW tests were performed on the whole panel (five-stringer FSP2 and four-stringer FSP1, because one stringer section was trimmed from FSP1 to perform survey impacts) to minimize boundary reflection interference.

A mini-impactor and dual Broadband Air-Coupled Transducers-1 (BAT-1) from MicroAcoustic was set for guided wave excitation and acquisition to scan the stringer as shown in Figure 3.3.1.1. A PC-based Oscilloscope PicoScope 4824 was used to acquire received data from BAT-1 transducers and Q-Amps from MicroAcoustic were utilized with BAT-1 sensors to condition received signals before recorded. UGWs from the hybrid system was acquired using a ‘Simple Edge Trigger Mode’ on the PicoScope 6 software, triggered to acquire data when receiver 1 signal rose above the set amplitude threshold level. The mini-impactor was triggered manually using a 6.35 mm thick slider, and time offsets on few data signals were observed because signals were acquired from an amplitude-based trigger from receiver 1 (excitation intensity difference led to acquisition time offset). All received waveforms were cross-correlated to be aligned prior to signal processing, which is discussed later in detail.

BAT-1 transducers were tilted about 13° from the normal to the skin surface towards the excitation source to optimize flexural wave sensitivity, based on Snell’s law in Equation (3.3.1.1), for the air-coupled transducers. Incident angle (θ_i) of the leaky wave to the receiver transducers was calculated from experimentally determined flexural wave velocity (v_f), 1500 m/s from guided wave testing at 150 kHz on the panel, and flexural wave angle from the skin surface (θ_f) equal to 90°. Receiver sensors were equally distanced 95.3 mm away from the center of the stringer to receive UGW from the skin bay at the entrance and exit of the stringer across the wave path and the mini-impactor was located 63.5 mm away from the receiver 1 as seen in Figure 3.3.1.1. Neoprene foam sheet was placed between the mini-impactor and receiver 1 as a shield to block the air-transmitted waves from interfering with the guided waves transmitted from the specimen to the receiver sensors. UGW scan was performed at 1cm resolution along the stringer, manually positioned as shown in Figure 3.3.1.2.

$$\theta_i = \sin^{-1}\left(\frac{v_i}{v_f} * \sin\theta_f\right) \tag{3.3.1.1}$$

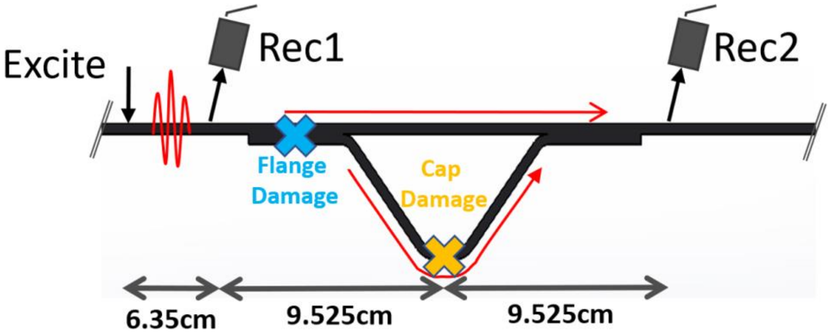

Figure 3.3.1.1. Hybrid UGW test schematic

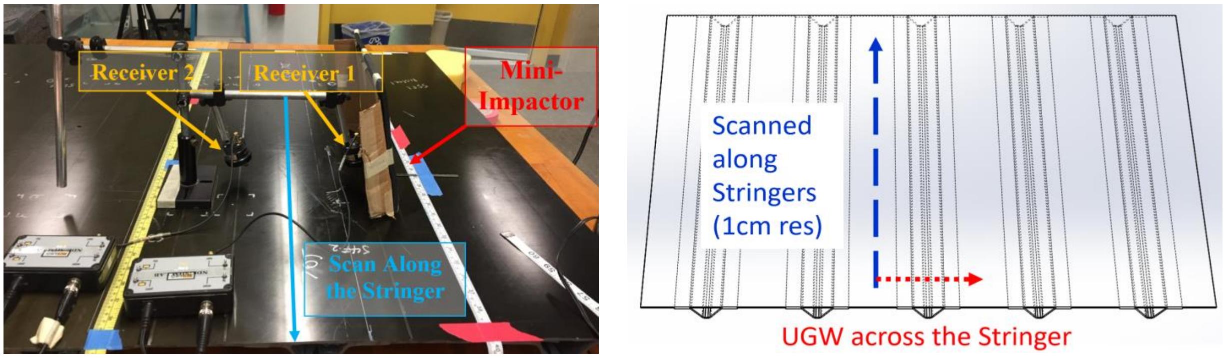

(a) (b)

Figure 3.3.1.2. Hybrid scan system – (a) mini-impactor excitation and two air-coupled receivers setup and (b) UGW scan plan schematic

3.3.2. UGW results

UGW data collected from the hybrid system were first processed to re-arrange time misaligned signals. UGW tests were repeated 10 times per scan location to average the results. The results of two scan locations, damaged and undamaged, from post-impacted FSP2 are shown in Figure 3.3.2.1. Although most received signal data were consistent as shown in the raw signals of Figure 3.3.2.1.b, only a few misaligned signals had to be re-arranged as shown in Figure 3.3.2.1.a. Time delays (D) between $S1_{NL}$ and $S1_{r}$ were extracted from cross-correlation based time delay estimation (TDE) [30]. $S1_{NL}$ represents arrays of signals in N number of repeated tests per L number of scan location and $S1_{r}$ is the reference signal, the first signal of the first scan location from each stringer, pristine location. Peaks of the cross-correlated signals, R, were evaluated from the expected value function (Equation (3.3.2.1)) and the corresponding time delays between cross-correlated signals were extracted from arguments of the maxima function (Equation (3.3.2.2)) for all UGW test results [30].

$$\mathrm{R} = \mathrm{E}\{S1_{r},(t) * S1_{NL}(t + D)\} \tag{3.3.2.1}$$

$$\mathrm{D} = \mathrm{argmax}\ (\mathrm{R}) \tag{3.3.2.2}$$

The time delays were applied to the signals of the corresponding test to align all receiver 1 signals to the reference signal. Guided waves signal results of receiver 2, that propagated across the stringer, were shifted by the same time delay from the corresponding receiver 1 signals. Figure 3.3.2.1 shows that the signals were aligned accordingly and consistent after the alignment. Since the cross-section of the stiffener region was consistent along the pristine stringers, time of flight (TOF) difference of UGWs between receiver 1 and receiver 2 theoretically should be zero without defects. In other words, receiver 2 signals will have a TOF change only if a time-delaying structural abnormality is present between receiver sensors (i.e. impact damage on stringer that could affect wave path length or wave speed).

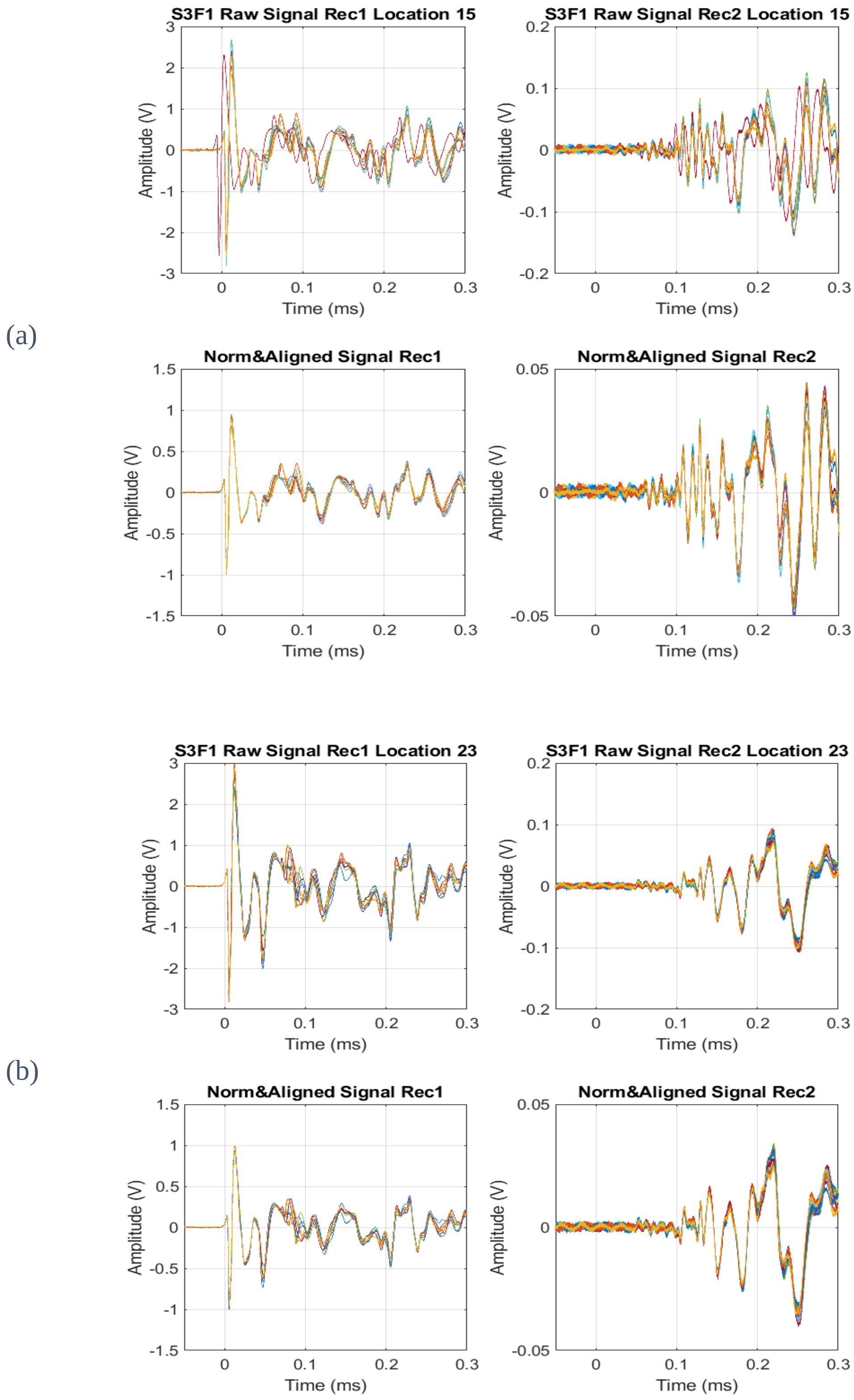

Figure 3.3.2.1. Post-impacted scan of S3F1 at (a) undamaged and (b) damaged location: before and after correlation of receiver 1 and receiver 2 for signal alignment

Receiver 2 signals were Hanning window-gated for the first two wave packets (see Figure 3.3.2.2) to analyze the structure for different damage modes. Gate span for first and second wave packets was selected to contain first symmetrical wave modes (S0) and anti-symmetrical wave modes (A0), respectively, from experimental group velocity investigation of the panel for the range of frequency the panel was inspected. Only receiver 2 results were analyzed and discussed herein, even though results from receiver 1 may be analyzed for complex reflected waves from the damage for more comprehensive damage investigation.

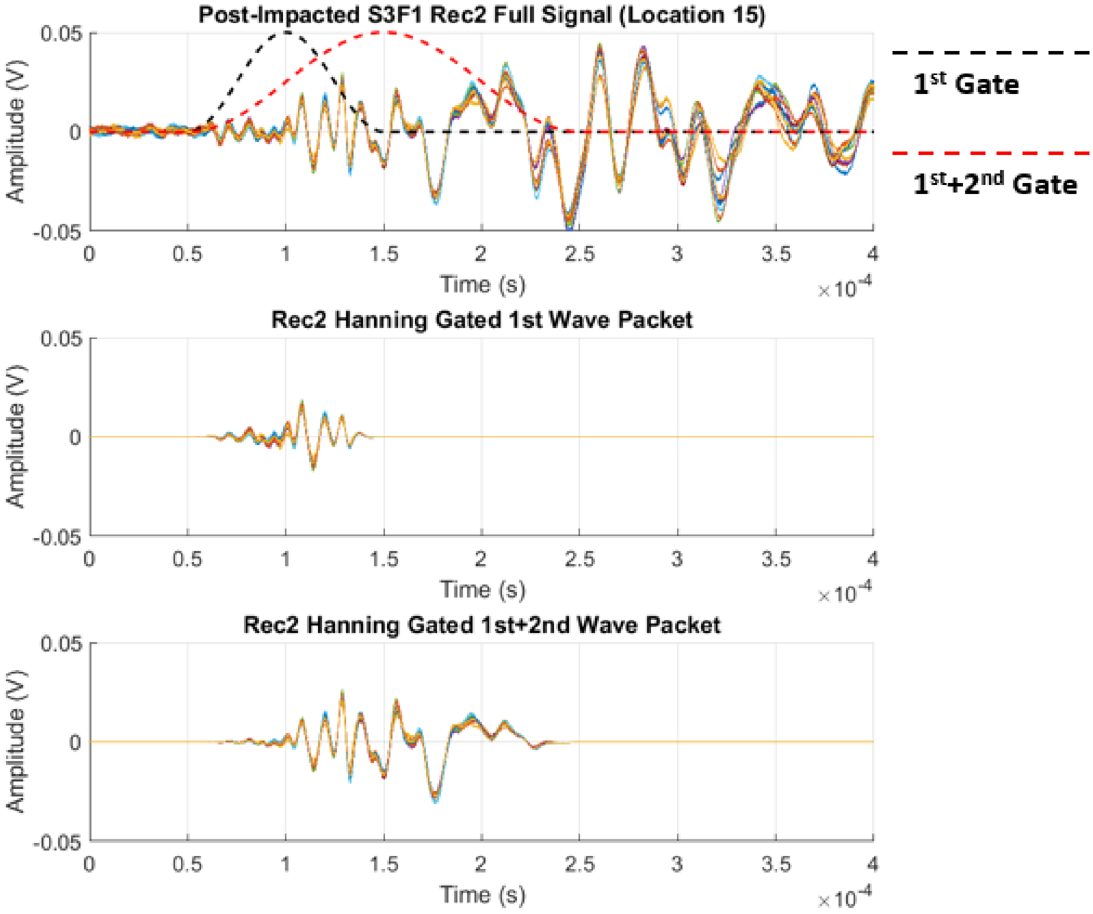

Figure 3.3.2.2. Hanning window gated receiver 2 signals from undamaged location for time (1st gate) and amplitude feature (1st + 2nd gate) extraction

3.3.2.1. FSP2 – Impact Damage Detection on Stringer Flange

The aligned receiver 2 signals from FSP2 were post-processed to identify the UGWs time lag induced from the stringer flange impact damage. Max peak time indexes of the gated 1st wave packet for every scan location were compared for each region of FSP2. Max peak time indexes, the time features, of post-impacted UGW tests certainly show time lag at the center of impact (COI) (Scan #11) compared to other locations (Scan #6 and #16) as shown in Figure 3.3.2.1.1. Time features extracted from 10 tests per location were averaged and plotted to the scan locations for all four regions in Figure 3.3.2.1.2. Time features of the post-impacted results compared to the baseline clearly display increase in time indexes at the impact-damaged regions on the stringer flange. Time index increase is proportional to the impact level as reported in Table 3.2.1.1: time lags induced from impact damage were discernibly higher for 84 J (S3F1) and 83 J (S3F2) compared to the regions impacted at 65 J (S4F1 and S4F2). The COI locations of each region were identified by the dip in the time index curve. Time index dip at the impact center can be correlated to lower damage severity at the impact center perceived from UT in Figure 3.2.2.3 and CT in Figure 3.2.2.4.

Minor discrepancy of the baseline time indexes of each scanned location was observed, and that could have been generated from several factors: thickness variation (±0.04 mm from the average thickness) throughout the panel from rough surface finish, 40 kHz surround noise in the facility where testing was performed, and/or minor impact intensity differences from manually triggered mini-impactor. Despite the discrepancy, difference between time indexes at the COI, TOF_{COI}, and average time index of the baseline of each region, $TOF_{Baseline\_avg}$, correspond to impact levels listed as Δt in Table 3.3.2.1.1.

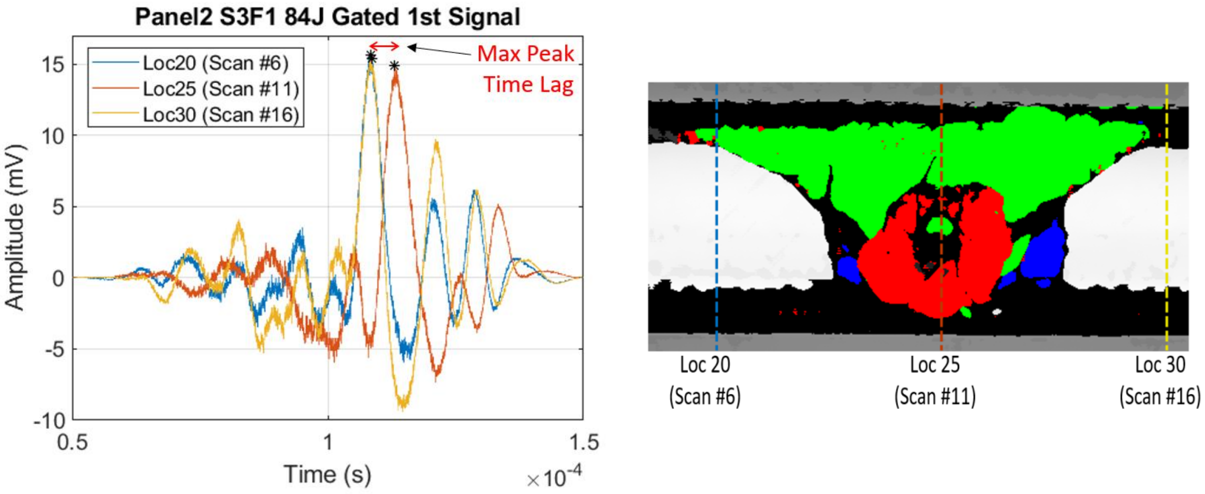

(a) (b)

Figure 3.3.2.1.1. Comparison of (a) max peak time of gated 1^{st} wave packet and (b) UT C-scan at three scan locations for S3F1

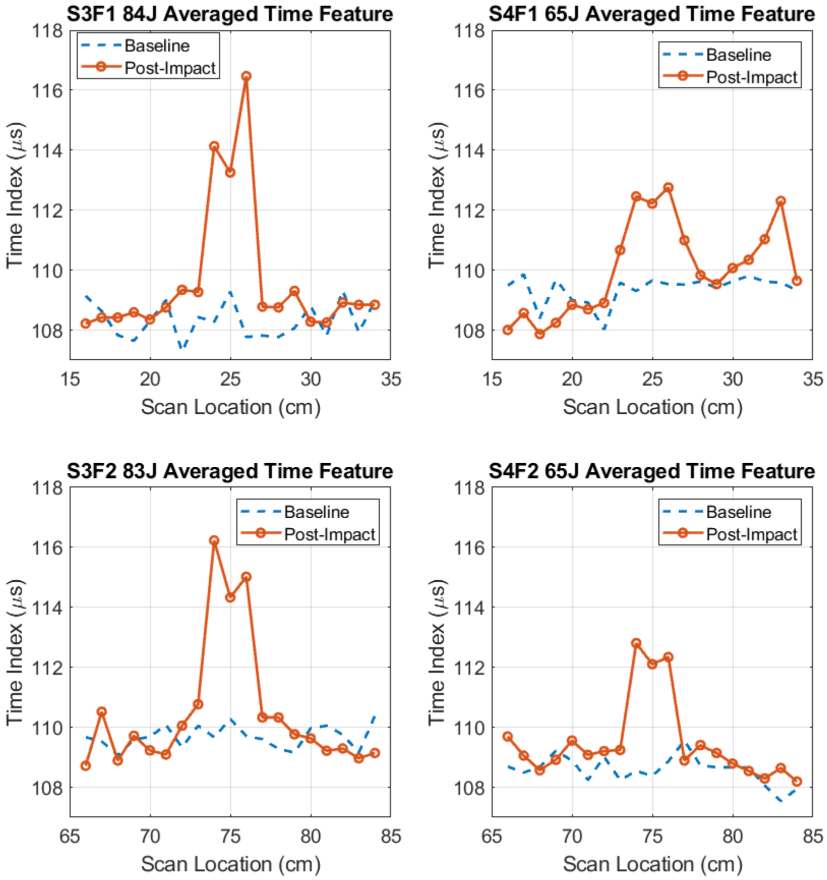

Figure 3.3.2.1.2. Averaged time feature index comparison of pre-impact baseline (blue dashed line) and post-impact results (red solid line) for all four impact damaged regions

Furthermore, time features were compared to the skin damage pixel counts (red C-scan zone) extracted from the UT C-scan at 1 cm resolution (see Figure 3.3.2.1.3). UGW time feature plots show remarkable match to the skin damage pixel count plots for the damage span and severity. UGW time features and UT skin damage pixel counts both display about 4 cm damage span. Pixel counts of the skin damage were greater for higher impact intensity (S3F1 and S3F2) compared to lower intensity (S4F1 and S4F2) -- same scale and trend as the time feature results. UT C-scan did not capture skin damage mode at the COI location, which generated the “dip” in the skin damage pixel counts profile for all regions.

Table 3.3.2.1.1: FSPs UGW test summary

	Region	Impact [J]	TOF$_{COI}$ [μs]	TOF$_{COI}$ – TOF$_{Baseline\_avg}$ Δt [μs]	RMS$_{COI}$ [mV]	RMS$_{COI}$/Impact [mv/J]
FSP2	S4F1	64.81	112.2	3.5	4.4	0.0682
	S4F2	64.81	112.1	2.8	4.4	0.0682
	S3F1	84.48	113.3	5.0	3.7	0.0436
	S3F2	82.72	114.3	4.6	3.8	0.0458
FSP1	S2C1	28.4	-	-	6.3	0.296
	S2C2	47.6	-	-	5.8	0.202
	S2C3	65.7	-	-	8.2	0.186
	S3C1	28.5	-	-	8.3	0.296
	S3C2	47.6	-	-	9.7	0.202
	S3C3	65.9	-	-	12.3	0.186

Uneven damage severity near the impact center from skin damage pixel count observed from the UT C-scan matched very well with the time feature profile together with the dip at COI. Pixel counts of flange damage (blue C-scan zone) were not considered in the damage severity comparison profile because severe flange damage is mostly hidden under the skin laminate damage, which was already considered under skin laminate damage pixel counts (also observed from CT scan image in Figure 3.2.2.4). UGW time feature results of post-impacted FSP2 was not affected by the skin-to-stringer disbond damage type (green C-scan zone in Figure 3.2.2.3), because 1st gated wave packet was thought to contain S0 wave modes only, that has in-plane motion only at the midplane. Hence, UGW time lag of S0 modes was ascertained to identify the skin and/or flange laminate damage mode only.

The amplitude features, root-mean-square (RMS), of the Hanning window-gated 1st + 2nd UGW signals of receiver 2 (Figure 3.3.2.2) were investigated. Amplitude feature profiles of each region were plotted together with skin-to-flange disbond damage pixel count profiles from the UT C-scan in Figure 3.3.2.1.4 and their comparison show a reasonable match. RMS of the UGWs decreased from the scattering of the waves when interacting with flange impact damage that generated concave up profile of the amplitude features. Therefore, pixel count profile of skin-to-flange disbond damage was plotted in reverse manner (pixel counts increase downward). Although a portion of the disbond damage mode was hidden under the skin damage mode from C-scan, amplitude feature profile followed similar trend as C-scan disbond damage pixel count profile for all regions. It is hypothesized that the profiles were well-matched because skin-to-flange disbond damage does not completely expand under the skin damage, as the CT image shows in Figure 3.2.2.4.

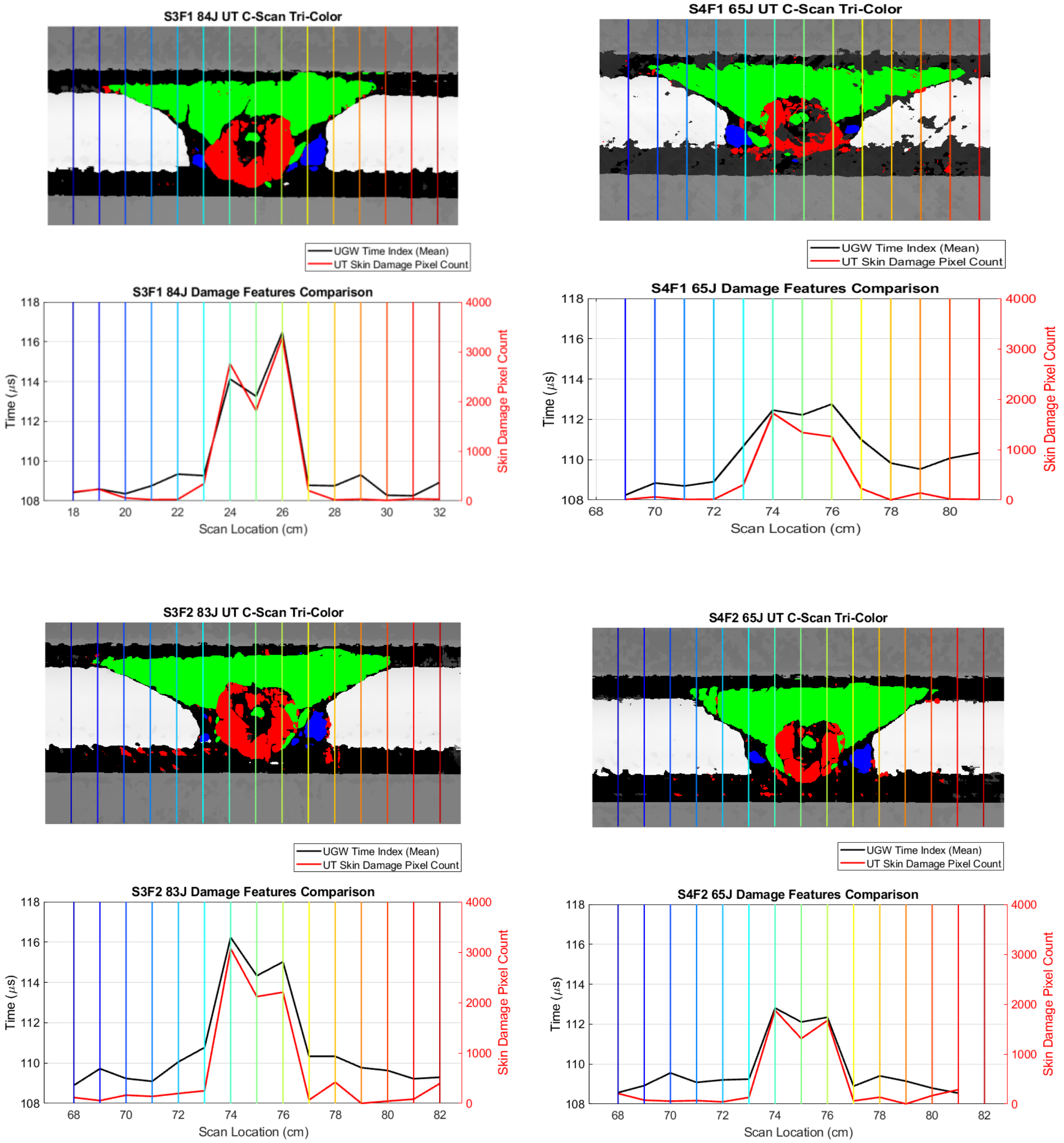

Figure 3.3.2.1.3.UGW time index compared to UT C-scan skin damage pixel count

RMS values of both 1st + 2nd wave packets were used because the 2nd wave packet, anti-symmetric mode, combined with the 1st wave packet improved amplitude feature results with more intense magnitude variation than the 1st or 2nd wave packets independently. Impact locations were also identifiable with a “spike” on the RMS profiles caused by reduced wave scattering at the COI. Moreover, RMS values at center of impact, RMS_{COI}, were inversely proportional to impact energy level as listed in Table 3.3.2.1.1 (higher RMS for lower impact level).

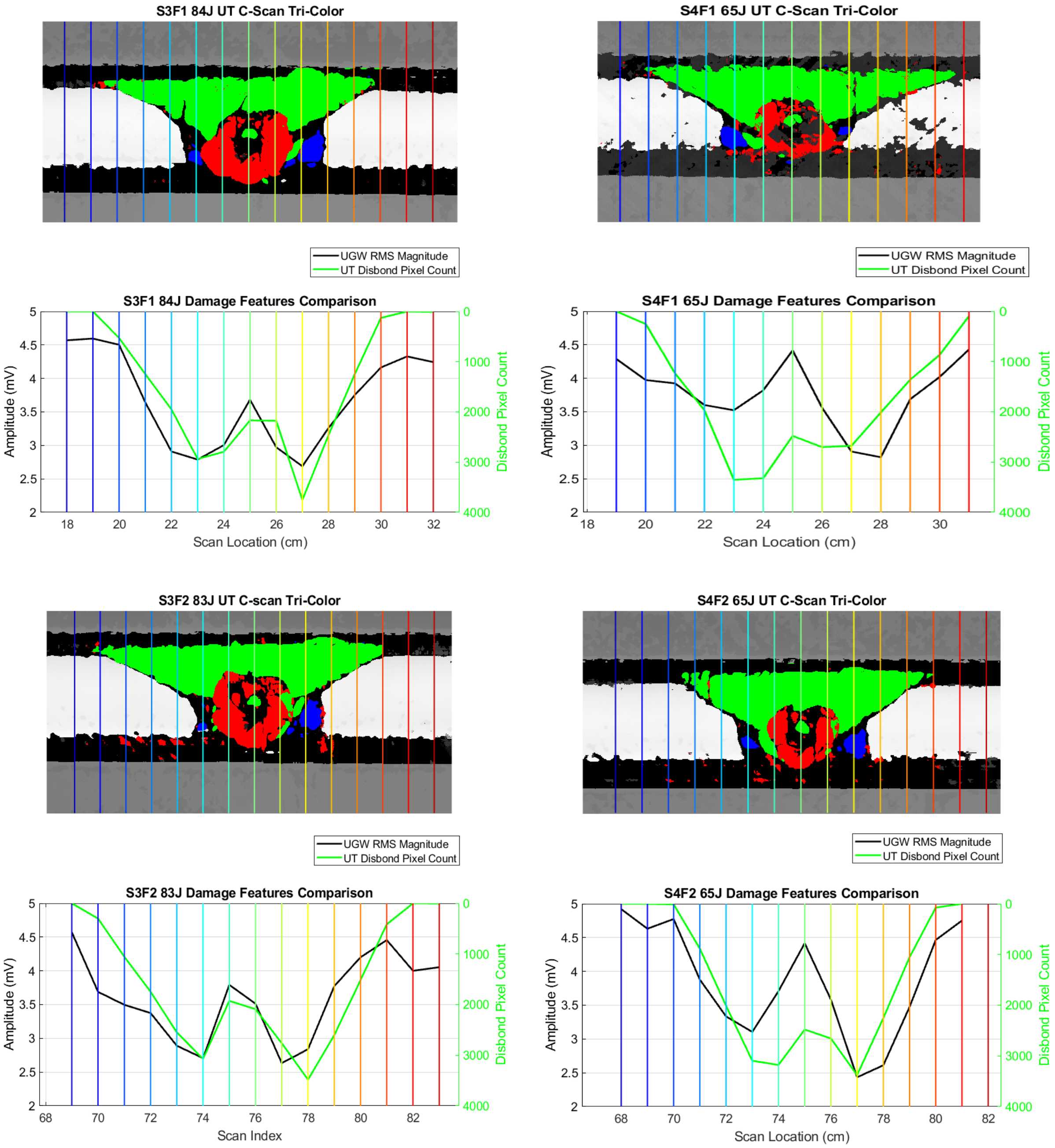

Figure 3.3.2.1.4. UGW RMS compared to UT C-scan disbond damage pixel count

3.3.2.2. FSP1 – Impact Damage Detection on Stringer Cap

UGWs propagated across the stringer with cap-impact damage on FSP1 were investigated in the same method as FSP2 as discussed in the previous section: time features of gated 1st packet and amplitude features of gated 1st + 2nd wave packets were evaluated. Time feature results did not draw any damage information of the stringer cap damage from FSP1. Even though the amplitude feature results of cap impact damage have drawn proportional relationship to the impact levels (higher RMS for higher impact level), they were not comparably investigated to the UT C-scan. UT C-scan only captured the damage on the crown of the stringer despite the damage extension down to the web of the stringer for 47 and 66 J cap-impacted regions (as seen in Figure 3.2.2.1 and Figure 3.2.2.4) due to complex curved geometry of the stringer. In contrast to the RMS values reduction behavior observed for the impact damage on the stringer flange, RMS values increased when the impact damage was located on the cap and/or web of the stringer as UGWs transmitted across the stringer section.

Peak of the RMS values were located at the COI, RMS_{COI}, which increased proportionally with respect to the impact levels. Increase of amplitude features with the damage presence along the wave path was an unanticipated UGW behavior which requires further investigation. However, it could be best interpreted that the stringer cap damage limits UGWs transmission to the stringer path that yields more UGWs transmission through the skin path at wave path split; similar behaviour of the wave reviewed from the bolted joint studies on HEWABI Frame02 panel (Section 2.4) that transmitted wave energy (external skin path) increased when leaked wave energy was reduced (internal shear tie path).

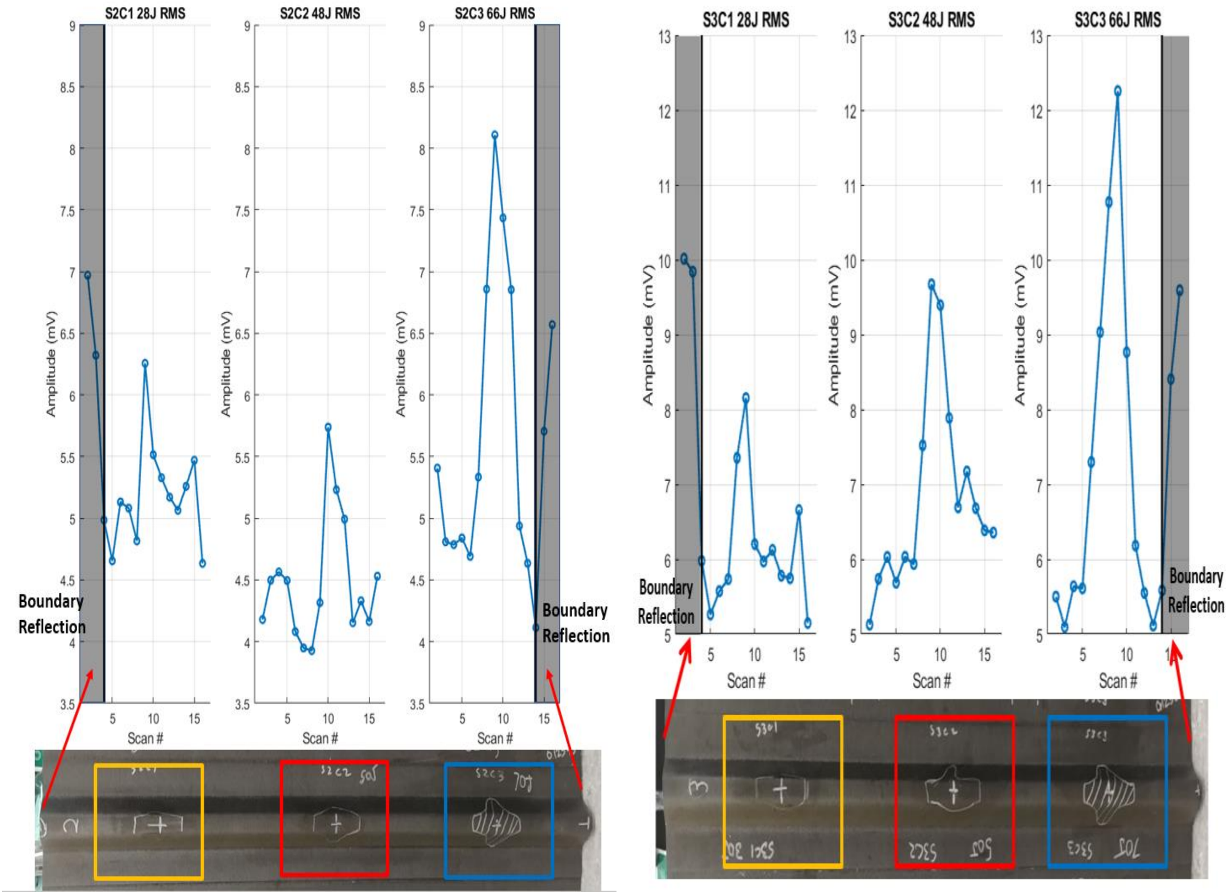

Figure 3.3.2.2.1. RMS Results of Stringer 2 (left) and Stringer 3 (right) Cap-Impacted Regions

3.4. Discussion

UGW experiment using a hybrid system included an extra step: signal alignment in time domain using cross-correlation process. If the mini-impactor, which is still in the development stage, can be established as a data acquisition trigger, then signal alignment process could be eliminated. Even with an extra process, UGW experimental results with aligned signals showed high potential in allowing the exploration of different damage modes, location, and severity of blunt impact damage on the cap and the flange of the stringer, despite the complex damage modes. In addition, impact level on the structure was studied to directly affect how UGWs propagated across the COI, based on time and amplitude features correlation. Preliminary guided wave testing on the structure was first performed to empirically understand group wave velocity of a specific range of frequencies to increase the precision of structural damage investigation with correct gating of wave packets. Impact level and location evaluated from UGW experiment results could be used to estimate residual strength of the structure if parametric study of residual strength to the impact damage relationship is established (further discussed in Chapter 4).

UGW tests on stringer panels particularly focused on a mini-impactor with two air-coupled receivers system to establish a portable UGW test system that could be utilized in the field (e.g., on aircraft sitting at airport ramp). Narrowband frequency UGW tests that is more sensitive to the specific damage type could generate much more sophisticated results than the current hybrid system. Additionally, optimal UGW feature selection [31], other than time and amplitude features, can be investigated to build more details about the complex impact damage modes.

3.5. Conclusions

Two large-sized panels, each having five omega-shaped stringers, were impacted at the cap and flange of the stringer, and subsequently compression strength tested (after being trimmed into smaller single-stringer-sized elements) to quantify residual strength of the bluntly impacted structure. NDE methods were conducted on the panels prior to the compression test and its results were compared for different impact levels at regions of the panels. Severity of the damage increased along with the impact energy and it was noted that the impacted location, or COI, remained almost damage-free as observed in the UT and CT scan results.

Panels were UGW scanned across the impact damaged regions with scans performed along the stringer at 1 cm resolution. UGW time and amplitude features were investigated to show their proximity to the damage location, modes, and severity. RMS value variances were identified to locate and examine severity of the damage on the stringer. Impact damage on stringer cap and flange showed increase and decrease in RMS values, respectively, and RMS values corresponding to the severity of the damage. Time delays of the gated symmetrical wave mode were studied to find complex flange impact damage modes (i.e., matrix crack, fiber breakage, and delamination) separate from skin-to-stringer disbond damage. Lastly, all time and amplitude feature results were studied to have close link to the impact energy. Discussion of the residual strength of the stringer panel relationship to the extracted amplitude features will be covered in the following Chapter 4.

Acknowledgements

Chapter 3 work was work compiled from collaboration with Andrew Ellison and Margherita Capriotti, sponsored by NASA Langley and the FAA. Panels were manufactured with Andrew with the help from Chaiane Wiggers De Souza and Moonhee Nam, along with other undergraduate students, Paul Lee and John Hamrang. UT C-scans and x-ray CT scans of the specimen were carried out by Andrew during his internship at NASA Langley, after panel impact tests and compression specimen preparation were completed by him. UGW tests and data analysis were done together with Margherita and frequent meetings with Andrew and Margherita helped optimize the results presented herein.

Chapter 3 contains material currently being prepared for submission for publication. Capriotti, Margherita; Ellison, Andrew; Kim, Hyungsuk E.; Lanza di Scalea, Francesco; Kim, Hyonny. The dissertation author was the primary investigator and author of this material.

4. UGW Results for Residual Strength Estimation

Aircraft that have undergone accidents must be evaluated for damage tolerance levels by assessing damage presence and severity on the structure using NDE techniques. Especially, structure with damage severity higher than the allowable damage limit per FAA Advisory Circular 20-107B guidelines [7] (i.e., damage tolerance level below ultimate load level) should be detected to perform necessary structural repair. UGW test methods conducted from the exterior skin of the composite panel (mentioned in previous chapters) successfully detected blunt impact damage induced on the internal components, and the test results were assessed for damage type, location and severity. Damage assessment from UGW test results were comparable to the damage map produced from well-established NDE techniques, proving feasibility of UGW-based damage tolerance level estimation.

BID characteristics assessed from two features, arrival time and amplitude of transmitted waves, extracted from UGW test data changed noticeably when stress waves interacted with damage modes in composite structures. Damage acts as a "waveguide" that impedes transmission of waves by slowing and scattering them (e.g., voids, typically smaller than a wavelength), and reflecting and guiding waves to detour around the damage when acoustic impedance mismatch is high (e.g., discontinuity). Hence, features of transmitted UGWs are directly related to the damage within the path, and correct analysis of UGW output data would provide adequate estimation of the damage. UGW test result at the damage center is hypothesized to be related to the damage severity as the wavefront interacts with the whole area of damage, and damage characteristics defined from a line-scan UGW test can be investigated to estimate residual strength of the composite laminate.

In this chapter, the amplitude feature of the UGW results were first correlated to the residual strength of an open-hole notched composite laminate. The relationship of open-hole notched composite strength to UGW was first studied using finite element analysis modeling and then investigated via experimental analysis. Damage tolerance analysis from the UGW amplitude features was evaluated only from the UGW line-scan results at the center of the damage. Next, UGW results and residual compressive strength of the flange blunt impacted stiffened panels were examined in a similar manner as the hole-notched coupons' correlation.

4.1. Background

Residual strength prediction based on linear elastic fracture mechanics (LEFM) has been studied for composite laminates with notched damage types as shown in Equation (3.2.1.1) [22] σ_r is the stress level at crack length, $2L$, (refer to Figure 4.1.1) with fracture toughness of the material, K_{IC}. Exponent value, m, is an empirically defined parameter.

$$\sigma_r = K_{IC}(\pi L)^{-m} \tag{4.1.1}$$

Figure 4.1.1. OHT tension test coupon with DIC speckle pattern

A two-parameter model, Equation (4.1.2), showed successful estimation of residual tensile strength of notched coupons. σ_0 is the material strength and L_0 is the intrinsic defect size that withstands material strength [23].. Studies have found that the exponent value, m, for composites is always smaller than the exponent value of isotropic materials due to pseudo-plastic behavior at the crack tip [23]. The two-parameter model was further explored to predict the residual compressive strength of impacted composite laminates [24]. Notch dimension, L, and Impact energy, U, were expressed in a simple power law correlation as shown in Equation (4.1.3), where k is a scale factor and n is an exponent value ($n > 0$). Combining these equations, a new two-parameter relationship was expressed in Equation (4.1.4), where $U_0$is impact energy that produces damage equivalent to the intrinsic defect size and $\alpha = mn$.

$$\frac{\sigma_r}{\sigma_0} = \left(\frac{L_0}{L}\right)^m \tag{4.1.2}$$

$$L = kU^n \tag{4.1.3}$$

$$\frac{\sigma_r}{\sigma_0} = \left(\frac{U_0}{U}\right)^\alpha \tag{4.1.4}$$

Residual strengths of composite laminate were estimated from non-destructively evaluated ultrasonic attenuation measurements for void content levels. Ultrasonic attenuation coefficient, α, from through-transmission test results was correlated to the various void content cases on the composite laminate and strong correlation of interlaminar shear strength to attenuation coefficients was observed [25]. An attenuation slope was developed from a linear-fitted attenuation coefficient with respect to the frequency, $d\alpha/df$, and was examined to estimate interlaminar shear strength by correlating the attenuation slope to the damage size in

Equation (3.2.1.1), which imposes strength reduction similar to crack damage cases on composite laminate (see Equation (4.1.5)) [26].

$$\tau_f = C\left(\frac{d\alpha}{df}\right)^{-m} \tag{4.1.5}$$

4.2. Open-Hole Tension (OHT) Analysis

UGW tests were conducted on open-hole notched composite laminates before and after holes were introduced to the specimen. UGW measurement (non-destructive) was investigated for the relationship to the residual tensile strength (destructive) of the composite from through-hole damage. The relationship between non-destructive and destructive measurements was first studied via finite element model analysis. Then the experimental study of various hole notch sizes was examined from a composite plate.

4.2.1. Finite Element Analysis

FE model was generated using commercial, Abaqus, to study how guided waves pass through open hole notched composite laminates of varying notch (i.e., damage) sizes and also how residual tensile strength of the laminate could be correlated to UGW results. A carbon/epoxy (Cytec X840/Z60 fabric) composite laminated beam (300 mm x 100 mm x 2.9 mm) with $[0]_{13}$ layup was simulated to run case studies on UGWs transiting through various hole notch diameters from 0 to 50 mm (see Figure 4.2.1.1). Tensile failure model analysis was also conducted for composite beam with gage length 305 mm and thickness 2.9 mm. For each diameter notch hole sizes analyzed for tensile strength (2.3, 3.4, 6.35, 12.7, 19.1 and 25.4 mm), widths were determined by width-to-diameter ratio of 4-to-1. Material properties for the model are in Table 2.1.2.

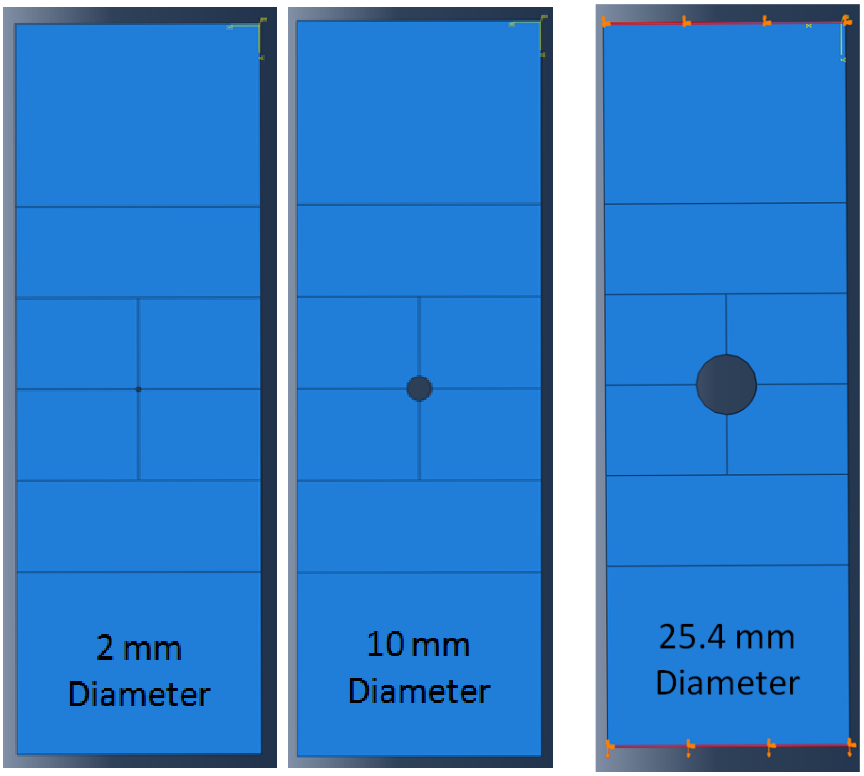

(a) (b)

Figure 4.2.1.1. UGW FE model simulation: (a) UGW model with 2 and 10 mm center hole notch and (b) tensile model with 25.4 mm center hole notch for W/D = 4

Abaqus Explicit solver was used to analyze both guided waves and tensile load simulation. For the guided waves simulation, explicit central-difference time integration rule was considered to determine the mesh size and time increment [32-33]. Minimum time increment is defined by Equation (4.2.1.1) , where L_e and C_d are minimum element size of the model and dilation wave speed, respectively. And the maximum mesh size, L_{max}, was determined from Equation (4.2.1.2) with the minimum group velocity from the dispersive guided wave, C_{min}, for the test frequency, f. It is a widely used rule to allow set minimum elements, n_{min}, from 8 to 10 per wavelength [33].

$$\Delta t \leq \left(\frac{L_e}{C_d}\right) \tag{4.2.1.1}$$

$$L_{max} < \frac{C_{min}}{(f * n_{min})} \tag{4.2.1.2}$$

Dynamic explicit analysis was used to simulate guided waves with continuum shell elements (SC8R). A five-cycle Hanning windowed tone burst nodal load, applied in direction normal to the plane, was excited for the following center frequencies: 150, 400 and 600 kHz. Guided waves propagated directly across the center of the hole notch region and were received as shown in Figure 4.2.1.2.

Received UGWs (out-of-plane displacements) for multiple hole notch simulation were plotted, and first symmetric and anti-symmetric wave modes were gated based on the displacement investigated from top and bottom surfaces (see Figure 4.2.1.3). Received waves were Hanning window-gated for the first wave modes as shown in Figure 4.2.1.4 and S0 mode is discussed for the simulation result since it is free from mixed wave modes or boundary-reflected waves. Wave amplitude of gated signals was observed to attenuate more with increased hole notch sizes. Root-mean-square (RMS) values of the gated signal results for the notch radius curves were divided by pristine un-notched RMS value and plotted (see Figure 4.2.1.5 for 150 kHz as well as 400 and 600 kHz), which show an exponentially decaying plot that is similar to typical residual strength vs. damage size plots [22-24]. Greater RMS ratio decaying was observed for higher test frequencies, which may be wave attenuation as a function of frequency over distance wave traveled.

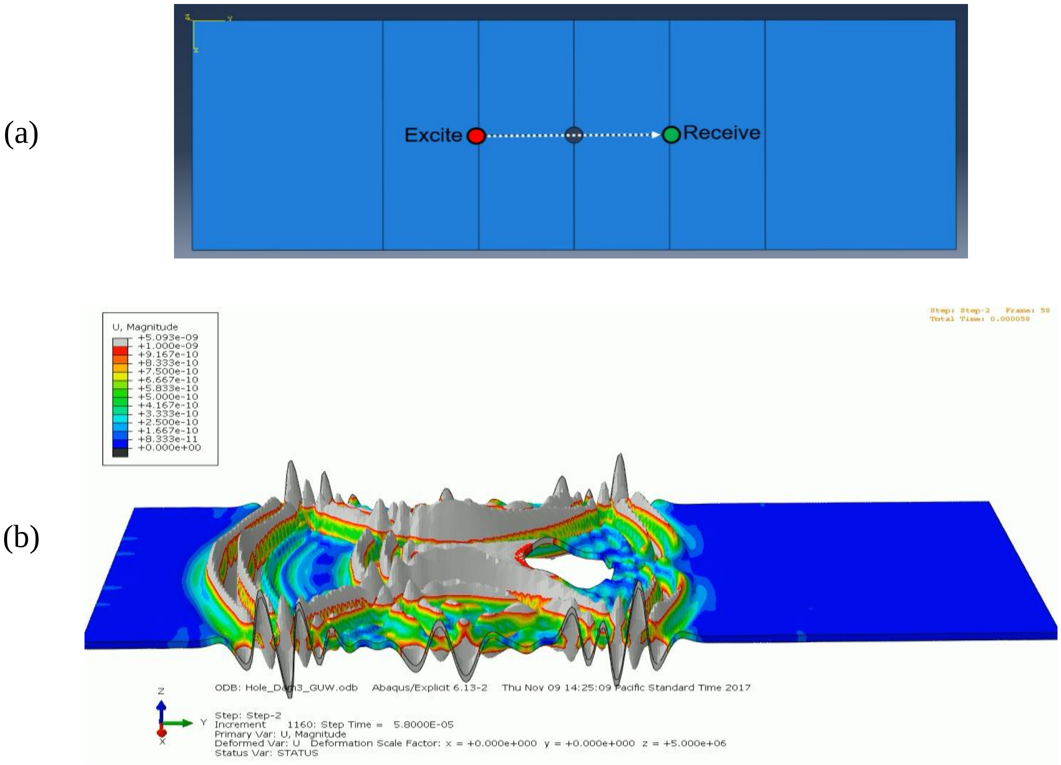

Figure 4.2.1.2. UGW FE model simulation: (a) UGW line scan through center of hole notch schematic and (b) A0 wave mode propagating around hole

A line scan of UGWs through the center of the damage showed that wave energy attenuates relative to the damage size based on results of the FE model studies. If damage size or severity can be estimated based on guided wave attenuation rate, then estimated damage size can be implemented to evaluate residual strength. RMS ratio, which expresses UGW attenuation rate relative to undamaged case, to the hole notch radius shows attenuation rate that is dependent on frequency. Time delay of the UGW packet was also observed from Figure 4.2.1.4, which may also be used as a parameter to estimate damage severity. However, time-based results are not covered in the dissertation.

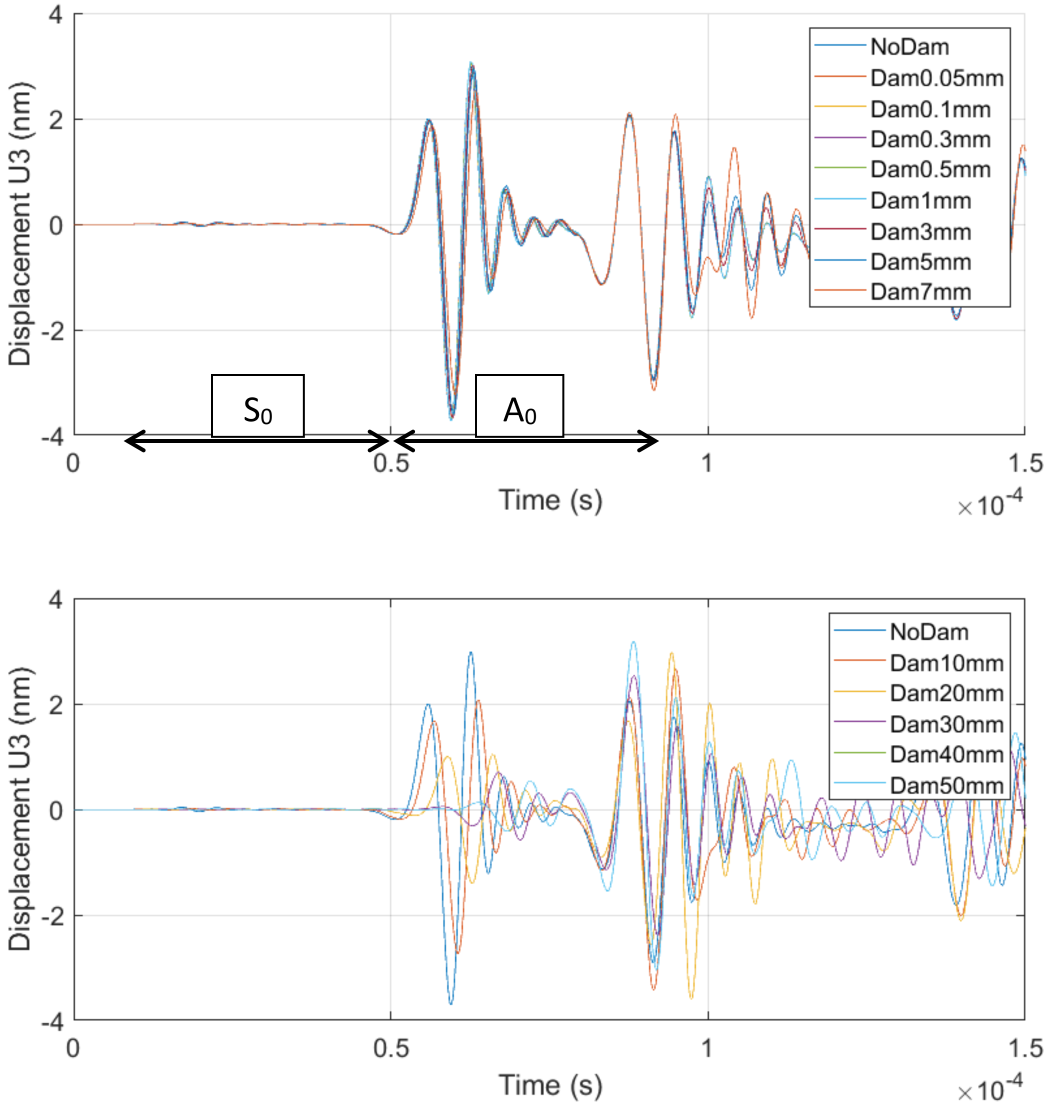

Figure 4.2.1.3. UGW results from FE simulation for 150 kHz: S0 and A0 modes as shaded

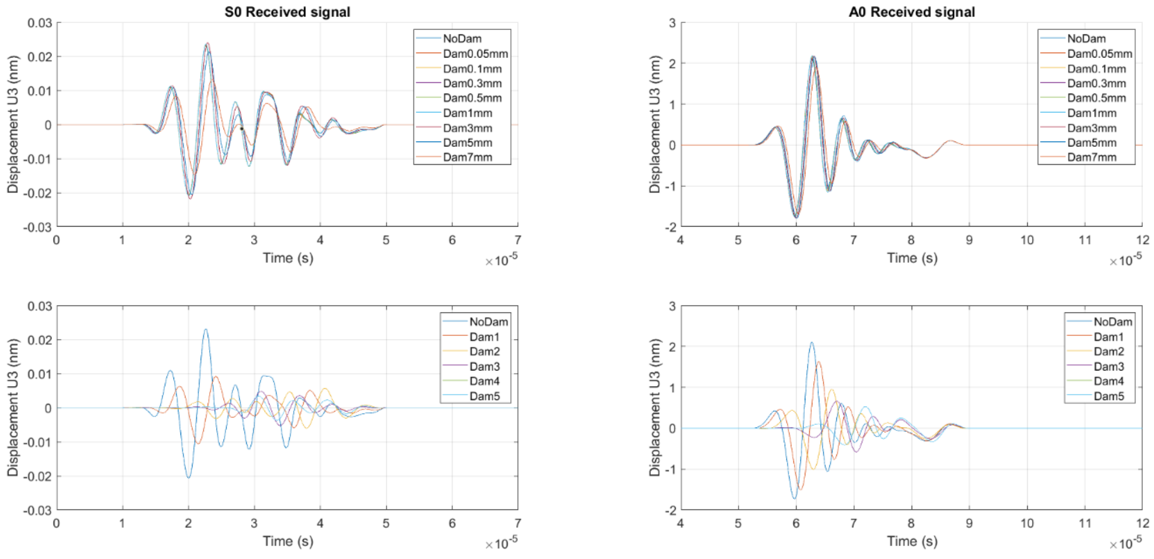

(a) (b)

Figure 4.2.1.4. UGW simulation results gated for (a) S0 mode and (b) A0 mode for 150kHz test frequency for various hole notch diameters

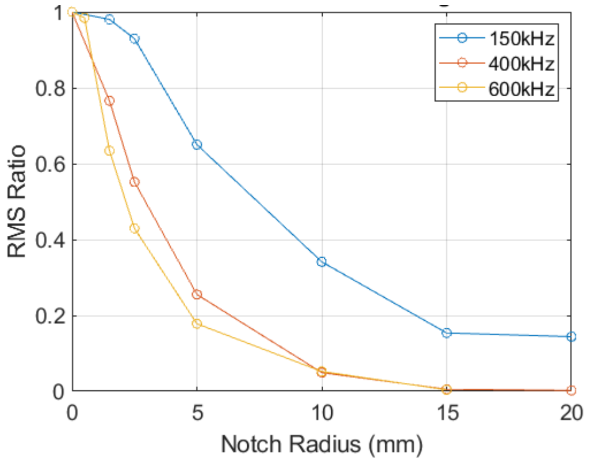

Figure 4.2.1.5. RMS ratio of gated S0 mode UGW signals from FE simulation for various test frequencies to multiple notch radii

4.2.2. Experimental Studies

A plain weave carbon/epoxy (Hexcel 282/SC-780) composite laminate of layup $[0]_{10}$ was fabricated as a large plate. Baseline UGW line scans, aligned to the center of pre-assigned hole notch locations, were collected at each region on the pristine large plate (see Figure 4.2.2.1).

Baseline UGW signals were collected with contact transducers in six assigned regions referred to as D1 to D6 for hole notches of diameters 2.2, 3.5, 6.4, 13.7, 20.0 and 26.6 mm, respectively in ascending order (see Figure 4.2.2.2.c). Excitation and receiver transducers were positioned along the same linear path, 152.4 mm away from the center of the hole in opposite directions as shown in Figure 4.2.2.2.c, with excitation and receiver transducers located near the edge and at the middle of the plate, respectively. PICO and R15S transducers were used for UGW tests. UGW tests were performed while the smaller PICO transducers stayed coupled onto the plate, pre- and post-hole drilling, using portable drill-press as seen in Figure 4.2.2.2.a and b. UGW tests with intact coupling of PICO sensors were executed to eliminate effects of test variation from uncoupling and recoupling of the transducers. Also, UGW tests were performed on the full plate, as shown in Figure 4.2.2.2., to neglect boundary reflected waves from interfering with the initial wave modes.

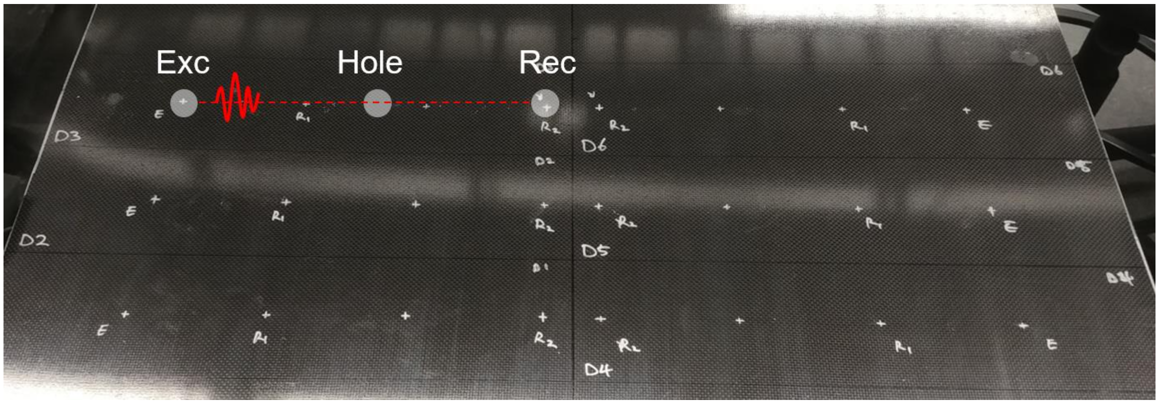

Figure 4.2.2.1. Large composite plate with six regions indicated for open-hole UGW testing

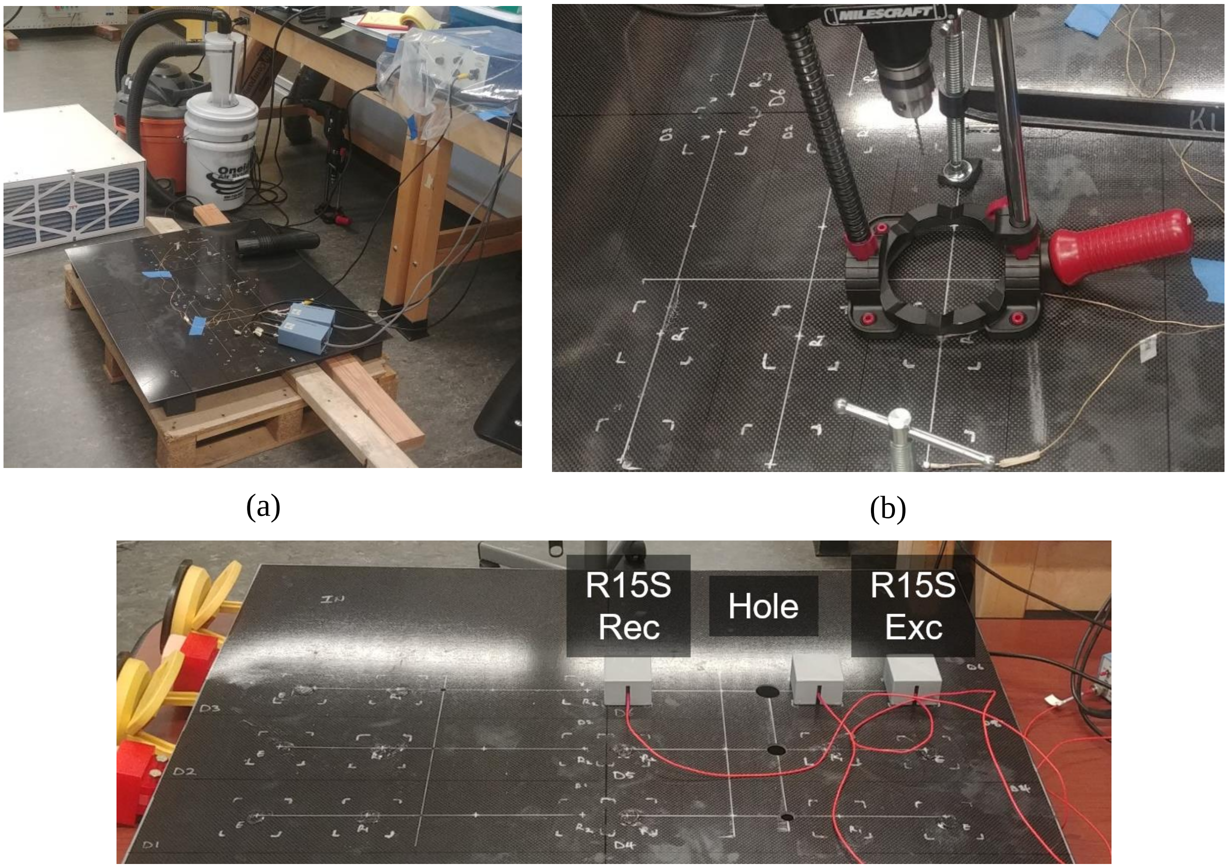

(a) (b)

(c)

Figure 4.2.2.2. UGW test setup: using (a) PICO sensors pre-drilling, (b) portable drill-press setup for hole drilling with PICO sensors coupled, and (c) R15S sensors test with holes

UGW tests were conducted for frequencies in the range of 150 to 450 kHz. Raw signals of pre- and post-drilling UGW test results are shown in Figure 4.2.2.3**.** for 6.4 mm and 20.0 mm diameter holes. UGW comparison of baseline and post-drilling of regions D3 (6.4 mm) and D5 (20.0 mm) show more signal amplitude attenuation for larger hole diameter. RMS of gated first wave packet (S0 wave mode) for post-notched results was normalized by baseline RMS results and plotted versus hole notch radius in Figure 4.2.2.4. RMS ratio results for all test frequencies in Figure 4.2.2.4 show a similar decaying trend as the results from FEA model simulated UGWs in Figure 4.2.1.5: RMS ratio curve shifts lower with increasing test frequency and shows notably higher sensitivity to smaller notch sizes. Comparison of RMS ratio profiles from both the FE model simulation and experiment results (see Figure 4.2.2.5) shows test frequency of 150 kHz has a flat region in the initial profile up to 2 mm – flat region reflects intrinsic defect where strength of the material is not affected. However, damage detection sensitivity increases proportionally to the test frequency, and the intrinsic defect for "UGW" seems to disappear with increased test frequency. Again, this may be caused only due to the increased wave attenuation as a function of frequency over wave propagation distance. However, this decay trend could deliver a different trend based on the damage type (i.e., voids, impact damage, or delamination).

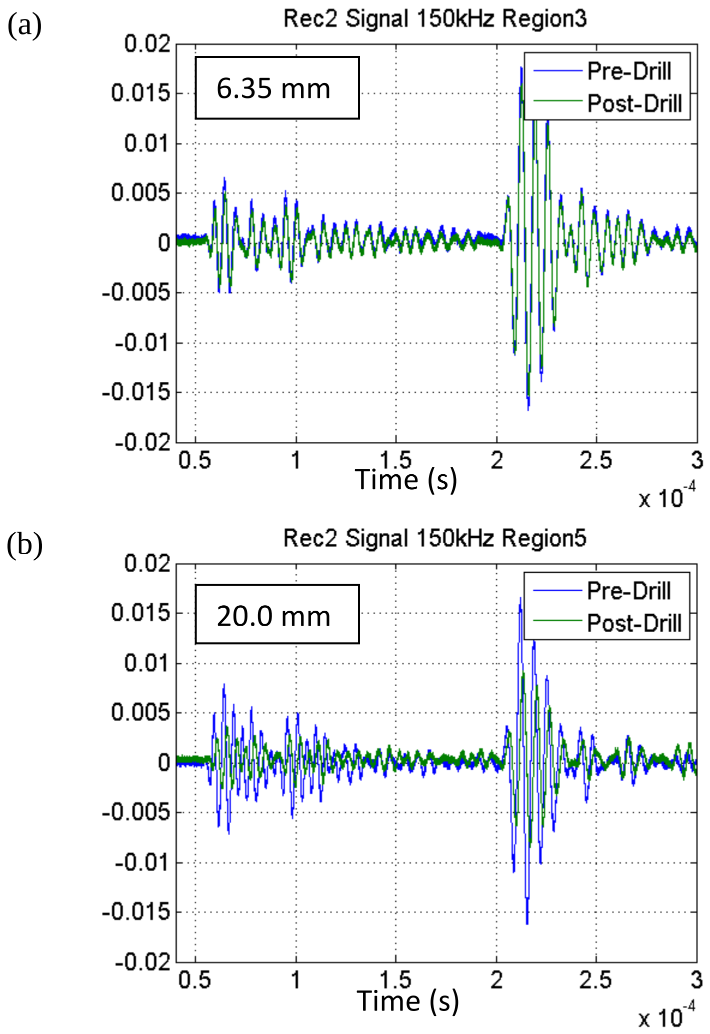

Figure 4.2.2.3. Experimental UGW scan results at 150kHz with PICO sensors comparing pre-drill vs post-drill results for hole notch diameters (a) 6.4 mm and (b) 20.0 mm

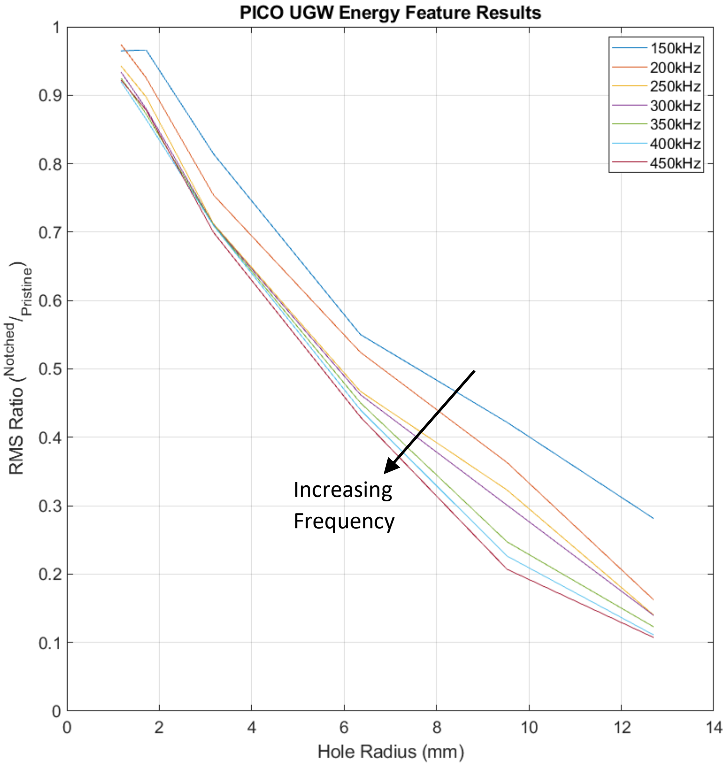

Figure 4.2.2.4. RMS ratio of S0 gated UGW signals for frequencies from 150 to 450 kHz with PICO sensors

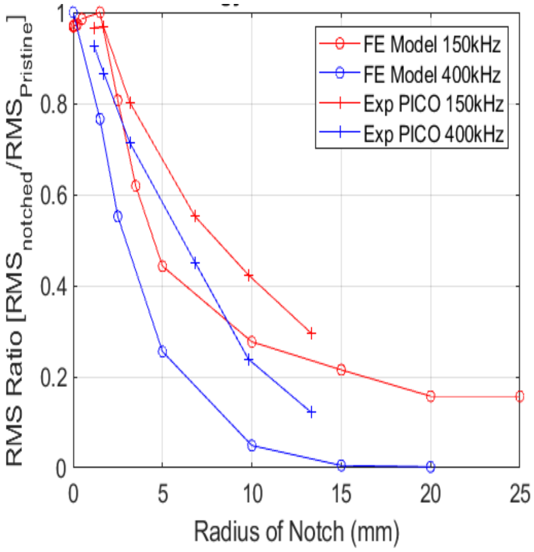

Figure 4.2.2.5. RMS ratio of S0 gated UGW signals comparison for the FE model and experiment

OHT strength coupons were cut out from the large plate (Figure 4.2.2.2) after all UGW acquisition was complete. Experimental OHT coupons were trimmed to a width/diameter ratio of 4 (W/D = 4/1) with gage length of 205 mm and tested (see Figure 4.2.2.6). Average thickness of the laminate measured at 2.4 mm. Tension strengths are reported in Table 4.2.2.1 for two batches of specimens, and force-displacement profile for 2nd batch coupons is shown in Figure 4.2.2.7. OHT tests were conducted on an MTS machine at test rate 0.5 mm/min. Laser extensometer displacement reading was very noisy as shown in Figure 4.2.2.7. Therefore, strain rate was gathered from Digital Image Correlation (DIC) results (see Figure 4.2.2.8a). DIC was used in the tension experiment to confirm uniform strain field is satisfied away from the hole region (see Figure 4.2.2.8.b) for the tension testing with W/D ratio of 4.

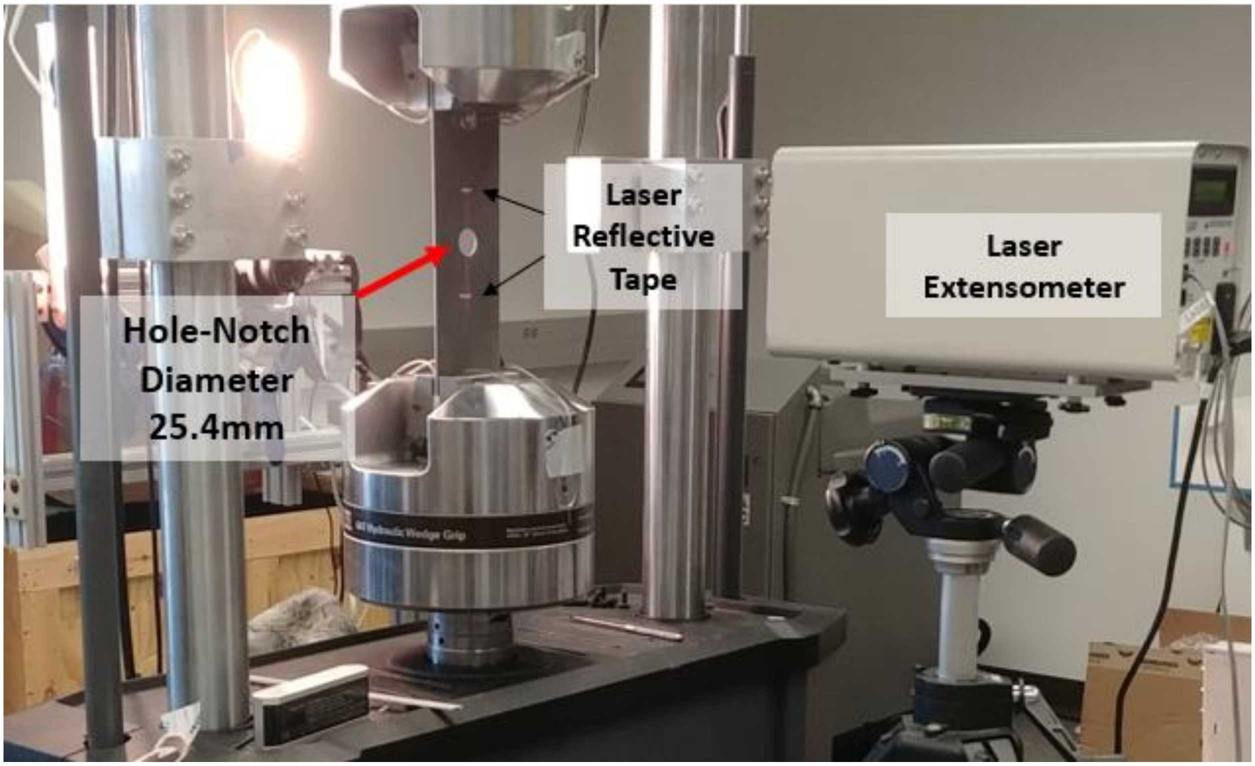

Figure 4.2.2.6. Experimental OHT coupon setup with laser extensometer

Table 4.2.2.1: Open-hole tension (OHT) strength experimental summary

Coupon Type	Hole Dia. (mm)	Width (mm)	Failure Load 1st Batch (kN)	Failure Load 2nd Batch (kN)	Strength 1st Batch (MPa)	Strength 2nd Batch (MPa)
No Dam	0	25.4	37.29	-	61.9	-
D1	2.35	10.46	8.10	-	42.0	-
D2	3.43	14.37	9.38	12.18	36.1	44.0
D3	6.35	24.86	15.52	17.48	35.7	40.5
D4	12.7	50.37	28.49	26.22	33.0	30.2
D5	19.05	78.26	36.07	34.67	26.9	25.7
D6	25.4	99.25	46.82	43.47	26.6	24.3

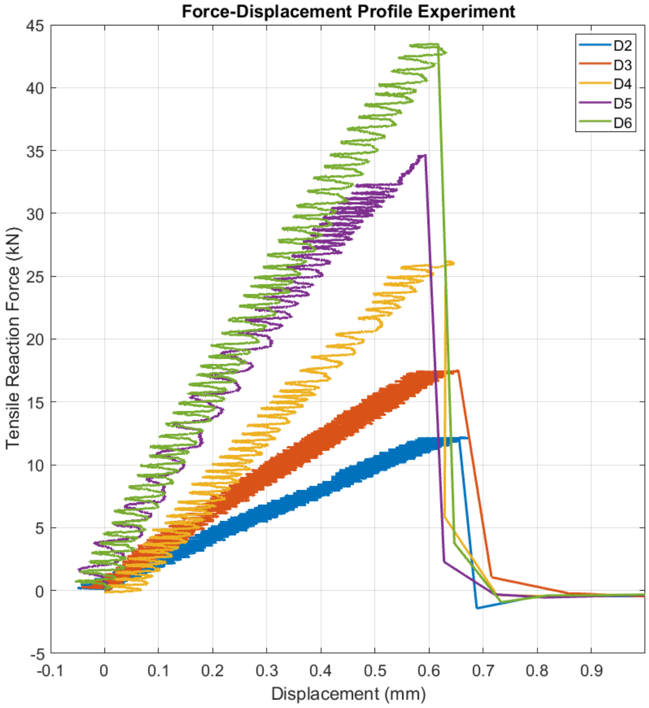

Figure 4.2.2.7. Force-Displacement plot with laser extensometer displacement for 2nd batch

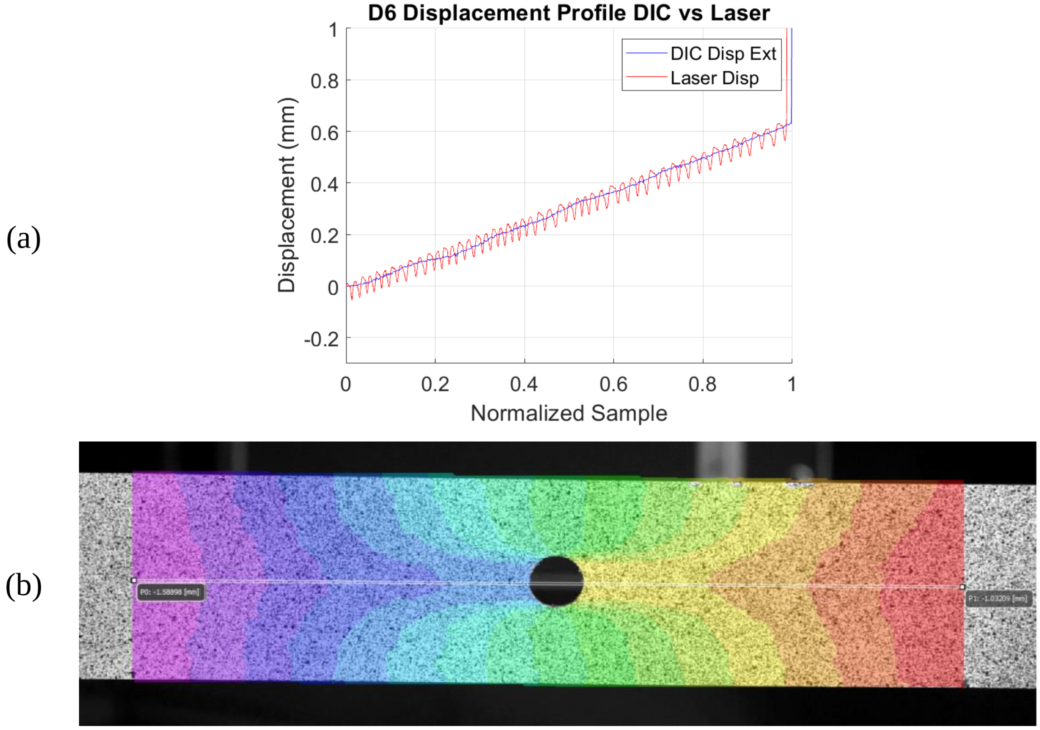

Figure 4.2.2.8. Comparison of (a) DIC vs. Laser displacement profile and (b) DIC displacement field

Figure 4.2.2.9 plots the normalized residual strength (notched strength divided by un-notched strength) from experimental results together with a theoretical fitting curve from the two-parameter model (Equation (4.1.2)). L_0 and m values were evaluated to be 0.73 mm and 0.3, respectively, fitting the experimental results from the 2nd batch specimens. As shown in Figure 4.2.2.9 , residual tensile strengths for D1 and D2 (2.2 and 3.5 mm in diameter) coupons from the 1st batch were lower than the values estimated from the theoretical curve. This is estimated to have been caused due to a few factors: inaccurate trimming of coupons of small width and/or small number of fiber tow carrying the load. From the observation of the 1st batch, it was noticed that D1 and D2 coupons had only one to two fiber tows on each ends of the hole notch.

Exponent value m from this current residual tensile strength testing matched the exponent values listed in Caprino’s work [23]., although the intrinsic defect size seems quite larger than the values determined from other laminate coupons. Also in Figure 4.2.2.9, UGW RMS ratio results for both PICO and R15S transducers at 450 kHz frequency have been plotted via the relationship in Equation (4.2.2.1). This equation was defined to express residual strength as a function of the RMS ratio (attenuation rate) in place of the hole size after a futile attempt to fit linear slope RMS ratio rate to the test frequency, similar to Equation (4.1.5). The parameters c and α are found to be 0.4 and 2.2, respectively, from the current test data but will vary for other UGW frequency, materials, and damage modes. RMS ratio has a similar reduction trend as the strength ratio, which needs to be further studied to correlate how such UGW results could be used to estimate residual strength of impact damaged composite laminates.

$$\sigma_R = \sigma_0 \left(c \times \exp^{\left(\frac{RMS_N}{RMS_0}\right)^{\alpha}} \right) \tag{4.2.2.1}$$

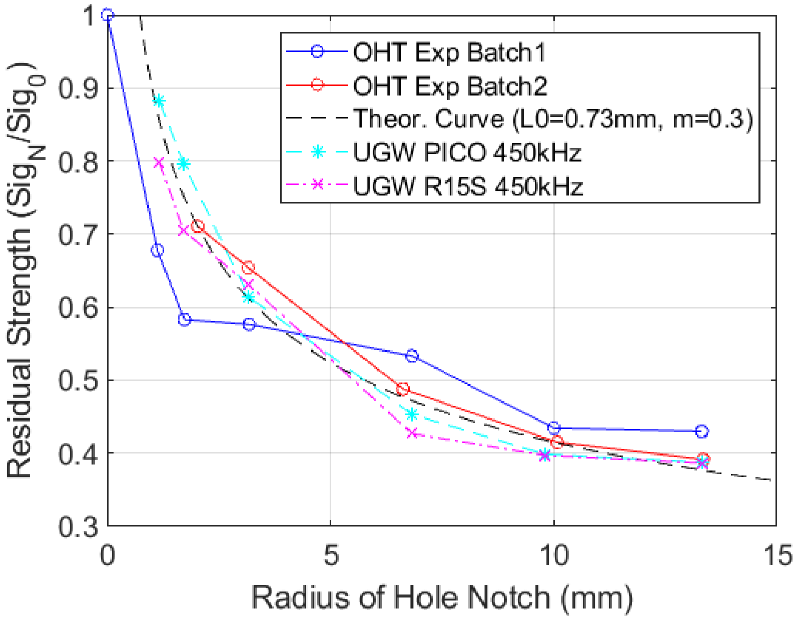

Figure 4.2.2.9. OHT residual strength ratio with theoretical fit of the residual strength and curve fitted UGW RMS ratio at 450 kHz

4.2.3. Sub-Component Level CAI Experiment

The UGW line scan method found to estimate well the residual tensile strength of hole-notched composite laminate was extended to correlate the stiffened composite panel residual compression strength after impact (reported in Chapter 3) with UGW results from center of impact (COI). For the flange impacted panel (FSP2), RMS results from COI were identified to reduce with increased impact energy levels, and RMS ratio was plotted versus the impact energy level together with strength ratio in Figure 4.2.3.1. With only a few data points available, it is difficult to draw any comprehensive generalized conclusion from the plot. However, the results seem to correlate quite well with compressive strength as the UGW RMS value at COI reduces correspondingly with the strength.

Residual compressive strength to UGW RMS correlation was performed using the 1 cm UGW scan resolution results (see Figure 3.3.1.2), and a much higher fidelity result is expected for impact damaged panel UGW scan results taken at a finer scan resolution. Also, impacted stiffener panel results investigated in Figure 4.2.3.1 were performed using a broadband excitation and reception system, unlike narrowband experiments performed for the OHT coupon. Attenuation rate was found to vary based on the test frequency (see Figure 4.2.2.4), and therefore narrowband frequency experiment is anticipated to give more consistent RMS ratio profile for better correlation to residual strength.

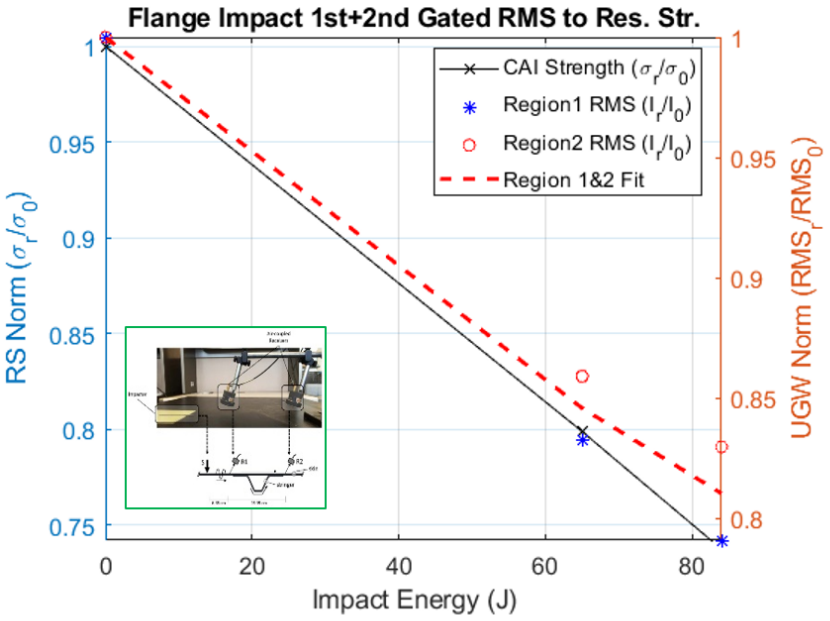

Figure 4.2.3.1. Amplitude feature ratio from COI compared to compression strength ratio

4.3. Conclusions

UGW measurements of various sized hole notched composite laminates were examined to measure the attenuation rate related to open-hole dimensions. FE analysis was used to investigate UGW behavior through various radii open-hole notches, and results from line-scan UGW through the center of the hole were examined for a range of hole radius (e.g., actuation and reception of guided wave aligned to the center of the hole). RMS values of the S0 wave mode showed an exponentially decaying profile versus increased hole radius. It is noted that this relationship is directly similar to the residual strength.

Experimental UGW tests were performed on a large composite plate and transmitted guided waves attenuation rate was examined by comparing the wave energy of the hole notched region to the baseline undamaged data before the hole drilling. While the attenuation rate of UGW was frequency dependent, curve fitted UGW attenuation rate at 450 kHz test frequency showed remarkable correlation to the open hole tension residual strength ratio. FE model and experimental results showed remarkable sensitivity to the defect size as a means of UGW testing. And parametric studies of UGW feature relationship to the residual strength of different loading cases, such as compression, shear, bending, etc., could give more insight on repair necessity -- damage severity estimated from UGW measurements will be fixed while residual strength varies depending on the loading case the structure needs to withstand. UGW line-scan results from impact damaged stiffener panel showed a similar trend, which demonstrates a clear feasibility of UGW-based residual strength estimation of impact damaged composite panels, perhaps even from a single scan result.

5. Conclusions

Non-destructive evaluation technique utilizing UGW was examined on highly complex multi-component joint-assembled composite panels. Thin composite structures generally allow UGW to propagate through a long distance, covering large area scan through continuous waveguides. The main objectives of the research were to use UGW to detect damage and estimate its severity, location and type, and then to estimate residual strength of the structure from UGW damage evaluation. This research focused on detection of blunt impact damage modes generated in the internal structure with UGW test method restricted to external skin-side access only.

Experimental UGW tests were performed on the HEWABI Frame02 panel that is composed of co-cured skin and stringer with bolted joint shear ties and C-frames. Contact-based UGW tests using a mini-impactor and R15S transducer setup identified damage located on bolted joint internal structure. First, UGW test frequency was determined from preliminary study on Frame02 panel: below 50 kHz frequencies found appropriate for multi-bolted joint internal structure scanning, and about 150 kHz for in-plane skin damage focused scanning. Second, the internal frame path transmitted UGW at 40 kHz frequency band. From the mini-impactor excitation on the shear tie joint skin, low frequency (~40 kHz) internal frame path transmitted wave was received by R15S transducer on the skin of an adjacent shear tie bolted joint, and internal frame path transmitted waves of frequency above 50kHz were almost fully attenuated when passing through multi-bolted joint interfaces. Therefore, UGW test results from skin, excited and received signal near 40 kHz frequency band, were transmitted majorly through internal structure of Frame02 panel and were attenuated significantly when damage was located along this guided wave path. Such behavior of internally transmitted waves was perceived from experimental tests based on panel disassembly and a series of bolted joint plates. A major portion of the UGW excitation from the exterior skin side at the shear tie bolted joint regions was perceived to absorb into the internal path (approximately 86%), based on the panel disassembly test, and UGWs transmitted through a series of bolted joints were abruptly attenuated for frequencies above 50 kHz.

Although significant wave amplitude scattering was noticed with internal structure damage, wave energy scattering rate was different for similar damage type and severity at different locations along the wave path. Thus, UGW-based evaluation for damage severity, location, type, and residual strength was not accomplished for the detected damage on complex multi-bolted joint internal structure.

Further experimental investigation of UGW test method was executed on the Stringer03 panel to detect damage on a hat stringer at test frequency of 170kHz. UGW test was performed across the stringer at 1 cm resolution along the stringer using a cart scanning system with non-contact air-coupled transducers. Although details of the damage were not fully analyzed, stringer heel crack and disbond damage types were detected and damage span size along the stringer was estimated from a damage index profile as a function of the scan location. The non-contact cart scan system was able to scan a meter-long stringer member in 8-10 seconds, but adequate averaging with a high-power amplifier system was needed to obtain good quality results (e.g., UGW results with high signal to noise ratio).

UGW scanning executed on another set of stringer stiffened composite panels, was compared directly to the results from conventional NDE methods. Amplitude and time features from UGW results were evaluated for wave packets containing symmetric and anti-symmetric wave modes. UGW feature indexes were compared to the conventional UT C-scan results. Time feature (time delay) of symmetric wave mode packets was evaluated to be sensitive to the crushed matrix damage, but insensitive to the disbond damage from stringer flange blunt impact. On the other hand, amplitude feature (RMS of gated signal) of combined symmetric and anti-symmetric wave mode packets estimated disbond damage span and severity along the stringer flange. Time and amplitude feature index values at the center of the impact of a series of impact levels showed that the feature indexes are correlative to the damage severity, because higher impact intensity responded to higher time delay and lower RMS values. Also, impact location was discerned by a dip/spike in the feature index profile caused by less severe damage at the exact impact location than its surrounding area. Crushed matrix damage and disbond damage types from impact were discretely identified from the time and amplitude feature, respectively. Blunt impact damage on the stringer cap was also detected from UGW scanning and showed relative RMS value corresponding to the impact level. However, direct comparison of UGW damage scan results for the cap damage to the conventional NDE results was limited to validate performance of UGW-based cap damage characterization.

Finally, residual strength estimation from UGW test results was investigated for open-hole notched composite coupons and flange impact damaged composite elements from single stringer panels. UGW to residual strength correlation method was first studied at a basic level using open-hole notched composite coupons and promising outputs were observed: UGW amplitude features ratio from a line scan through the center of the damage was reduced corresponding to increasing hole notch sizes. Similarly, flange impact damaged Stringer panel's UGW amplitude feature and residual compressive strength profile plotted versus the impact levels showed a relatively decaying trend, although the test data is scarcely limited (only 4 data points).

Potential of UGW test method was explored for damage scanning on complex composite structures. The main objectives of the research were partially achieved: damage detection and characterization were achieved for stringer stiffened panels, but for impact damage on skin-stringer flange only. Even though damage characteristics were not quantified, detection of damage was achieved on bolted joint composite components (shear tie) from complex composite panels. Nonetheless, UGW test results seem promising for damage detection of more complex structures with continuous waveguides, and quantitative measurements relating to damage characteristics (size and location) should be possible by scrutinizing the features UGW results data of various wave modes.

5.1. Future Research Prospects

Wave propagation through a structure is understood to contain much more information than what is understood, and it certainly does, based on the meaningful information that was interpreted from analyses performed on a fraction of UGW data throughout this research. UGW scanning systems, both non-contact and hybrid systems, obtained quite significant information about damage on composite structures from transmitted UGWs across the damage. However, location of damage could be characterized more precisely by analyzing reflected waves from two transducers system (receiver transducers before and after the stringer). When damage is located at the inlet or outlet of stringer flanges across the wave path, reflected waves will arrive at different times back to the receiver, closer to the excitation source. Also, a hybrid system was tested manually along the stringer on the panel -- a mini-impactor and receiver sensors were moved along the stringer separately referenced to a tape strip ruler. Although experimental results were remarkable, UGW results had minor discrepancies between each scan point. An optimized hybrid scanning system could enhance and minimize test discrepancies, by implementing the system in a robust fixture, and automating the mini-impactor trigger device which could minimize system misalignment from scans along the stringer and signal misalignment from software's amplitude-based data acquisition trigger.

Also, residual strength estimation based on UGW measurements could further be elaborated. Open-hole notch specimens showed great sensitivity to estimate hole notch sizes based on UGW results to correlate to the residual strength, but the parameters that influence the UGW measurements and residual strength relationship are not fully understood. Perhaps, additional FE model simulation could be studied to interrogate the residual strength to UGW features relationship. UGW measurements correlation to evaluate residual strength of different failure modes (compression, shear, or bending) for different damage types (matrix crack, delamination, or fiber breakage from impact damage). If a meaningful relationship of various cases is built, then their relationship could further explore complex composite structures. Finally, the time feature of the UGW signals should be explored for UGW-based residual strength estimation.

References

[1] Kim, Hyonny, Douglas A. Welch, and Keith T. Kedward. "Experimental investigation of high velocity ice impacts on woven carbon/epoxy composite panels." *Composites Part A: Applied Science and Manufacturing,* vol. 34, no. 1, pp. 25-41, 2003

[2] Whisler, Daniel, and Hyonny Kim. "Effect of impactor radius on low-velocity impact damage of glass/epoxy composites." *Journal of composite Materials,* vol. 46, no. 25, pp. 3137-3149, 2012.

[3] Ellison, Andrew, and Hyonny Kim. "Computed tomography informed composite damage state model generation." *Journal of Composite Materials,* vol. 52, no. 25, pp. 3523-3538, 2018.

[4] DeFrancisci, Gabriela K."High energy wide area blunt impact on composite aircraft structures." PhD Dissertation, University of California, San Diego, 2013.

[5] Ilcewicz, Larry. "Composite damage tolerance and maintenance safety issues." *FAA Damage Tolerance and Maintenance Workshop,* Rosemont, IL. 2006.

[6] Chen, Zhi Ming. "Experimental and Numerical Investigation of Wide Area Blunt Impact Damage to Composite Aircraft Structures." PhD Dissertation., University of California, San Diego, 2015.

[7] Federal Aviation Administration, "Composite aircraft structure." Advisory Circular (AC) 20-107B, *Change 1,* 2010.

[8] Rayleigh, Lord. "On waves propagated along the plane surface of an elastic solid." *Proceedings of the London Mathematical Society,* vol. s1-17, no. 1, pp. 4-11, 1885.

[9] Lamb, Horace. "On waves in an elastic plate." *Proceedings of the Royal Society of London. Series A,* vol. 93, no. 648, pp. 114-12, 1917.

[10] Rose, Joseph L. *Ultrasonic guided waves in solid media*. Cambridge university press, 2014.

[11] Su, Zhongqing, Lin Ye, and Ye Lu. "Guided Lamb waves for identification of damage in composite structures: A review." *Journal of Sound and Vibration,* vol. 295, no. 3-5, pp. 753-780, 2006.

[12] Raghavan, Ajay. "Review of Guided-wave Structural Health Monitoring." *The Shock and Vibration Digest,* vol. 39, no. 2, pp. 91-114, 2007.

[13] Worlton, D. C. "Experimental confirmation of Lamb waves at megacycle frequencies." *Journal of Applied Physics,* vol. 32, no. 6, pp. 967-971, 1961

[14] Alleyne, David N., and Peter Cawley. "The interaction of Lamb waves with defects." *IEEE Transactions on Ultrasonics, Ferroelectrics, and Frequency Control,* vol. 39, no. 3, pp. 381-397, 1992.

[15] Tang, Bruce, and Henneke, E.G., “Lamb wave monitoring of axial stiffness reduction of laminated composite plates.” *Materials Evaluation,* vol. 47, no. 8, pp. 928-933, 1989.

[16] Kessler, Seth S., S. Mark Spearing, and Constantinos Soutis. "Damage detection in composite materials using Lamb wave methods." *Smart Materials and Structures,* vol. 11, no. 2, pp. 269, 2002.

[17] Kaczmarek, H. "Lamb wave interaction with impact-induced damage in aircraft composite: use of the A0 mode excited by air-coupled transducer." *Journal of Composite Materials,* vol. 37, no. 3, pp. 217-232, 2003.

[18] Cho, Younho. "Estimation of ultrasonic guided wave mode conversion in a plate with thickness variation." *IEEE Transactions on Ultrasonics, Ferroelectrics, and Frequency Control,* vol. 47, no. 3, pp. 591-603, 2000.

[19] Yang, Jinkyu, and Fu-Kuo Chang. "Detection of bolt loosening in C–C composite thermal protection panels: I. Diagnostic principle." *Smart Materials and Structures,* vol. 15, no. 2, pp. 581-590, 2006.

[20] Bao, Jingjing, and Victor Giurgiutiu. "Effects of fastener load on wave propagation through lap joint." *Health Monitoring of Structural and Biological Systems 2013,* vol. 8695, pp. 86952-1-12, 2013.

[21] Waddoups, Mo E., Jo R. Eisenmann, and B. Eo Kaminski. "Macroscopic fracture mechanics of advanced composite materials." *Journal of Composite Materials,* vol. 5, no. 4, pp. 446-454, 1971.

[22] Mar, James W., and Kuen Y. Lin. "Fracture of boron/aluminum composites with discontinuities." *Journal of Composite Materials,* vol. 11, no. 4, pp. 405-421, 1977.

[23] Caprino, Giancarlo. "On the prediction of residual strength for notched laminates." *Journal of Materials Science*, vol. 18, no. 8, pp. 2269-2273, 1983.

[24] Caprino, Giancarlo. "Residual strength prediction of impacted CFRP laminates." *Journal of Composite Materials,* vol. 18, no. 6, pp. 508-518, 1984.

[25] Stone, D. E. W., and B. Clarke. "Ultrasonic attenuation as a measure of void content in carbon-fibre reinforced plastics." *Non-Destructive Testing,* vol. 8, no. 3, pp. 137-145, 1975.

[26] Jeong, H. "Effects of voids on the mechanical strength and ultrasonic attenuation of laminated composites." *Journal of composite materials,* vol. 31, no. 3, pp.276-292, 1997.

[27] Capriotti, Margherita, Hyungsuk E. Kim, Francesco Lanza di Scalea, and Hyonny Kim. "Non-Destructive inspection of impact damage in composite aircraft panels by ultrasonic guided waves and statistical processing." *Materials*, vol. 10, no. 6, pp. 616, 2017.

[28] Halvorsen, William G., and David L. Brown. "Impulse technique for structural frequency response testing." *Sound and Vibration*, vol. 11, no. 11, pp. 8-21, 1977.

[29] Thomas, Frank P., and Zhao Yi. “Torque Limit for Composites Joined with Mechanical Fasteners.” *46th AIAA/ASME/ASCE/AHS/ASC Structures, Structural Dynamics and Materials Conference*, pp. 2351, 2005.

[30] Ellison, Andrew C. “Segmentation of X-ray CT and Ultrasonic Scans of Impacted Composite Structures for Damage State Interpretation and Model Generation." PhD Dissertation , University of California, San Diego, 2020.

[31] Jacovitti, Giovanni, and Gaetano Scarano, "Discrete time techniques for time delay estimation." *IEEE Transactions on Signal Processing*, vol. 41, no. 2, pp. 525-533, 1993.

[32] Rizzo, Piervincenzo, and Francesco Lanza di Scalea, "Feature extraction for defect detection in strands by guided ultrasonic waves." *Structural Health Monitoring*, vol. 5, no. 3, pp. 297-308, 2006.

[33] ABAQUS. ABAQUS Analysis User’s Manual, Version 6.13, *Dassault Systemes Simulia Corp*, 2013.

[34] Yang, Chunhui, Lin Ye, Zhongqing Su, and Michael Bannister. "Some aspects of numerical simulation for Lamb wave propagation in composite laminates." *Composite Structures*, vol. 75, no. 1-4, pp. 267-275, 2006.

[35] Capriotti, Margherita. “Elastic and Thermal Wave Propagation based Techniques for Structural Integrity Assessment.” PhD Dissertation , University of California, San Diego, 2019.

Appendix A. Finite Element Model Analysis

A.1. C-frame Abaqus Model

Finite element model was analyzed to understand the behavior of asymmetric UGW on C-frame components from HEWABI Frame panels. C-frame model was designed based on the cross-section area and material properties from DeFrancisci's dissertation [4]. For guided wave simulation, central-difference time integration rule was accounted for to determine time increment and mesh size for the center frequency of the simulated excitation (Equations (4.2.1.1) and (4.2.1.2)). C-frame was partitioned to generate slit damage on its section and to generate a ply offset. Various ply angle offset was not examined (see Figure 2.2.2.4.b), but ply offset on a simple composite plate was executed instead to reduce the computational cost. The model was further explored for possible damage detection at the UGW test frequency, 50 kHz, which propagated strongly through bolted joint frame components. UGW simulation results from chirp excitation (50-500 kHz) showed very good detection capability of C-frame flange damage at 50 kHz. Dynamic explicit analysis was used to simulate guided wave propagation through the C-frame with settings and results shown in the following figures:

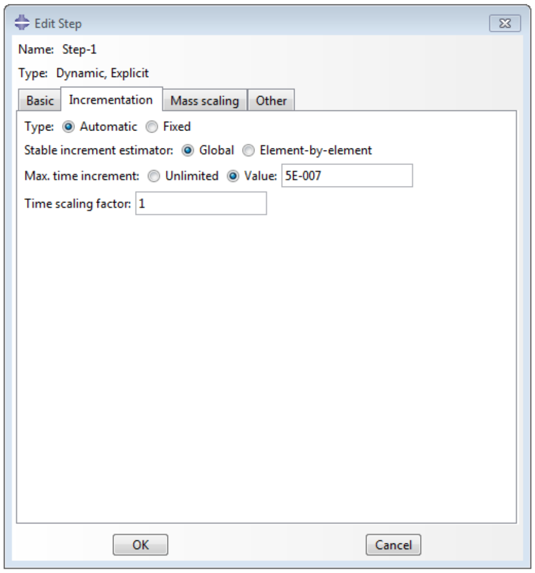

Edit Step

Name: Step-1

Type: Dynamic, Explicit

Type: ● Automatic ○ Fixed

Stable increment estimator: ● Global ○ Element-by-element

Max. time increment: ○ Unlimited ● Value: 5E-007

Time scaling factor: 1

Figure A.1.1. Dynamic, Explicit Step with max time increment at 150 kHz simulation

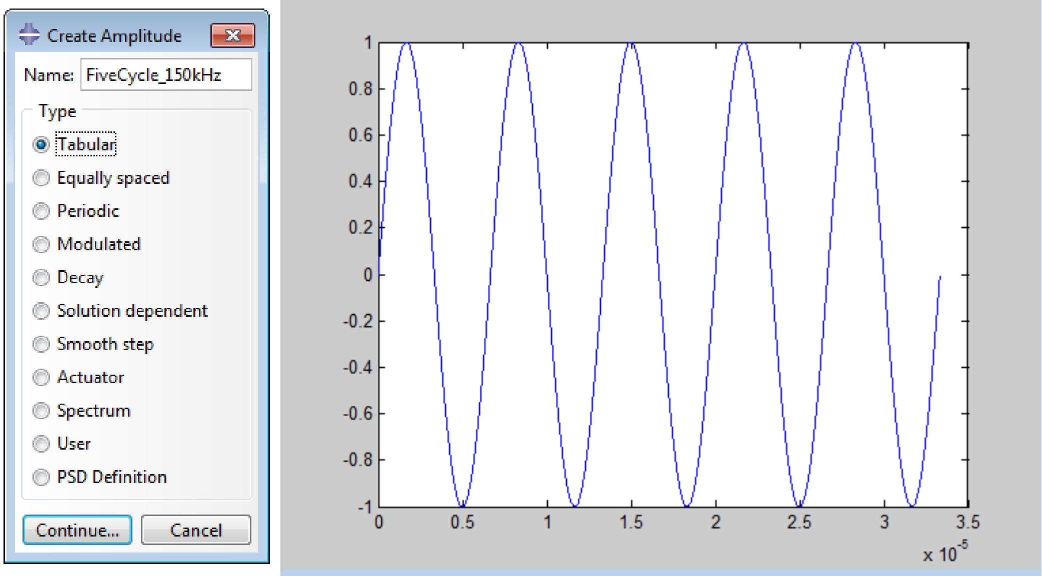

Create Amplitude

Name: FiveCycle_150kHz

Type

● Tabular
○ Equally spaced
○ Periodic
○ Modulated
○ Decay
○ Solution dependent
○ Smooth step
○ Actuator
○ Spectrum
○ User
○ PSD Definition

Figure A.1.2. Five cycle 150 kHz sine waves point load assigned using (left) tabular amplitude with (right) five cycle sine waves data generated from MATLAB

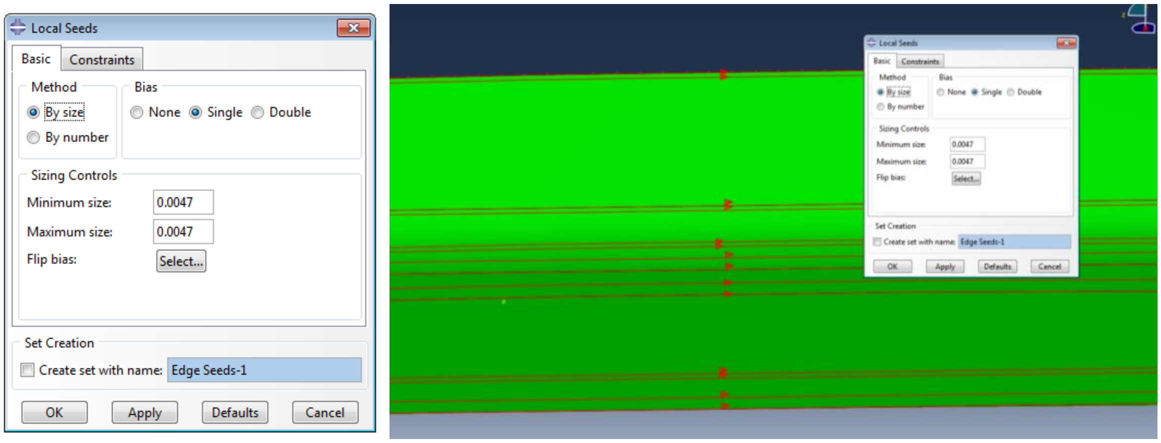

Method
● By size
○ By number

Bias
○ None ● Single ○ Double

Sizing Controls
Minimum size: 0.0047
Maximum size: 0.0047
Flip bias: Select...

Set Creation
☐ Create set with name: Edge Seeds-1

Figure A.1.3. Seed mesh size evaluated for 150 kHz frequency simulation input gathered from MATLAB generated five cycle sine waves bias direction towards center of the C-frame

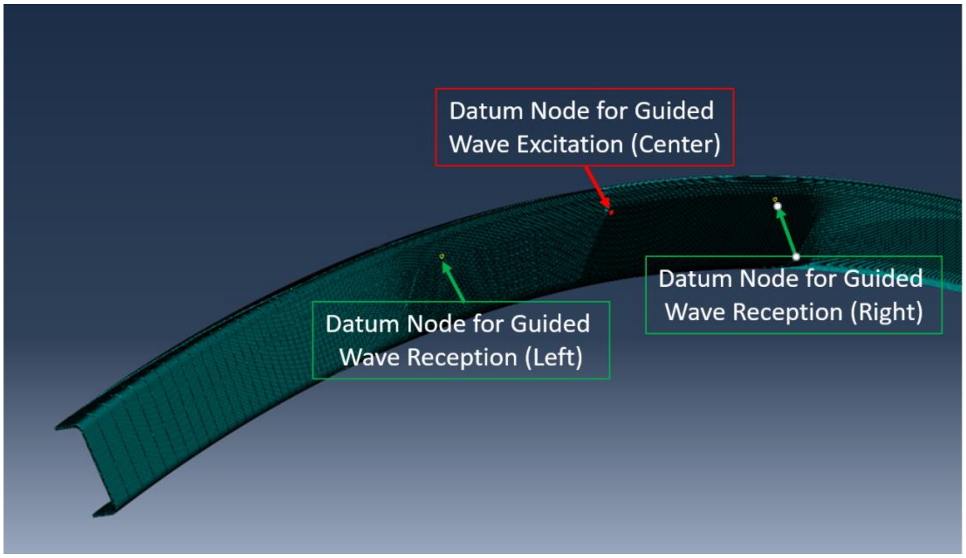

Figure A.1.4. Node sets to excite and receive UGW

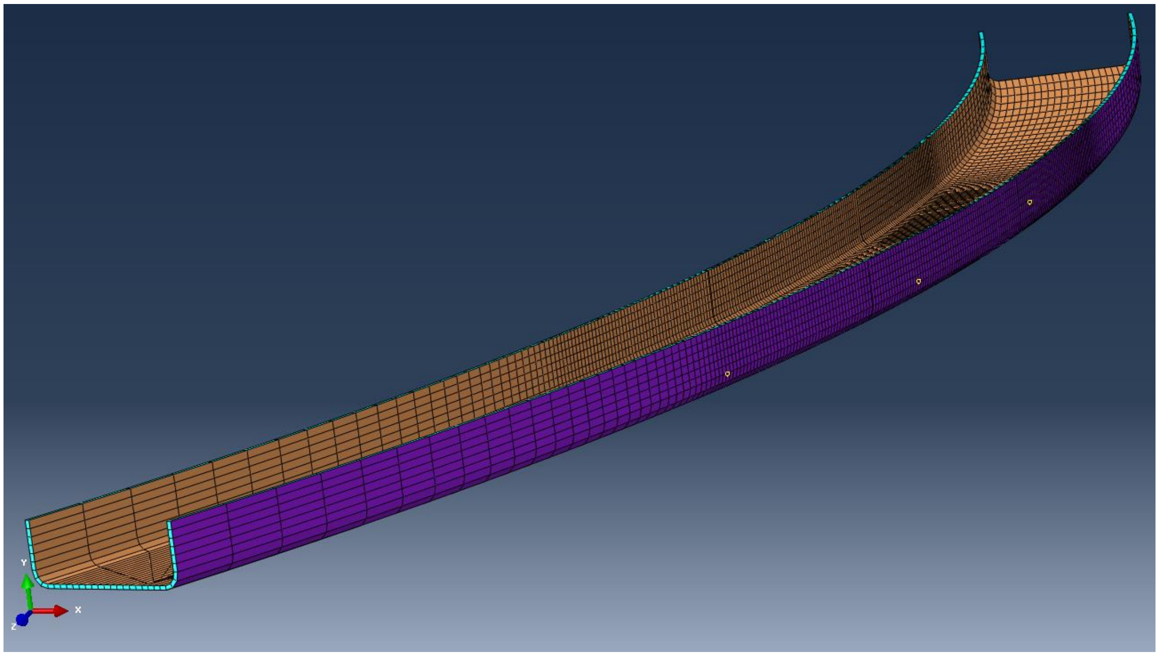

Figure A.1.5. Uniformly assigned stacking direction

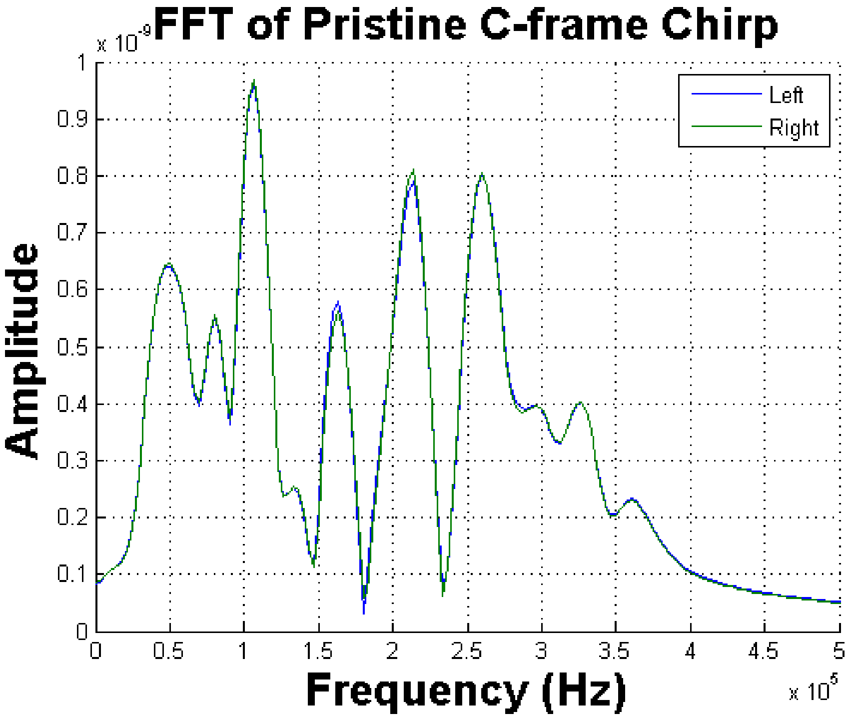

Figure A.1.6. Frequency response from C-frame model without damage

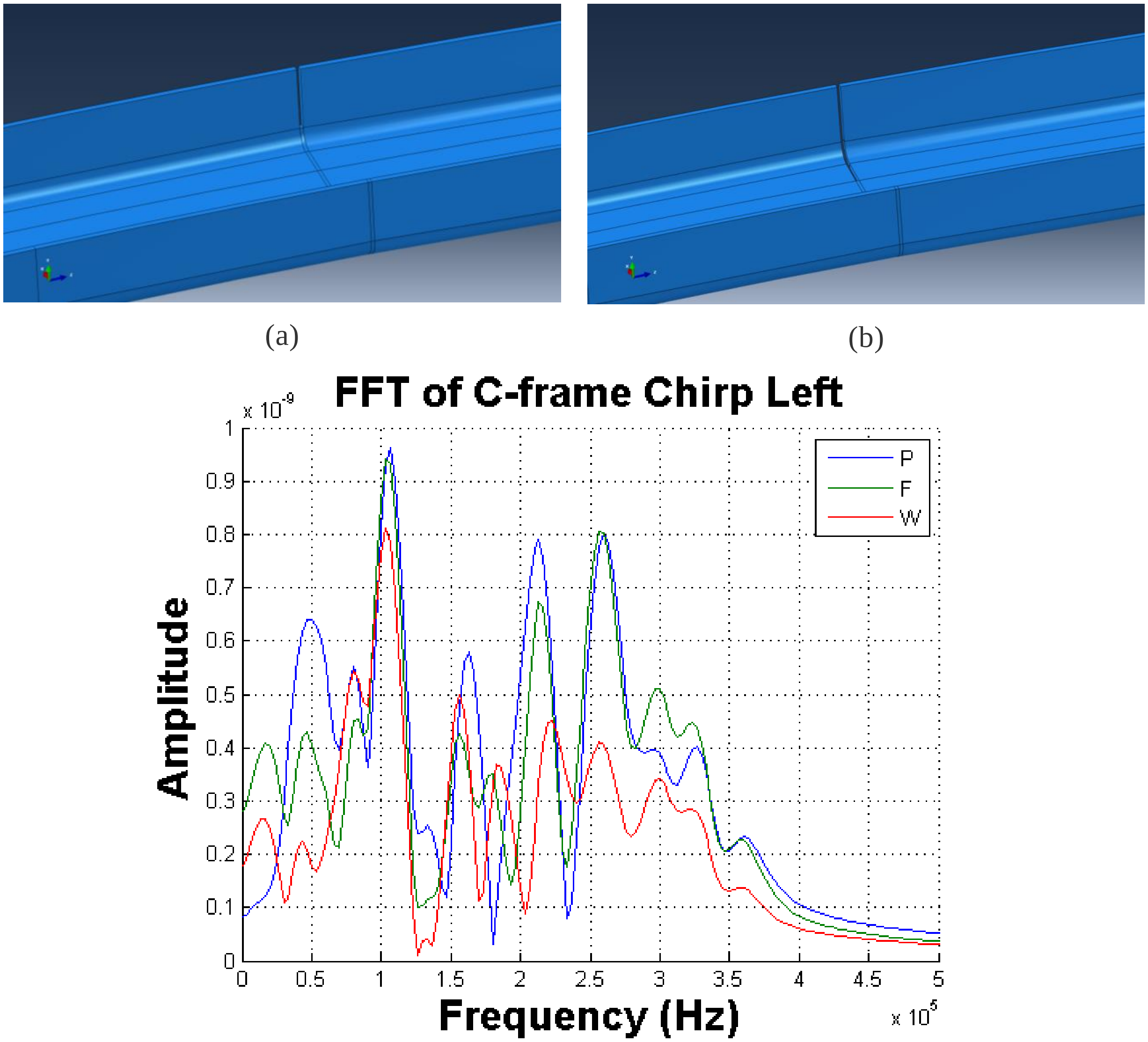

(a) (b)

(c)

Figure A.1.7. Frequency response from C-frame model with crack-like damage: (a) flange damage, (b) flange+partial web damage, and (c) frequency response results (P-pristine, F-flange only, and W-flange+partial web damage)

A.1.1. Angle Offset on C-frame Abaqus Model

In order to understand asymmetric guided wave propagation examined through C-frame via experiments, single ply offset of splice joint fabric patch was simulated. All simulation setting was the same as the previous section, A.1. Displacement result from single partitioned region ply offset result is as seen in Figure 2.2.2.5. Angle offset simulation was further explored on a simple plate.

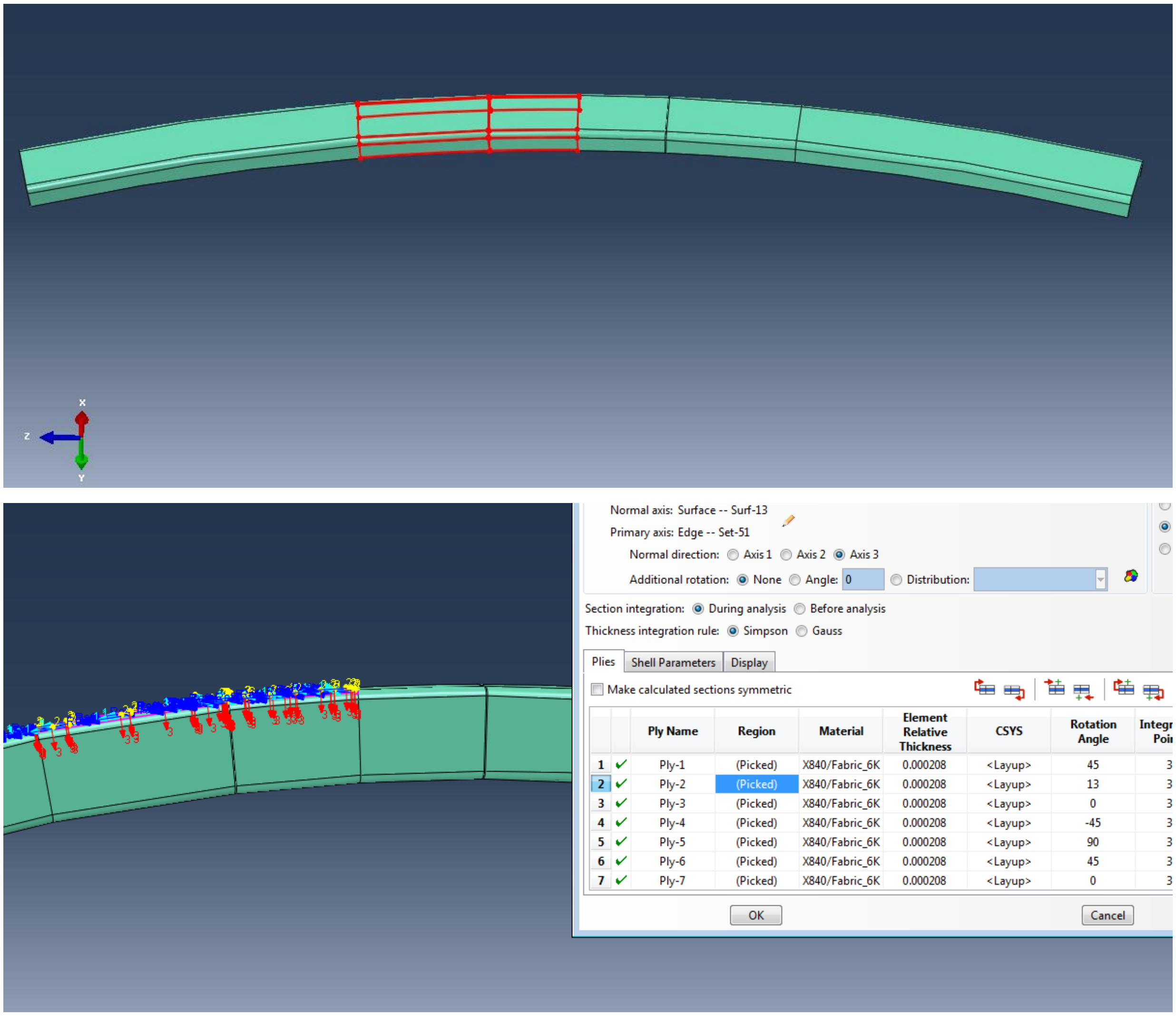

Normal axis: Surface -- Surf-13

Primary axis: Edge -- Set-51

Normal direction: ○ Axis 1 ○ Axis 2 ● Axis 3

Additional rotation: ● None ○ Angle: 0 ○ Distribution:

Section integration: ● During analysis ○ Before analysis

Thickness integration rule: ● Simpson ○ Gauss

☐ Make calculated sections symmetric

		Ply Name	Region	Material	Element Relative Thickness	CSYS	Rotation Angle	Integr Poi
1	✓	Ply-1	(Picked)	X840/Fabric_6K	0.000208	<Layup>	45	3
2	✓	Ply-2	(Picked)	X840/Fabric_6K	0.000208	<Layup>	13	3
3	✓	Ply-3	(Picked)	X840/Fabric_6K	0.000208	<Layup>	0	3
4	✓	Ply-4	(Picked)	X840/Fabric_6K	0.000208	<Layup>	-45	3
5	✓	Ply-5	(Picked)	X840/Fabric_6K	0.000208	<Layup>	90	3
6	✓	Ply-6	(Picked)	X840/Fabric_6K	0.000208	<Layup>	45	3
7	✓	Ply-7	(Picked)	X840/Fabric_6K	0.000208	<Layup>	0	3

Figure A.1.1.1. Second ply was changed from 0 to13 degree ply angle at a partitioned region (results shown in Figure 2.2.2.5)

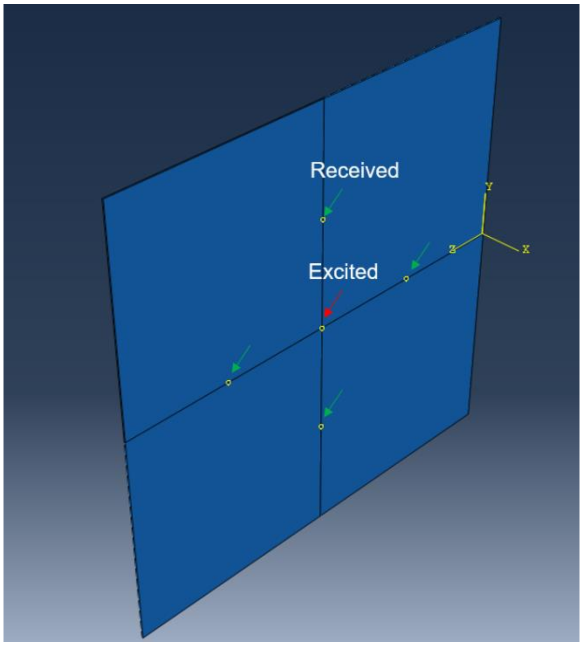

Figure A.1.1.2. Composite laminated plate of the same material as C-frame

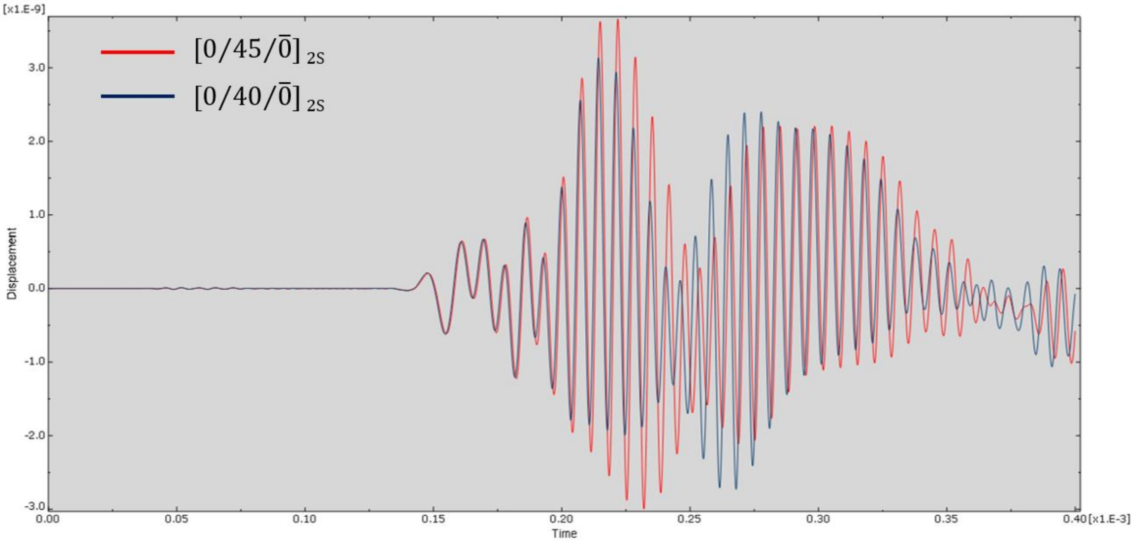

Figure A.1.1.3. Composite laminated plate compared for $[0/45/\bar{0}]_{2S}$ and $[0/40/\bar{0}]_{2S}$

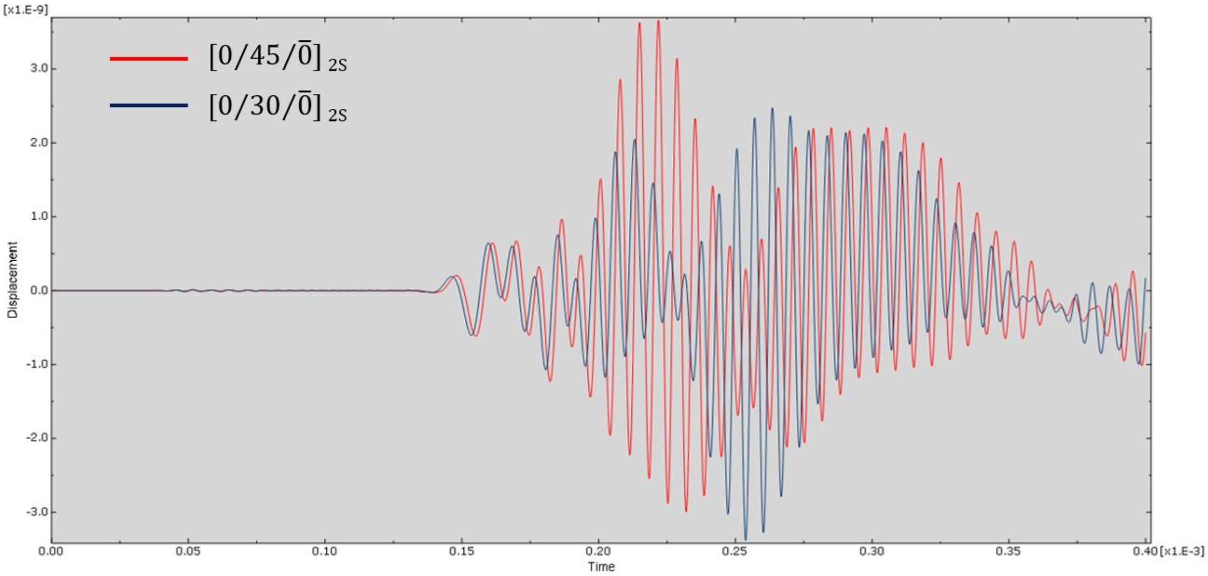

Figure A.1.1.4. Composite laminated plate compared for $[0/45/\bar{0}]_{2S}$ and $[0/30/\bar{0}]_{2S}$

A.2. Mini-Impactor Model

A mini-impactor was model simulated before it was manufactured to determine a suitable design that fits the experimental need. Various tip designs were projected to the aluminum plate at a set velocity of 6.4 m/s.

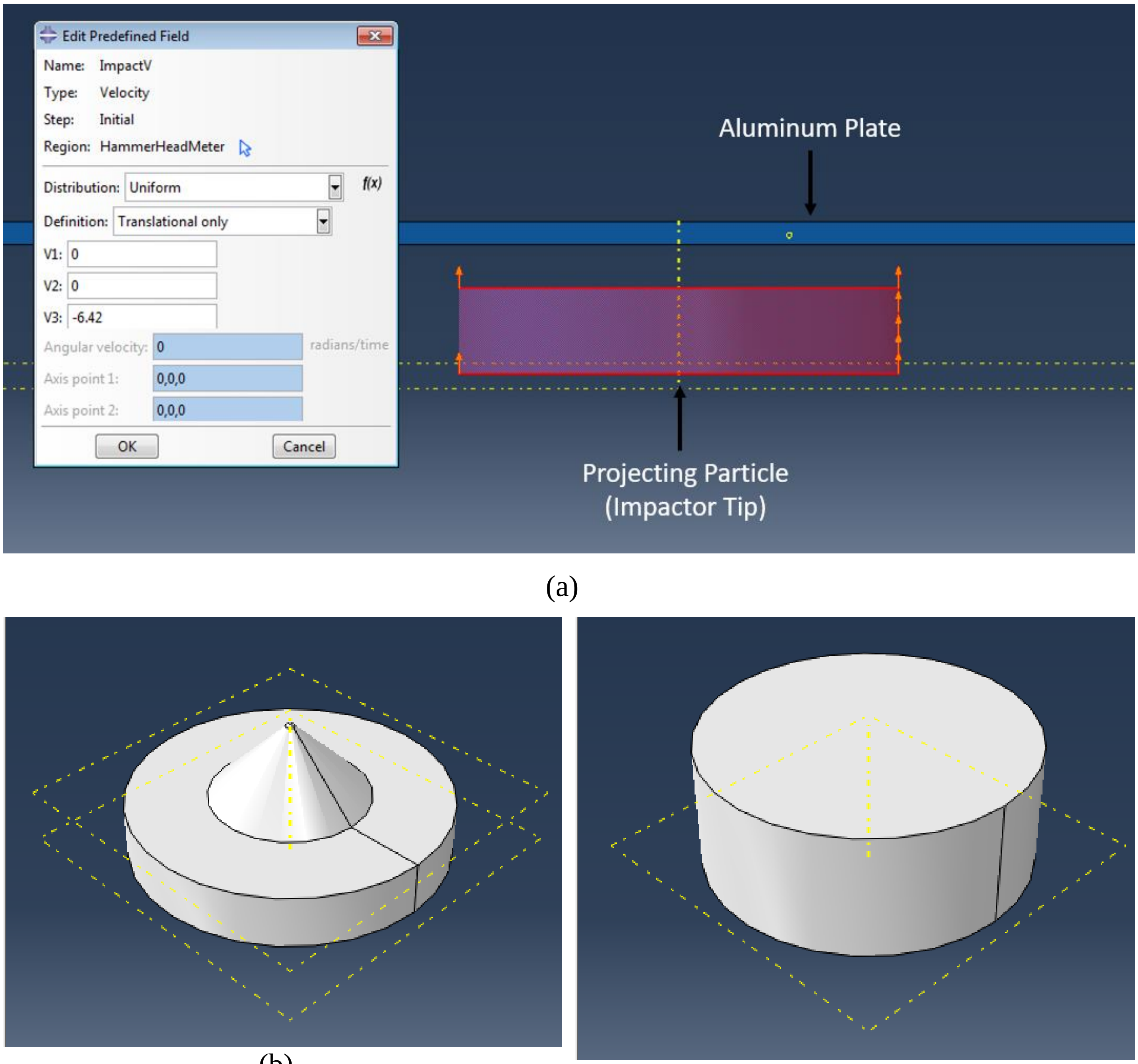

Edit Predefined Field

Name: ImpactV
Type: Velocity
Step: Initial
Region: HammerHeadMeter

Distribution: Uniform
Definition: Translational only
V1: 0
V2: 0
V3: -6.42
Angular velocity: 0 radians/time
Axis point 1: 0,0,0
Axis point 2: 0,0,0

(a)

(b)

(c)

Figure A.2.1. Impact simulation on (a) an aluminum plate for various impactor shapes: disc impactor of (b) 1 mm depth and 5 mm diameter with a cone tip and (c) 5 mm depth and diameter with a flat face

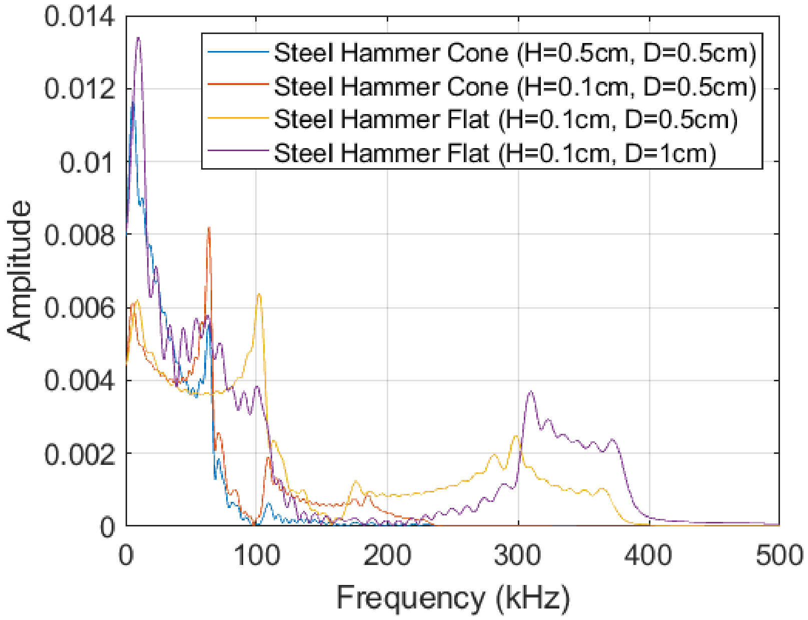

Figure A.2.2. Impact simulation frequency response of various impactor shapes

Appendix B. Miscellaneous Experiments

B.1. 3D-printed R15S Transducer Hold-Down

R15S transducer hold-down was designed and 3D-printed from SolidWorks designed model. Magnetic transducer hold-downs from Mistras were first used for experimental tests from the outer skin. However, composite components did not always have ferromagnetic parts on the structure, so the 3D-printer was used to manufacture a hold-down for general purposes. Hold-downs with neoprene (hold down inserts to apply pressure on the transducer) and 3M VHB tapes (affix hold down firmly onto the specimen) were working most consistently compared to other inserts (aluminum spring, polyurethane or natural gum foam) and to air-suction cups to fix the hold-downs, respectively.

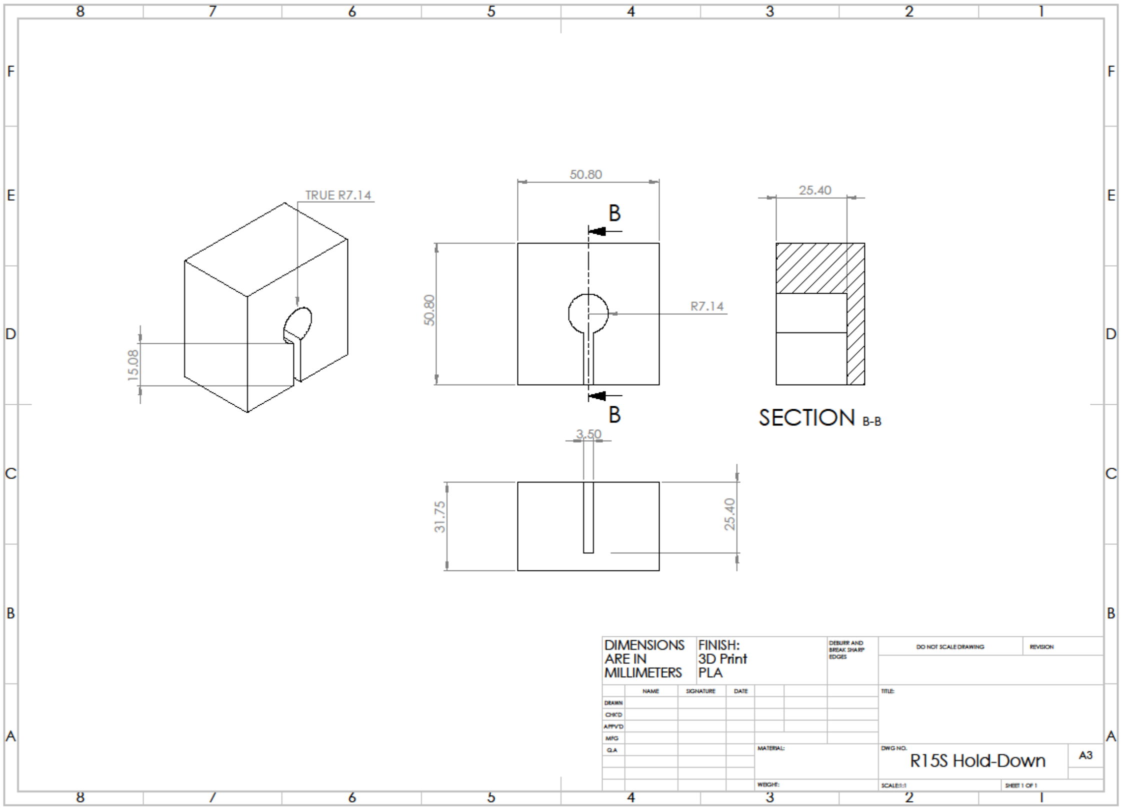

Figure B.1.1. R15S transducer hold-down SolidWorks drawing

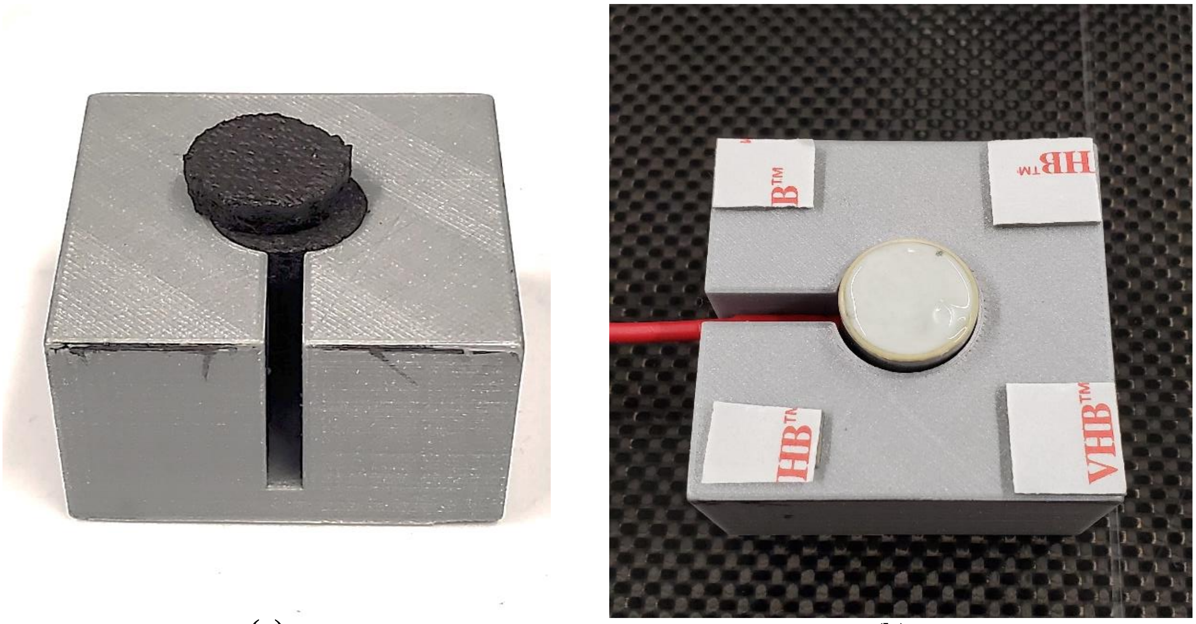

(a) (b)

Figure B.1.2. 3D-printed hold-down with (a) neoprene fill and (b) VHB double-sided tape and gel applied on the R15S sensor

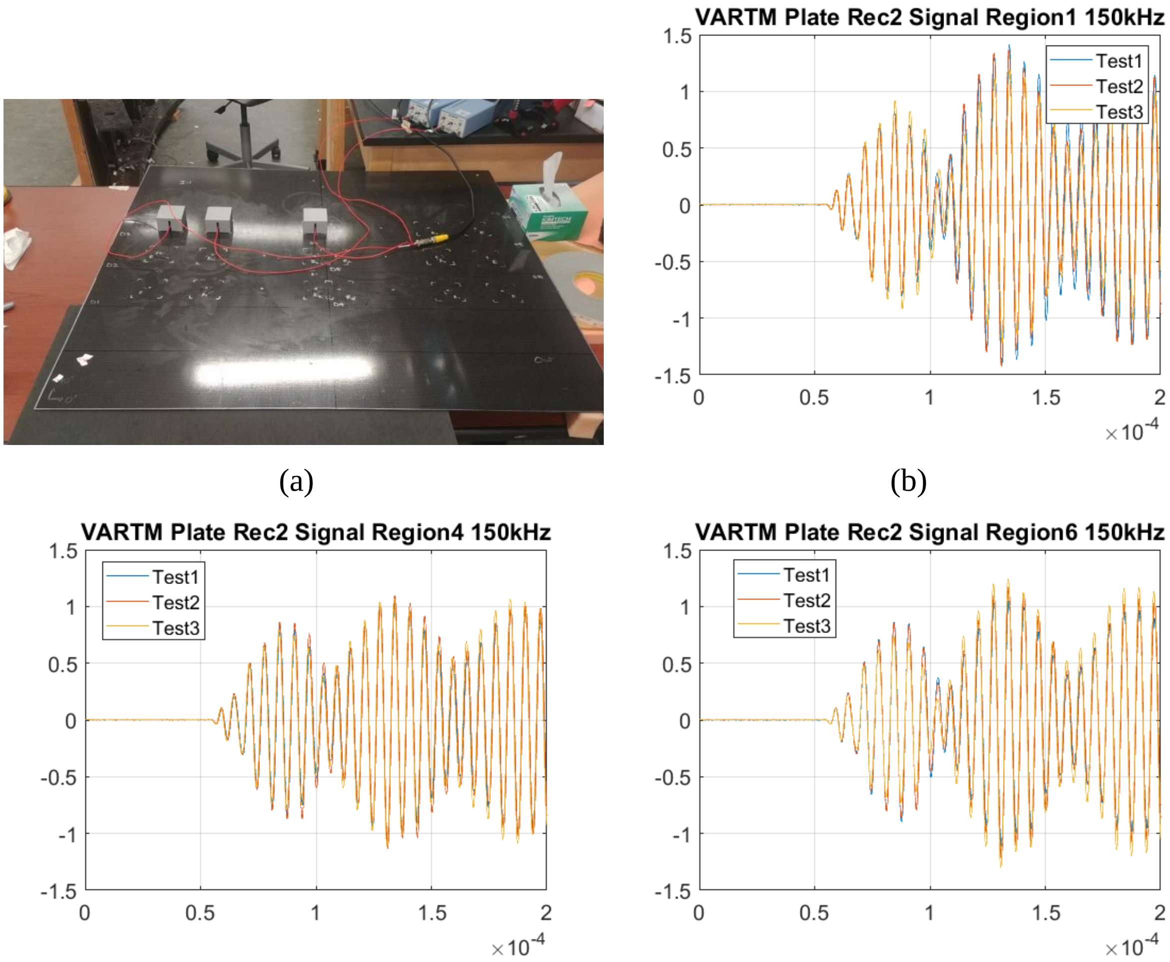

(a) (b)

(c) (d)

Figure B.1.3. Baseline data from three repeated tests (actuator and receiver transducers were completely removed from the composite plate for each test): (a) test setup, and repeated tests on (b) region 1, (c) region 4, and (d) region 6

B.2. Mini-Impactor

A mini-impactor was fabricated with an aluminum tip and a composite strip bonded together from epoxy. For the first batch of mini-impactors, a thin aluminum sheet (white color-coded shim from McMaster-Carr) was snipped into approximate sizes of 1 mm^2, 2 mm^2 and 3 mm^2 square pieces to serve as the aluminum tips. The first batch of composite strips were fabricated from unidirectional dry fibers that did not have a label of the material. A small plate of $[0]_8$ ply 127 x 127 mm was fabricated from a wet-layup technique with Poly Epoxy. The cured laminated composite plate was 0.56 mm in thickness and was trimmed into smaller 6.35 x 100 mm composite strips. Then the aluminum tips and composite strips were lightly sanded prior to bonding. Poly Epoxy was used to bond the tip and the strip together, and the impacting side of the tip surface was taped prior to applying epoxy to ensure clean surface finish from bonding. The second batch of mini-impactors were fabricated with the same process, but with T800/3900 prepreg and a thinner impactor tip (brown color-coded shim from McMaster-Carr).

Mini-impactors' frequency response studies have been performed on aluminum, composite, rubber, and steel specimen. And high-speed camera motion response was observed for mini-impactors' impact contact duration, double impacts and more. High-speed camera observation showed that the thin aluminum tip (0.2 mm) allowed the composite strip to contact the excited aluminum plate. Also, true contact duration may require higher frames/sec capture, but approximately was between 11 and 33 µs. Results from impacting various specimen show hardness of the specimen proportionally determines actuated frequency band.

Table B.2.1: First Batch Mini-Impactor Frequency Response Study Summary

Mini-Impactor (First Batch)	Target Cut Size of the Tip [mm x mm]	Tip thickness [mm]	Tip Mass [mg]	Resonance Frequency [kHz]
1	1 x 1		4.8	42
2			5.3	75
3			5.1	52
4			4.4	68
5	2 x 2		17.8	68
6			17.6	73
7			15.8	58
8	3 x 3		28.6	64
9			30.6	67
10			46.0	68

Table B.2.2: Second Batch Mini-Impactor Impact Response Study Summary

Mini-Impactor (Second Batch)	Tip thickness [mm]	Tip Area [mm x mm]		Contact Duration from High-Speed Camera [μs]
1	0.2	4.14	4.48	11
2	0.52	3.27	4.32	33
3	0.2	4.16	4.67	-
4	0.54	3.04	3.61	-
5	0.51	3.05	2.75	-
6	0.21	2.76	2.81	-
7	0.18	2.11	3.03	-

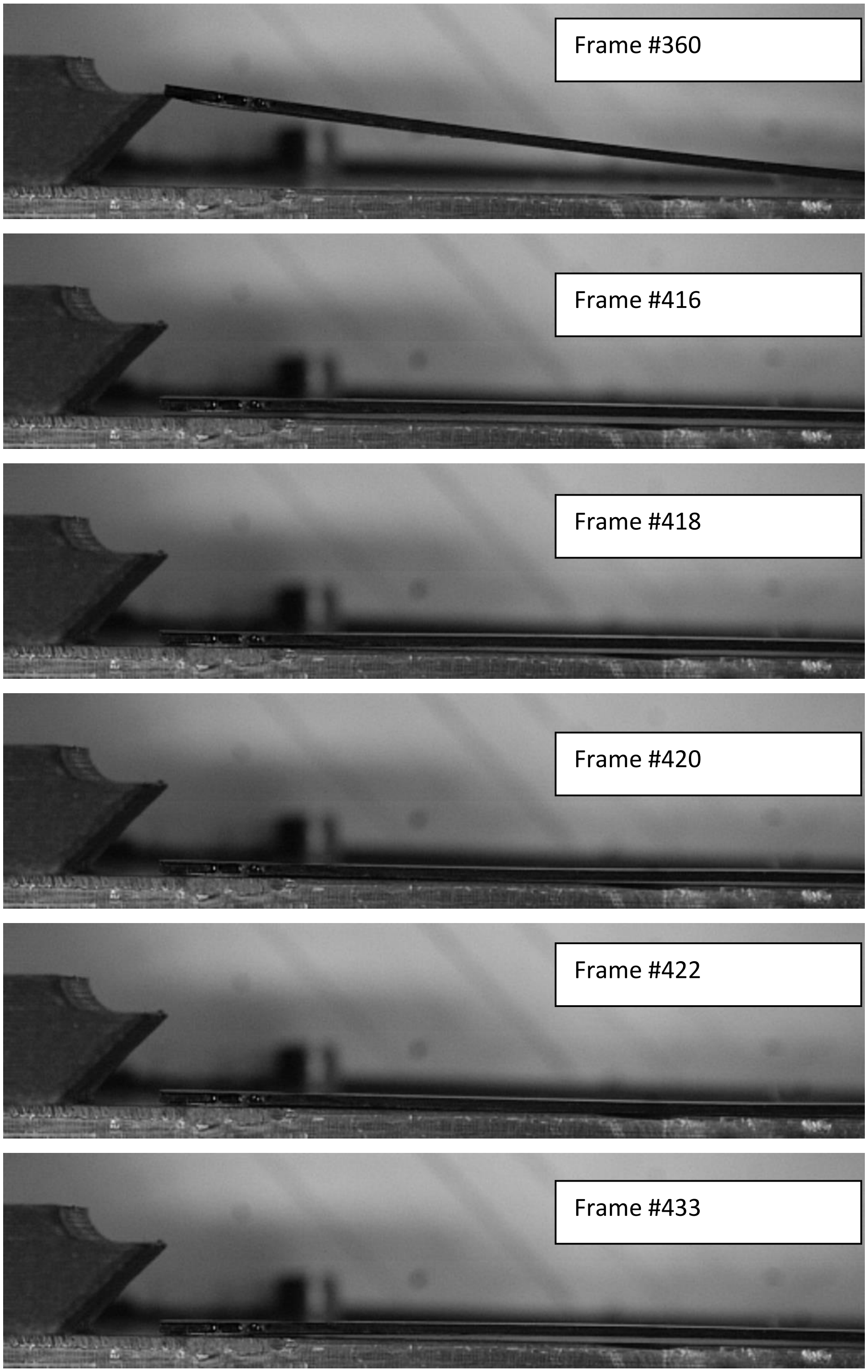

Figure B.2.1. Physical response observation of the mini-impactor with 0.2 mm thickness tip (512 x 128 pixel resolution @ 25 μs/frame) - composite strip touching the aluminum plate

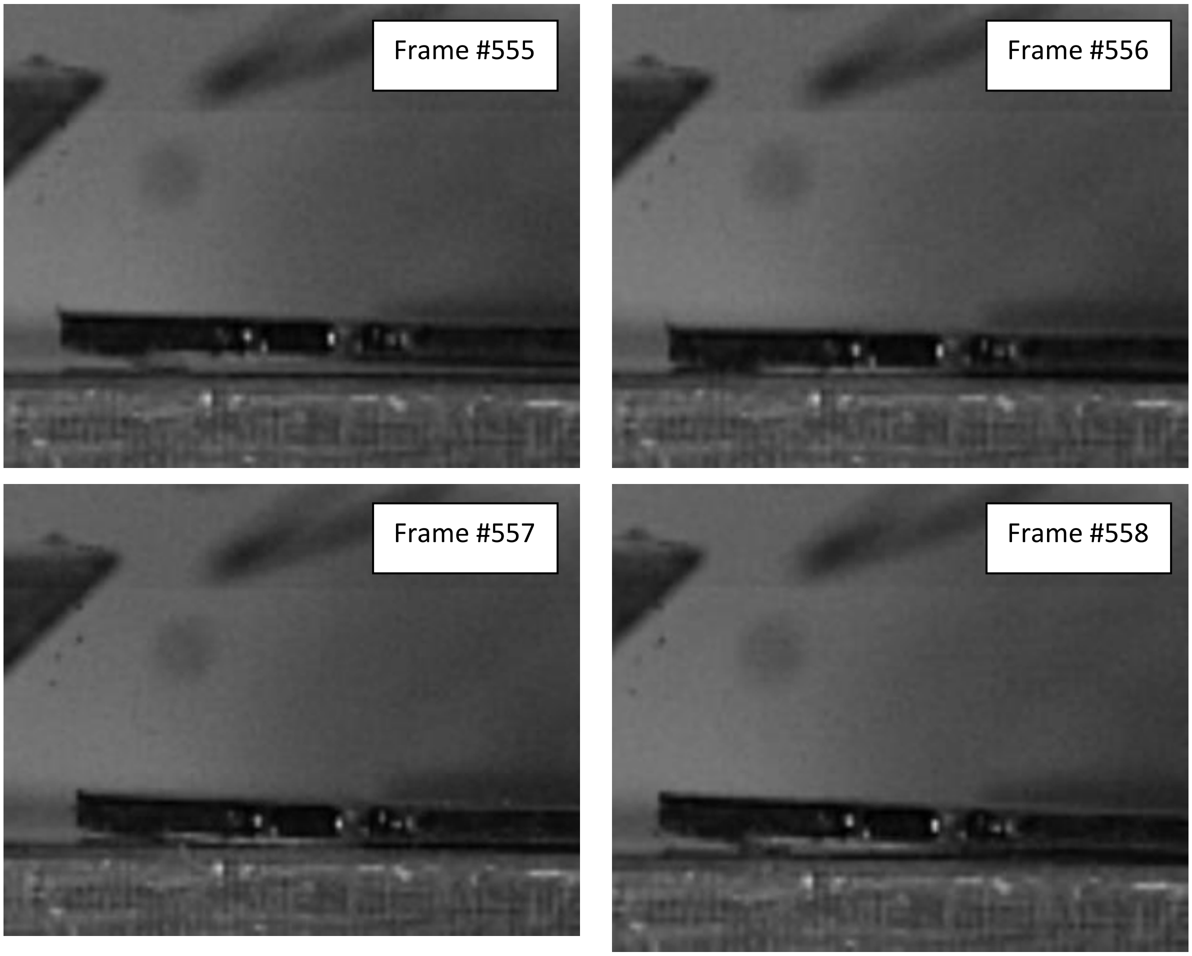

Figure B.2.2. Physical response observation of the mini-impactor with 0.2 mm thickness tip (128 x 128 pixel resolution @ 11 μs/frame)

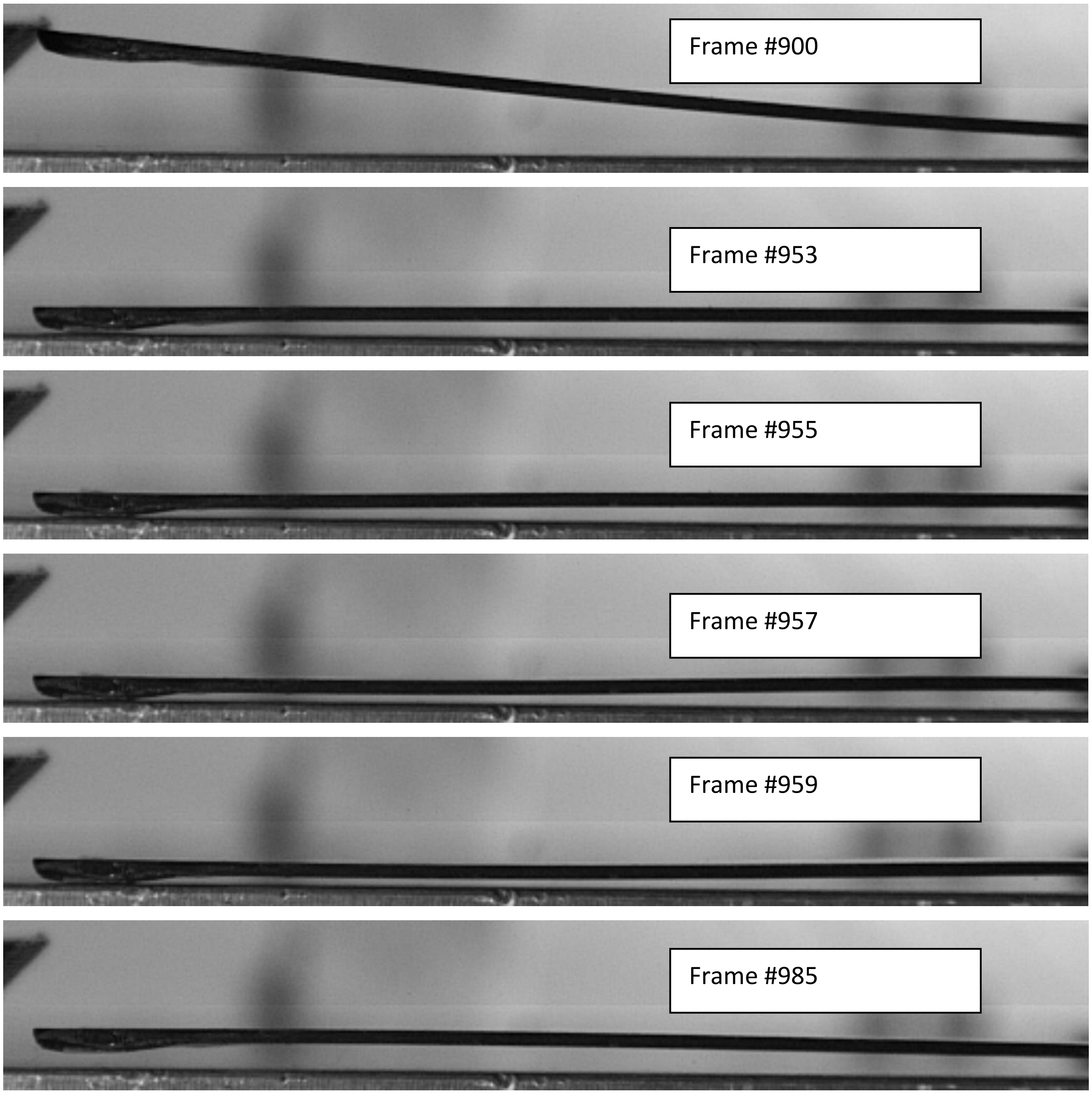

Figure B.2.3. Physical response observation of the mini-impactor with 0.5 mm thickness tip (512 x 80 pixel resolution @ 18 μs/frame) - composite strip touching the aluminum plate

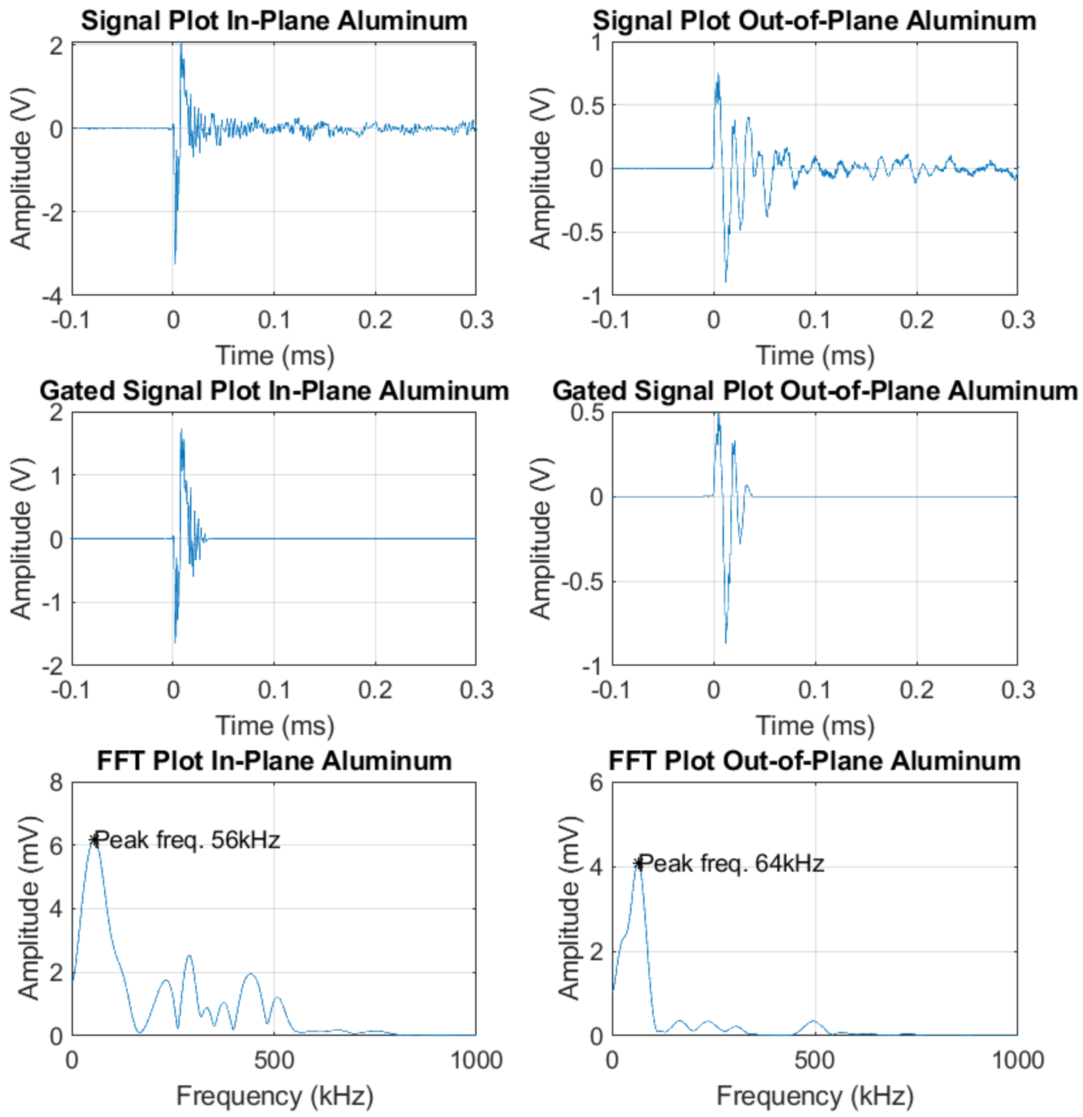

Figure B.2.4. Response on aluminum plate with the mini-Impactor with 0.5 mm thickness tip

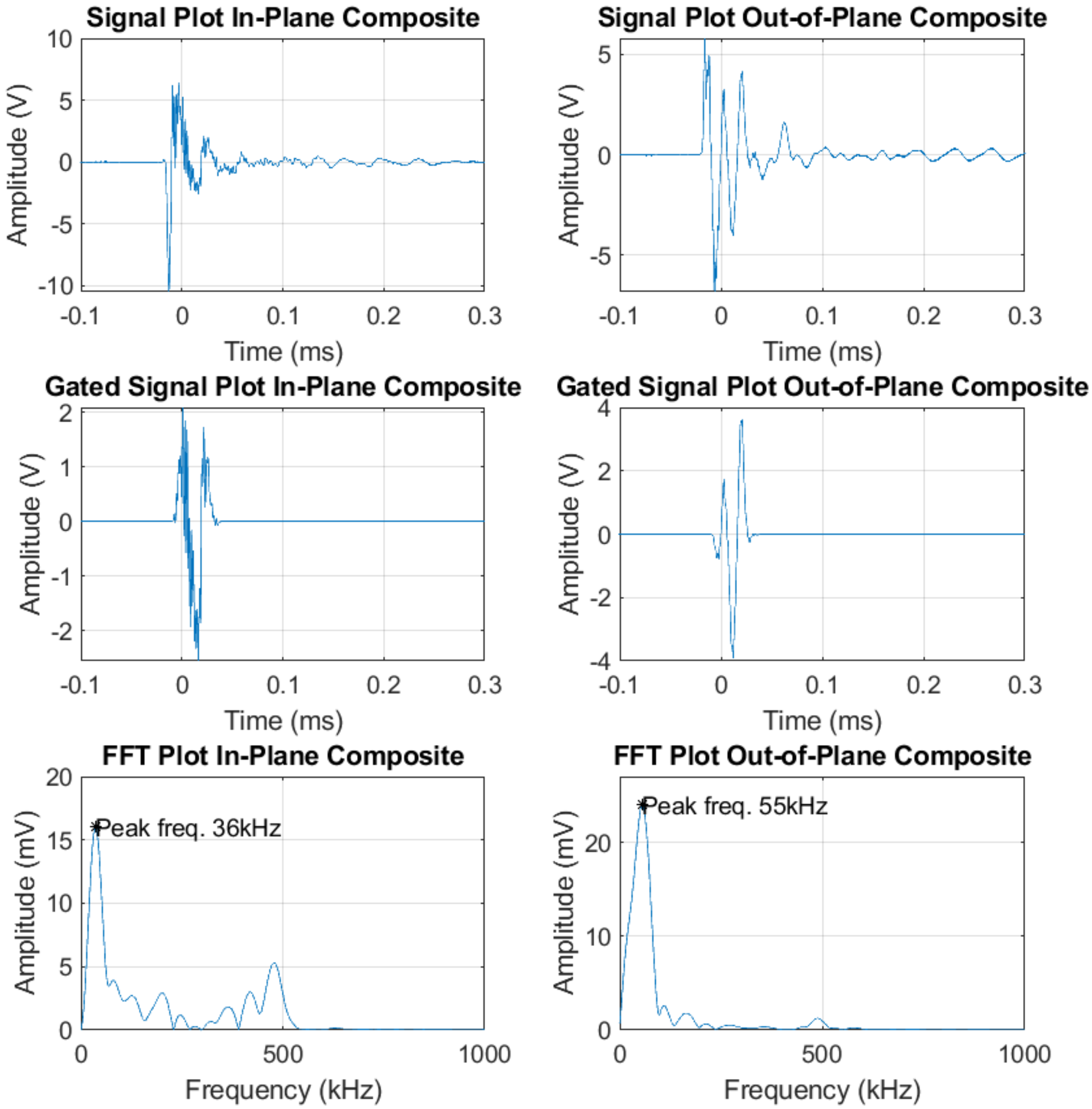

Figure B.2.5. Response on composite plate with the mini-Impactor with 0.5 mm thickness tip

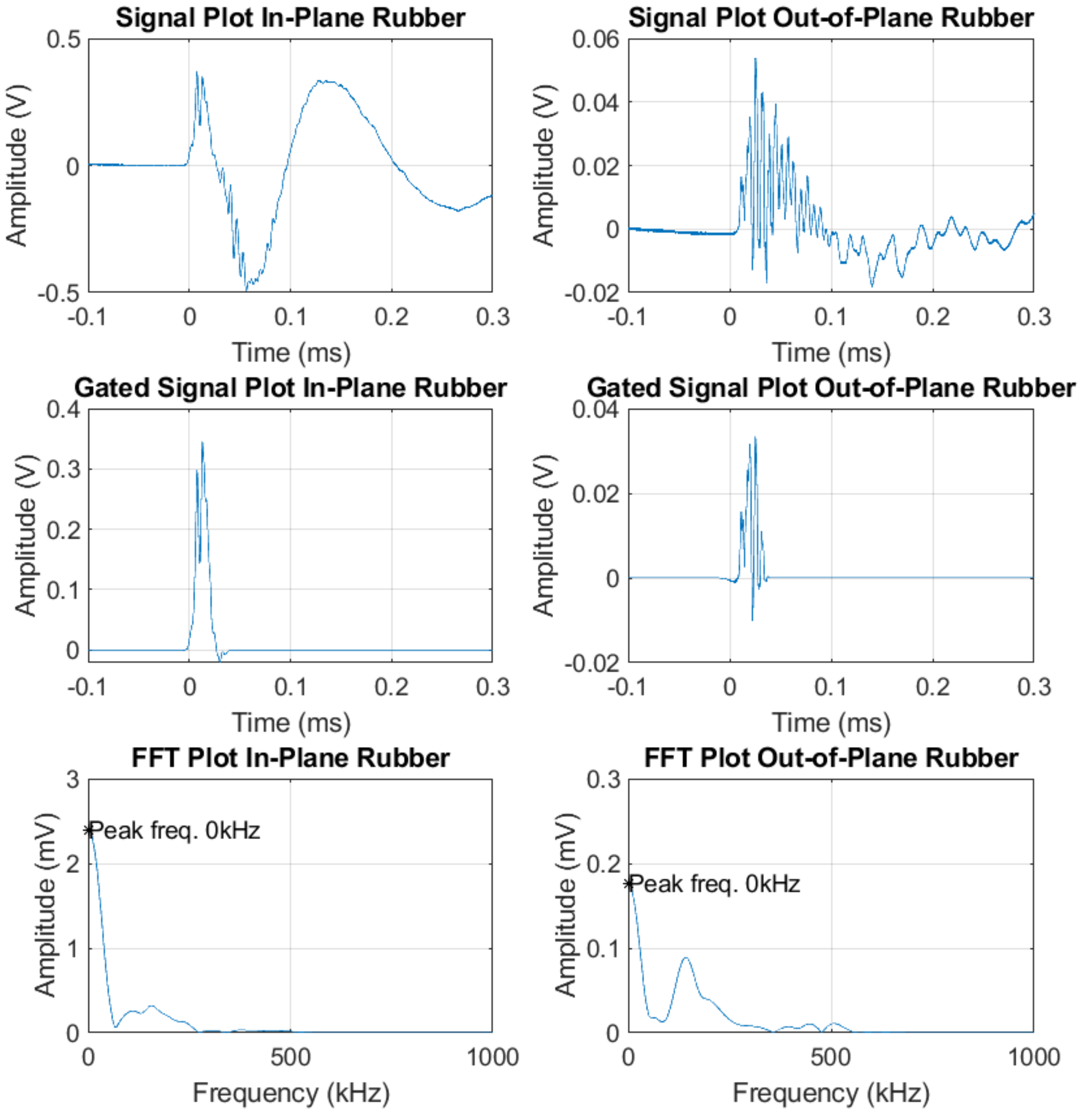

Figure B.2.6. Response on rubber plate with the mini-Impactor with 0.5 mm thickness tip

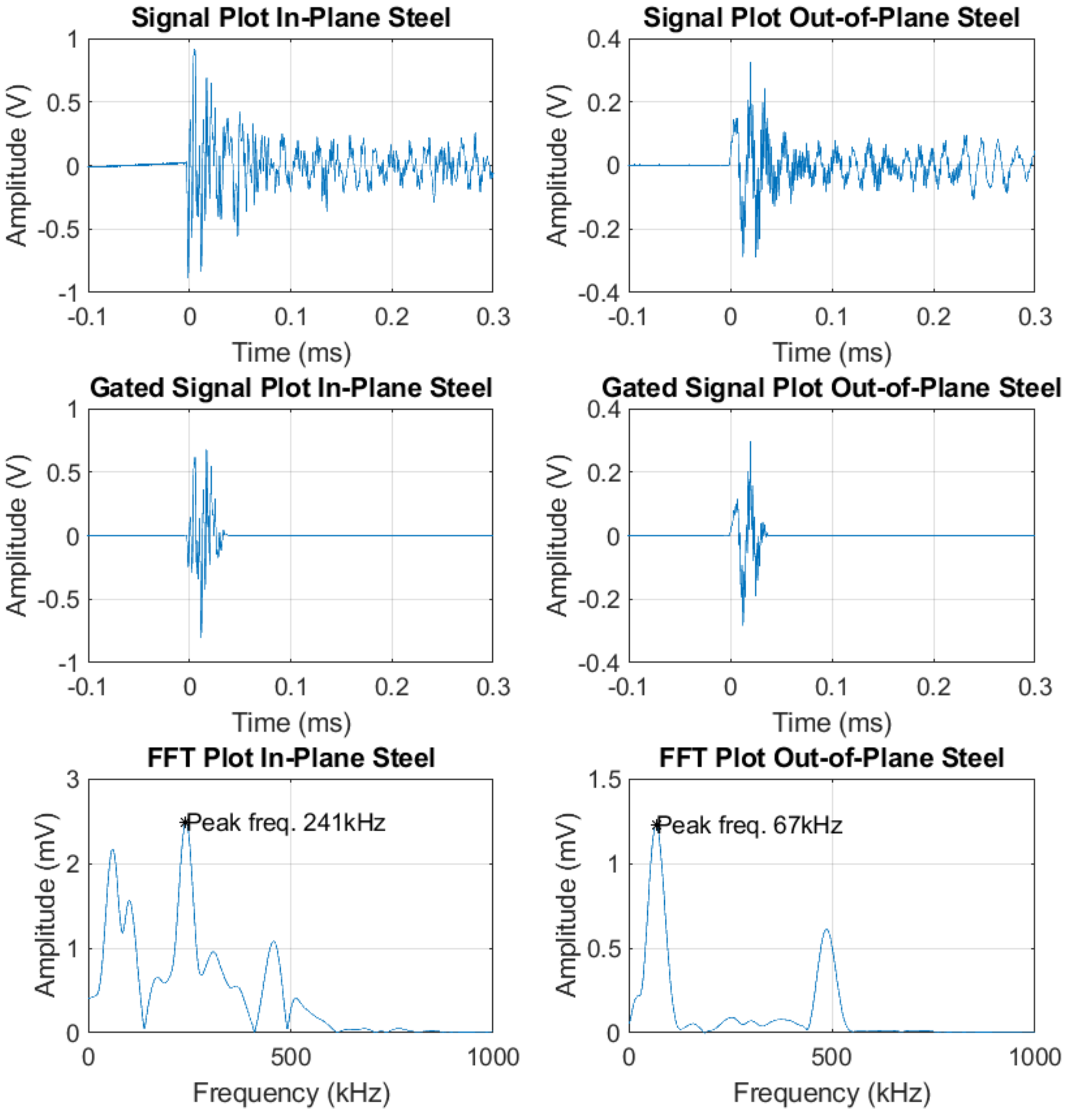

Figure B.2.7. Response on steel plate with the mini-Impactor with 0.5 mm thickness tip